


Summer 8-17-2018

Genetic Modification of Inherited Retinopathy in Mice

Yang Kong
yang.kong@maine.edu

Follow this and additional works at: <https://digitalcommons.library.umaine.edu/etd>

 Part of the [Congenital, Hereditary, and Neonatal Diseases and Abnormalities Commons](#), [Disease Modeling Commons](#), [Eye Diseases Commons](#), [Genetic Processes Commons](#), and the [Ophthalmology Commons](#)

Recommended Citation

Kong, Yang, "Genetic Modification of Inherited Retinopathy in Mice" (2018). *Electronic Theses and Dissertations*. 2901.
<https://digitalcommons.library.umaine.edu/etd/2901>

This Open-Access Thesis is brought to you for free and open access by DigitalCommons@UMaine. It has been accepted for inclusion in Electronic Theses and Dissertations by an authorized administrator of DigitalCommons@UMaine. For more information, please contact um.library.technical.services@maine.edu.

GENETIC MODIFICATION OF INHERITED RETINOPATHY IN MICE

By

Yang Kong

M.D. Weifang Medical University, 2008

M.S. Shandong University School of Medicine, 2011

A DISSERTATION

Submitted in Partial Fulfilment of the

Requirements for the Degree of

Doctor of Philosophy

(in Biomedical Science)

The Graduate School

The University of Maine

August 2018

Advisory Committee:

Patsy M. Nishina, Professor, Jackson Laboratory, Advisor

Gregory A. Cox, Associate Professor, Jackson Laboratory

Thomas Gridley, Professor, Maine Medical Center Research Institute

Stephen H. Tsang, Associate Professor, Columbia University Medical Center

Zhong-wei Zhang, Associate Professor, Jackson Laboratory

Copyright 2018 Yang Kong

GENETIC MODIFICATION OF INHERITED RETINOPATHY IN MICE

By Yang Kong

Dissertation Advisor: Dr. Patsy M. Nishina

An Abstract of the Dissertation Presented
in Partial Fulfilment of the Requirement for the
Degree of Doctor of Philosophy
(in Biomedical Science)

August 2018

The retina, as a critical component of the sensory system, consists of multiple cell types, of which, photoreceptors play a key role in receiving, integrating and transmitting light signals. The biofunctions of photoreceptors rely on their proper growth and development, which is predominantly governed by a cluster of molecules that comprise the transcriptional regulation for photoreceptor development. Any disruption of these molecules potentially incurs retinal pathologies.

It is known that deficiencies of nuclear receptor subfamily 2 group E member 3 (NR2E3) or neural retina leucine-zipper (NRL), two molecules in regulating photoreceptor cell development, cause photoreceptor dysplasia. In a sensitized chemical mutagenesis study to identify genetic modifiers in retinal degeneration (*rd*) 7 mice (*Nr2e3^{rd7}*), *Tvrm222*, was established, in which photoreceptor dysplasia was significantly rescued compared to that in *Nr2e3^{rd7}* mutants. Notably, the *Tvrm222* allele also ameliorates photoreceptor dysplasia in *Nrl* knockout mice. According to whole-genome mapping and exome sequencing, the modifier was localized to Chromosome 6 and was identified as a missense

variant in the FERM domain containing 4B (*Frmd4b*) gene, which is predicted to cause the substitution of serine residue 938 with proline (S938P).

Furthermore, we observed that the *Frmd4b*^{*Tvrm222*} allele preserved the integrity of the fragmented external limiting membrane (ELM) present in both *rd7* and *Nrl*^{-/-} mouse retinas. FRMD4B, as a binding partner of cytohesin 3 (CYTH3), has been proposed to participate in cell junction remodeling. However, its function in ELM maintenance and photoreceptor dysplasia has not been previously examined. This study revealed that the S938P variation significantly reduces *in vitro* membrane recruitment of FRMD4B.

Notably, in an attempt to explore the molecular mechanisms underlying the modifying effect of FRMD4B^{938P} on dysplastic retinas, we observed an increased activation of ADP-ribosylation factor 6, a direct substrate for CYTH3, both *in vitro* and *in vivo*, as well as decreased phosphorylation of AKT in *Tvrm222* retinas. These changes were accompanied by an elevation in cell membrane-associated zonula adherens and occludens proteins in *Tvrm222* retinas. Taken together, this study determines a critical role of FRMD4B in maintaining the integrity of adhesive support (at the ELM) and in rescuing photoreceptor dysplasia in mice.

ACKNOWLEDGEMENTS

My sincere appreciation goes to all of those individuals who contributed remarkably and gave me enormous help towards the completion of my Ph.D. study. First and foremost, I would like to express my deepest gratitude to my advisor, Dr. Patsy Nishina at the Jackson Laboratory for providing me with a concrete framework, on which this project was shaped; for giving me a platform to continuously explore the maximum potential of this work as well as of myself; for showing me the importance of persistence and commitment to scientific research even through the hardest periods of time, and finally for cultivating my capabilities toward becoming a sound scientist.

Second of all, I feel particularly grateful for all of the professors on my committee, including Dr. Gregory Cox, Dr. Thomas Gridley, Dr. Stephen Tsang and Dr. Zhong-wei Zhang, not only for their devotion to serving as members of my thesis committee during the past few years, but also for their critical guidance on my scientific research and insightful advice that shed light on my choice about my future career.

Thirdly, I would like to thank all the members, past and present who work in our group, including Dr. Jürgen Naggert, Dr. Lihong Zhao, Gayle Collin, Dr. Bo Chang, Dr. Mark Krebs, Lisa Stone, Wanda Hicks, Jeanie Hansen, Xiaojie Ji, Jieping Wang and Jeremy Charrette. Thanks to their unreserved enthusiasm and assistance in my experiments one after another, allowing my Ph.D. project to proceed smoothly.

In addition, I also want to thank all the service departments and working staff involved at the Jackson Laboratory, including the departments of histology, imaging, genomic sequencing and computational science, etc. Additionally, I would like to thank Dr. Michael Czech at the

University of Massachusetts for gifting us their antibody. Their contributions were invaluable and comprised an essential aspect of this project, without which this work would not be possible.

Meanwhile, my greatest appreciation goes to all the faculty members affiliated to the program of graduate school of biomedical science and engineering (GSBSE) at the University of Maine, especially director Dr. David Neivandt, former director Dr. Carol Kim and the administrative assistants for the GSBSE program, past and present, including Laura Hall, Tammy Crosby and Kristen Freeman. Not only did they provide me with numerous precious opportunities and support, but also meticulously attended to virtually every aspect involved for graduate studies in the GSBSE program, which ensured me of an extremely fruitful past few years of Ph.D. training.

Finally, I must say I feel very much blessed to have such a supportive and loving family. The tremendous dedication and unconditional love from my entire family, especially from my parents and grandparents, are the fundamental and pillars that supported me during the past few years working and living in the U.S., to which I will always feel indebted. I would like to dedicate this work to them.

TABLE OF CONTENTS

ACKNOWLEDGEMENTS	iii
LIST OF TABLES	x
LIST OF FIGURES	xi
ABBREVIATIONS	xiii
Chapter	
CHAPTER 1 INTRODUCTION	1
1.1 Retinal anatomy	1
1.2 Classification and function of photoreceptors	3
1.3 Differentiation and development of photoreceptors	5
1.3.1 Extracellular and epigenetic regulation of photoreceptor development	5
1.3.2 Transcriptional regulation of photoreceptor cell fate determination	7
1.3.2.1 NR2E3 gene regulatory network	9
1.3.3 The impact of Müller glia on photoreceptor development	9
1.4 Cell junctions in maintaining retinal architecture	10
1.4.1 Classification of cell junctions and their roles in the retina	10
1.4.2 ELM in healthy and sick retinas	12
1.4.3 Cell junctions at the ELM and photoreceptor dysplasia	13

1.5 Mouse models for dysplastic retinopathies.....	13
1.6 Identification and characterization of genetic modifiers of photoreceptor dysplasia in mice.....	15
1.6.1 ENU mutagenesis screen for modifier allele(s) in mouse models.....	16
1.6.2 Suppression of photoreceptor dysplasia in mice by the <i>Frmd4b</i> ^{Tvrm222} allele.....	16
1.7 Current knowledge about FRMD4B.....	17
1.7.1 Molecular characteristics of FRMD4B and its interaction with GEFs.....	17
1.7.2 The impact of CYTH3-FRMD4B on activation of ARF6.....	19
1.7.3 The impact of CYTH3-FRMD4B on AKT phosphorylation.....	20
1.8 The regulation of ARF6 and AKT in cell-cell contact and polarity.....	21
1.8.1 The impact of ARF6 on regulating cell adhesion and polarity.....	21
1.8.2 The regulatory role of AKT in cell adhesion and polarity.....	22
CHAPTER 2 METHODS AND MATERIALS.....	24
2.1 Mice.....	24
2.2 Identification of genetic modifier(s).....	24
2.2.1 ENU mutagenesis and mouse breeding.....	24
2.2.2 QTL whole genome mapping.....	26
2.2.3 Linkage analysis.....	28

2.2.4 Exome capture libraries and high throughput sequencing.....	28
2.2.5 PCR.....	29
2.3 Phenotypic characterizations	33
2.3.1 Indirect ophthalmoscopy.....	33
2.3.2 Fundus imaging.....	34
2.3.3 Electroretinography.....	34
2.3.4 Histology.....	35
2.3.5 Measurement of the thickness of ONL	36
2.3.6 Immunohistochemistry	36
2.3.7 Transmission electron microscopy	37
2.4 <i>In-vitro</i> transfection of <i>Frmd4b</i> and <i>Cyth3</i> for cell culture studies	38
2.4.1 Cell culture.....	38
2.4.2 Plasmid construct.....	39
2.4.3 Cell transfection.....	48
2.4.4 Immunofluorescence microscopy of transfected cells.....	49
2.5 SDS-PAGE analyses.....	50
2.5.1 Western blot.....	50
2.5.2 Co-immunoprecipitation	51

2.5.3 Subcellular fractionation assay	53
2.5.4 GTPase-activation assay	54
2.6 Antibodies	56
2.7 Imaging processing and statistical analyses.....	56
CHAPTER 3 RESULTS.....	58
3.1 ENU-induced <i>Tvrm222</i> variant as a genetic suppressor of <i>rd7</i> dysplasia	58
3.2 <i>Tvrm222</i> variant is able to normalize retinal structure in <i>rd7</i> mouse eyes	61
3.2.1 <i>Tvrm222</i> variant does not affect retinal cell proliferation or Müller gliosis.....	61
3.2.2 Rescue of defective ELM by <i>Tvrm222</i> variant	68
3.3 Identification of <i>Frmd4b</i> ^{<i>Tvrm222</i>} variant as the genetic suppressor of photoreceptor dysplasia.....	71
3.3.1 Mapping <i>Frmd4b</i> variant as the modifier in <i>Tvrm222</i> mouse retina	71
3.3.2 Expression analysis of <i>Frmd4b</i>	73
3.3.3 The <i>Frmd4b</i> ^{<i>Tvrm222</i>} variant as the modifier for NRL deficiency	73
3.4 Reduced cell surface recruitment of FRMD4B in the presence of 938P	77
3.5 Alterations of ARF6 and AKT pathways in the presence of S938P variation.....	82
3.5.1 Elevation of ARF6 activation associated with the FRMD4B ^{938P} variant	82
3.5.2 Decreased AKT phosphorylation associated with <i>Frmd4b</i> ^{<i>Tvrm222</i>} variant	84
3.5.3 Increased membrane-associated junctional components in <i>Tvrm222</i> retinas.....	84

CHAPTER 4 DISCUSSION.....	89
4.1 Characterization of <i>Tvrm222</i> modification of photoreceptor dysplasia	89
4.1.1 Recapitulation of morphological defects of ESCS patients in mice	89
4.1.2 Functional assessment of <i>Tvrm222</i> modification in mice.....	90
4.2 Identification of the <i>Tvrm222</i> mutation as the suppressor for photoreceptor dysplasia.....	91
4.2.1 Mapping and sequencing the <i>Tvrm222</i> genetic modifier(s)	91
4.2.2 Genetic suppressor for <i>rd7</i> photoreceptor dysplasia.....	94
4.3 The impact of S938P variation on biological properties of FRMD4B	97
4.3.1 Physical interactions of FRMD4B with its binding partners	97
4.3.2 <i>In-vitro</i> systems for elucidating biological properties of FRMD4B	98
4.4 Signaling pathways that mediate functions of the CYTH3-FRMD4B complex	100
CHAPTER 5 CONCLUDING REMARKS AND FUTURE DIRECTIONS	104
REFERENCES	107
BIOGRAPHY OF THE AUTHOR.....	126

LIST OF TABLES

Table 2.1 Oligo primers for PCR amplification.....	30
Table 2.2 <i>Nr2e3^{rd7}</i> genotyping.....	31
Table 2.3 <i>Nrl</i> knockout genotyping	31
Table 2.4 Amplification of candidate variants.....	32
Table 2.5 cDNA amplification.....	33
Table 2.6 Oligo primers for amplification of construct inserts.....	40
Table 2.7 Expand long template PCR system for amplifying <i>Frmd4b^{wt}</i>	40
Table 2.8 Site mutagenesis for <i>Frmd4b^{938P}</i>	41
Table 2.9 Amplification of <i>Cyth3</i> coding sequence.....	41
Table 2.10 Oligo primers for sequence verification of the plasmid constructs	47
Table 2.11 Antibodies.....	57
Table 3.1 Lines established from <i>Nr2e3^{rd7/rd7}</i> mutagenesis screen.....	61

LIST OF FIGURES

Figure 1. Anatomy of mouse retina	2
Figure 2. Development of photoreceptors and its transcriptional regulation.....	6
Figure 3. Schematic representation of a breeding scheme for producing <i>Tvrm222</i> mice.....	25
Figure 4. Schematic representation of breeding schemes for mapping and sequencing <i>Tvrm222</i> line	27
Figure 5. Construction of FRMD4B plasmid vectors for <i>in-vitro</i> transfection	43
Figure 6. Construction of CYTH3 plasmid vectors for <i>in-vitro</i> transfection	44
Figure 7. Reduction of <i>rd7</i> -associated pan-retinal spots in <i>Tvrm222</i> mice	59
Figure 8. Suppression of <i>rd7</i> -associated anatomic anomalies associated in <i>Tvrm222</i> mice.....	60
Figure 9. ERG analysis on outer retinal function of both <i>Nr2e3^{rd7/rd7}</i> and <i>Tvrm222</i> mice.....	62
Figure 10. Measurement of the ONL thickness in <i>Nr2e3^{rd7/rd7}</i> and <i>Tvrm222</i> mice with age.....	63
Figure 11. Impact of <i>Tvrm222</i> modification on (photoreceptor) cells in <i>rd7</i> retinas	65
Figure 12. The impact of <i>Tvrm222</i> variant on Müller glia	67
Figure 13. Prevention of ELM fragmentation associated with <i>rd7</i> dysplasia in <i>Tvrm222</i> retinas	69
Figure 14. Maintenance of retinal architecture in <i>Tvrm222</i> mice.....	70
Figure 15. Whole genome mapping to identify the modifier allele in <i>Tvrm222</i> mice.....	72

Figure 16. Expression profile of the <i>Frmd4b</i> transcript and the impact of the <i>Frmd4b</i> ^{Tvrm222} allele on mouse retina.....	74
Figure 17. Suppression of retinal dysplasia due to NRL deficiency in the presence of <i>Frmd4b</i> ^{Tvrm222/Tvrm222}	75
Figure 18. Maintenance of ELM integrity in <i>Nrl</i> ^{-/-} mice in the presence of the <i>Frmd4b</i> ^{Tvrm222/Tvrm222} allele	76
Figure 19. <i>In-vitro</i> cytosolic localization of FRMD4B without stimulation of insulin.....	78
Figure 20. Decreased membrane recruitment of FRMD4B ^{938P} with insulin stimulation <i>in vitro</i>	79
Figure 21. Dependence of FRMD4B on CYTH3 for cell-surface targeting.....	81
Figure 22. Unaltered binding between CYTH3 and FRMD4B in the presence of 938P variant and no physical interaction with junctional components.....	83
Figure 23. Increased level of GTP-binding form of ARF6 in presence of the FRMD4B ^{938P} variant.....	85
Figure 24. Decreased phosphorylation of AKT in <i>Tvrm222</i> mouse eyes.....	86
Figure 25. An increase in membrane-associated CTNNB1 in <i>Tvrm222</i> mouse retinas	87
Figure 26. An increase in membrane-associated TJP1 in <i>Tvrm222</i> mouse retinas	88
Figure 27. Working model of interactions of CYTH3-FRMD4B complex with AKT and ARF6 pathways for modifying retinal dysplasia	103

ABBREVIATIONS

AKT: Also known as Protein Kinase B (PKB)

AMT: Advanced Microscopy Techniques

ARR3: Arrestin 3

AJ: Adherens Junction

CDH3: Cadherin 3

cGMP: Cyclic Guanosine Monophosphate

COS7: CV-1 in Origin with SV40 genes

CRB1: Crumbs 1

CRX: Cone-Rod Homeobox

CTNNB1: Catenin Beta 1

CYTH3: Cytohesin 3

DAPI: 1 × 4', 6-Diamidino-2-Phenylindole

ELM: External Limiting Membrane

EMT: Epithelial-Mesenchymal Transition

ENU: N-Ethyl-N-Nitrosourea

ESCS: Enhanced S Cone Syndrome

ExAC: Exome Aggregation Consortium

FRMD4B: FERM Domain containing 4B

GEF: Guanine Nucleotide Exchange Factor

GFAP: Glial Fibrillary Acidic Protein

GPCR: G Protein Coupled Receptor

GRP1: General Receptor of Phosphoinositides 1

GS: Glutamine Synthetase

H&E: Hematoxylin and Eosin

HEK: Human Embryonic Kidney

HTS: High Throughput Sequencing

IACUC: Institutional Animal Care and Use Committee

ILM: Internal Limiting Membrane

IPL: Inner Plexiform Layer

IS: Inner Segment

iPSC: induced-Pluripotent Stem Cell

JEOL: JEM-1230 Microscopy Technique

LB: Lysogeny Broth

LCA: Leber Congenital Amaurosis

LOD: Logarithm of the Odds

NDS: Normal Donkey Serum

NR2E3: Nuclear Receptor subfamily 2, group E, member 3

NRL: Neural Retina-specific Leucine zipper

ONL: Outer Nuclear Layer

OPN1SW: Opsin 1, Short Wave

OS: Outer Segment

OTX2: Orthodenticle Homeobox 2

PFA: Paraformaldehyde

PH: Pleckstrin Homology

PH3: Phosphorylated Histone 3

PI3K: Phosphoinositide 3-Kinase

PIP2: Phosphatidylinositol 4,5-bisphosphate

PIP3: Phosphatidylinositol (3,4,5)-trisphosphate

PIP5K: Phosphatidylinositol 4-Phosphate 5 Kinase

PM: Plasma Membrane

PNA : Peanut Agglutinin

qRT-PCR: Quantitative Reverse Transcriptase Polymerase Chain Reaction

QTL: Quantitative Trait Locus

RD: Retinal Degeneration

ROR β : RAR-related orphan receptor β

RIPA: RadioImmunoPrecipitation Assay

RP: Retinitis Pigmentosa

RPE: Retinal Pigment Epithelium

RTK: Receptor Tyrosine Kinase

SD-OCT: spectral domain optical coherence tomography

SDS: Sodium Dodecyl Sulphate

SNP: Single Nucleotide Polymorphism

SOX9: SRY Box 9

SSR: Small Sequence Repeat

TEM: Transmission Electron Microscopy

TJ: Tight Junction

TJP: Tight Junction Protein

TR β 2: thyroid hormone receptor β 2

TVRM: Translational Vision Research Mouse

UV: Ultraviolet

WT: Wild Type

ZA: Zonula Adherens

ZO: Zonula Occludens

CHAPTER 1

INTRODUCTION

The visual system, as a part of the central nervous system, serves as one of the crucial senses that allows perception of the environment by animals, including human beings. According to an epidemiological study published in 2017, it was estimated that about 253 million individuals worldwide suffer from vision impairment of different degrees (1). Ocular diseases lead to a tremendous socioeconomic burden globally, especially among low-income or developing countries. Investigations on the biological properties of the visual system, as well as the etiologies of relevant diseases are expected to provide insights that lead to therapeutic interventions to restore sight and to ease the socioeconomic burden.

1.1 Retinal anatomy

The generation of vision depends on the retina, a multi-layered tissue situated at the back of the eye, consisting of multiple cell types, of which photoreceptors play a central role in receiving, integrating and transmitting visual signals (Figure 1A) (2). Photoreceptor cells are a specialized neuron that are terminally differentiated and exhibit a pattern of polarized growth during development in vertebrates. The photoreceptor cells synapse with bipolar and horizontal cells as well as interdigitate with retinal pigment epithelial (RPE) cells (Figure 1B). Phototransduction is initiated at the level of the photoreceptor outer segments (OS) where there are abundant photopigments for absorbing light. The chromophores of the photopigments undergo a conformational change when stimulated by external light stimuli, activating the visual cascade (3-6). Photoreceptor cells extend to the inner plexiform layer (IPL) where they synapse with the secondary neurons, including bipolar cells and horizontal cells to transmit the electrical impulses via amacrine and ganglion cells to the visual cortex in the brain (Figure 1C). The

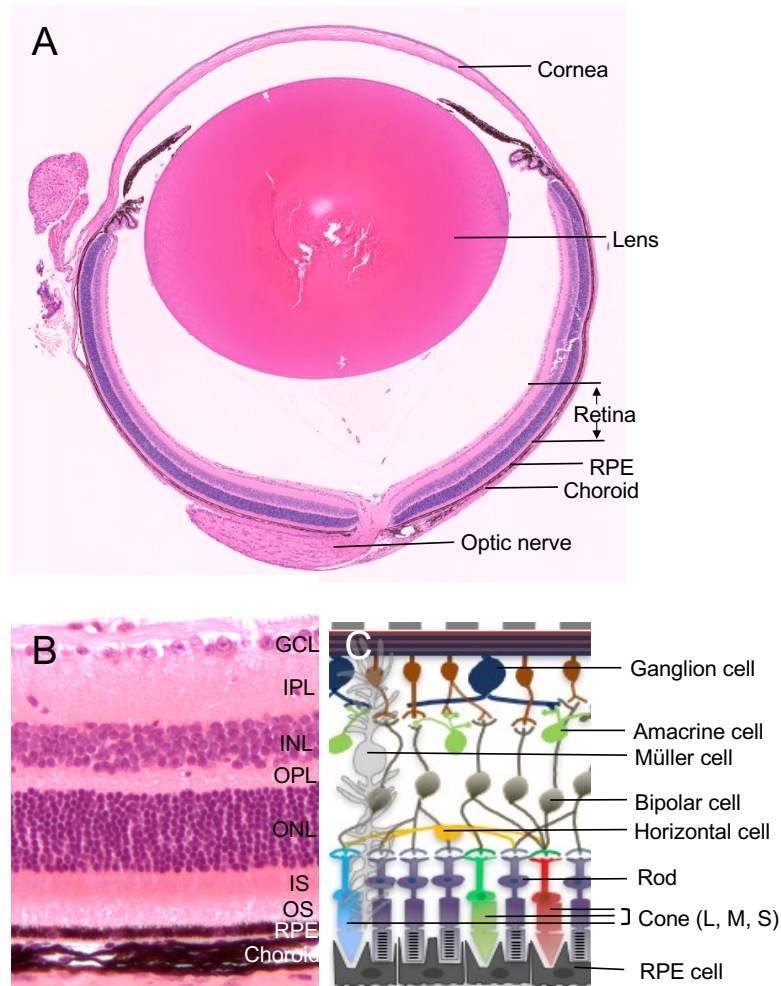


Figure 1. Anatomy of mouse retina. (A) A sagittal section of the eye of an adult C57BL/6J mouse; (B) A sagittal section of retina of an adult C57BL/6J mouse; (C) Schematic representation of the major cellular components of mouse retina. GCL: ganglion cell layer; IPL: inner plexiform layer; INL: inner nuclear layer; OPL: outer plexiform layer; ONL: outer nuclear layer; IS: inner segment; OS: outer segment; RPE: retinal pigment epithelium

photoreceptor inner segment (IS) is connected to the OS via the connecting cilium and contains a large number of mitochondria (7). The IS/OS are situated beneath the external limiting membrane (ELM), which is comprised of cell junctions between photoreceptors and apical processes of Müller glial cells. The nuclei of photoreceptor cells predominantly comprise the outer nuclear layer (ONL) in the retina situated toward the vitread aspect of the ELM.

1.2 Classification and function of photoreceptors

Vertebrate photoreceptor cells, based on cell morphology and function, broadly fall into two major categories, rod photoreceptors and cone photoreceptors. The rod photoreceptor OSs are cylindrical in morphology and extremely sensitive to photons due to an abundance of rhodopsin – a molecule comprised of a protein, opsin, and *11-cis* retinaldehyde, a derivative of Vitamin A, that is stored in the OS disc membrane. Rod photoreceptors primarily function in dim light conditions, as rhodopsin is hypersensitive to photons (8). The OSs of cone photoreceptors are conical in morphology and are primarily responsible for photopic vision and color perception. In contrast to rhodopsin, cone opsins in OS of cone photoreceptors are less sensitive and require a higher luminance level (9, 10). The cone photoreceptors are further classified into three subtypes: L-cone, M-cone and S-cone based on their major absorption spectra of light by the particular cone opsin associated with each cone type (11). The peak absorption wavelength for L cones is around 560 nm, and for M cones, 520 nm. S cones are predominantly responsive to the wavelength of light at ~ 420 nm (12-14). In addition, cone photoreceptors play a major role in visual acuity. The quantity and distribution of rod and cone photoreceptors vary remarkably across species. Generally, rod photoreceptors are dominant in number, with ~ 20-fold more rods than cones in human beings (15, 16). The mosaic of rods and cones in the nocturnal murine species shows even a larger difference with ~ 97% rods compared to ~ 3%

cones in the mouse retina (17, 18). In terms of distribution, rod cells are greater in density than cone cells, and span the entire retina except for the specialized macular area termed fovea in humans (19, 20). The density of cone cells reaches its peak in fovea while the number of rod cells drops remarkably to form a rod-free region in the fovea center. This anatomic characteristic establishes the fovea as the region of highest visual acuity, which declines outside the foveal center (21-23). Due to the topographic distribution of photoreceptors within the foveal region, lesions that affect the cone photoreceptors in this area may have dire consequences to vision (e.g. age-related macular degeneration).

Although visual phototransduction is a complex process, it is one of the best-characterized G-protein coupled receptor (GPCR) signaling cascades (24, 25). The process encompasses reception of light signals by the photoreceptors, conversion of biochemical signals into electrical signals, and transmission of electrical signals to horizontal and bipolar cells. The visual information is relayed by bipolar cells to ganglion cells and to the lateral geniculate nucleus, which is finally transmitted to the visual cortex. Phototransduction is initiated with stimulation of photopigment proteins by photons, which isomerizes *11-cis*-retinal to *all-trans*-retinal and eventually leads to a conformational change in the GPCR that subsequently leads to the activation of the G protein transducin (26). Transducin further activates the phosphodiesterase, which converts cyclic GMP (cGMP) into GMP. Consequently, the cytosolic concentration of cGMP is reduced (5, 27). The reduction of cGMP levels results in the closure of cGMP-gated cation channels that eventually leads to hyperpolarization of photoreceptor cells. The process culminates with a reduction in the release of glutamate, a neurotransmitter for signal propagation by photoreceptors to secondary neurons in the retina (28, 29).

1.3 Differentiation and development of photoreceptors

1.3.1 Extracellular and epigenetic regulation of photoreceptor development

The normal function of photoreceptors is determined by their proper growth and development. Photoreceptor cells are derived from neuroepithelial progenitor cells. This group of cells exhibit multi-potency in most species and is capable of dividing symmetrically or asymmetrically simultaneously, which eventually produce multiple lineages within the retina (30, 31). By using radioactive labeling or specific antibody markers, it was demonstrated that the retinal cells do not arise synchronously but show a sequential overlap in cell fate commitment to different lineages in temporal order across species (32, 33). Generally, cone photoreceptors are committed much earlier than rods, especially in animals with longer gestational periods (34, 35). The temporal development of rod and cone photoreceptors varies among species. In mice, commitment of precursors to cone photoreceptors take place at embryonic day (E) 11 and is completed before birth. Whereas rod photoreceptor genesis occurs later, initiating as early as E13 and reaching peak development at P0. Some rods are even formed postnatally (Figure 2A) (36).

Cell fate specification of precursors into particular retinal cell types requires precise regulation from both intrinsic and extrinsic cues that govern proliferation of multi-potent retinal progenitor cells, commitment to particular cell types, and morphologic and functional differentiation (34, 37, 38). According to studies, innate differentiation capacity of progenitors into specific lineages is determined spatiotemporally, which, to a great extent is achieved via their responsiveness towards extracellular cues and transcriptional regulation (39-41). For instance, it was reported that insulin-like growth factor is capable of promoting retinal progenitor cell identity (42, 43) *in vitro* during early development, as well as facilitates orchestration of laminar neuroretinal organization postnatally (44). Moreover, an alteration in the levels of

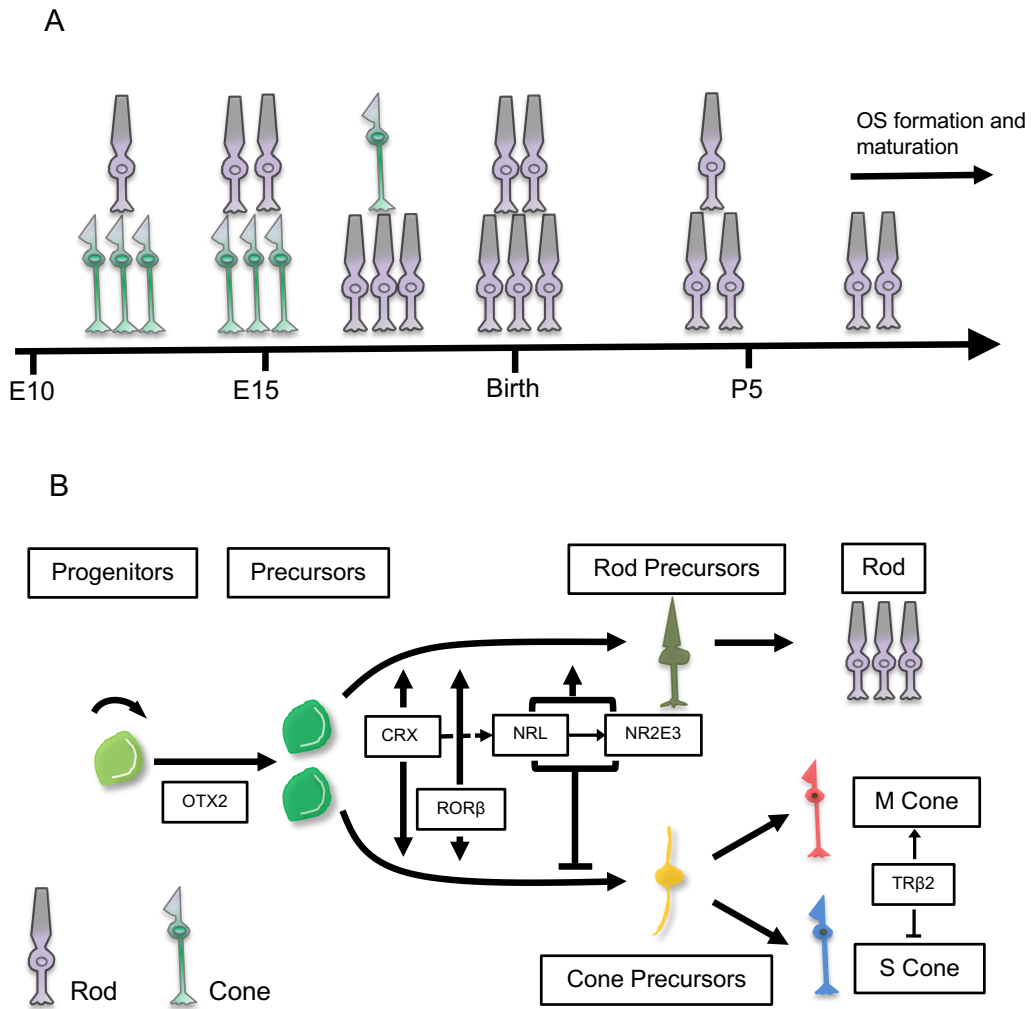


Figure 2. Development of photoreceptors and its transcriptional regulation. (A) The time course of development of both rod and cone photoreceptors in mouse retina. (B) Transcriptional regulation of photoreceptor development in mouse retina. OS: outer segment, OTX2: orthodenticle homeobox protein, CRX: cone-rod homeobox protein, ROR β :RAR-related orphan receptor β , NRL: neural retina leucine zipper protein, NR2E3: nuclear receptor subfamily 2 group E member 3, TR β 2: thyroid hormone receptor β 2

transforming growth factor, in conjunction with epidermal growth factor, is capable of inducing proliferation or selective cell fate commitment of retinal progenitors (45). In addition to extracellular signals, intrinsic factors function as critical machinery to ensure photoreceptor development and differentiation from progenitor cells. For instance, alteration of chromatin configuration, an epigenetic modification directly controls chromatin accessibility and serves as a key element in determining the expression of target genes (46, 47). Additionally, epigenetic modification is often correlated with transcriptional activity to determine cell fate commitment (48).

1.3.2 Transcriptional regulation of photoreceptor cell fate determination

Transcriptional regulation of cell fate determination serves a fundamental mechanism to ensure the accurate and step-wise development and differentiation of multi-potent progenitors to matured cell types in the retina. Compared to the regulatory network during the early stages of retinogenesis that is poorly delineated, the mechanism underlying photoreceptor commitment into rods and cones from precursor cells is distinctly defined (49). This process is primarily dictated by a panel of transcription factors, namely, orthodenticle homeobox protein (OTX2), cone-rod homeobox protein (CRX), RAR-related orphan receptor β (ROR β), neural retina leucine zipper (NRL) protein, nuclear receptor subfamily 2 group E member 3 (NR2E3) and thyroid hormone receptor β 2 (TR β 2) (39, 49).

These six transcription factors are members of a signaling pathway that functions cooperatively in a sequential manner (Figure 2B). Specifically, OTX2 is located upstream in the transcriptional hierarchy and functions as the premier “checkpoint” that drives the commitment of post-mitotic retinal progenitors into photoreceptor cell fate (50). Ablation of OTX2 in retinal progenitor cells results in loss of multiple retinal cell types, including rod and cone

photoreceptors (51), which indicates its fundamental role as a differentiation signal of retinal progenitor cells. Subsequently, the regulation to terminal differentiation to photoreceptor cells relies on CRX, which is first expressed at E12.5 in mouse, and directly acts on promoter regions of *rhodopsin* and cone *opsin* (52). It synergizes with NRL to promote expression of photoreceptor genes, especially in favor of rod photoreceptor commitment (53). In respect to specification to photoreceptor cell subtypes, ROR β , plays a dual role in promoting differentiation to both rod and cone photoreceptors, and functions upstream of NRL and NR2E3. Moreover, ROR β is indispensable for the maturation of OS and synapses in the retina (54). Photoreceptor precursors expressing NRL adopt a rod cell fate by inducing expression of rod-specific genes (55). NRL deficiency in mouse retina causes accumulation of excessive cone-like cells at the expense of rods, as more immature precursor cells are differentiated into cone photoreceptors (56). Similarly, NR2E3, whose transcription is directly governed by NRL, diverts differentiation to rods by suppressing cone cell genes (57). In contrast, TR β 2 found in cone photoreceptors, mediates differentiation to M-cones (54).

Although these transcription factors were proposed to function in a distinct hierarchical manner during the development of photoreceptor cells, their regulatory mechanisms are far more complex and do not necessarily act in a linear fashion (58). While it was regarded that retinal progenitor cells differentiate into S-cone as the default program for cell fate commitment that is controlled by OTX2, CRX and ROR β in a hierarchical manner to ensure specification of progenitors into different photoreceptor cell types (49), a relevant study pointed out that any given transcription factor among the six is capable of modulating the transcriptional activity of the remaining factors (58). Coordination of these transcription factors is extremely important to guarantee the precise differentiation and homeostasis of photoreceptors in mammals. Hence, it is

likely that perturbation of any member of the photoreceptor transcriptional regulatory network could result in retinopathies. In fact, *Crx* mutations are associated with autosomal dominant Leber congenital amaurosis (LCA) and late-onset retinitis pigmentosa (RP) (59-61). Disruption of *NRL* is reported to be involved in RP (62). Mutations in *NR2E3* are known to cause enhanced S cone syndrome (ESCS) in human populations (63) as well as RP (64, 65). These retinal disorders are generally characterized as developmental defects or dystrophy of photoreceptor cells. Histologically, photoreceptor dysplasia and disruption of cellular composition are two prominent pathological changes associated with these retinopathies due to mutations in transcription factors, including *NRL* and *NR2E3*.

1.3.2.1 NR2E3 gene regulatory network

According to previous investigations in which expression was assessed by microarray hybridization screening and quantitative reverse transcriptase polymerase chain reaction (qRT-PCR) analysis, *NR2E3* was found to regulate the expression of an array of genes (66). Analysis of gene profiles of *Nr2e3^{rd7/rd7}* mice revealed a large number of differentially expressed genes that fall into different functional categories, including cell growth and proliferation (e.g. *Bub1b*, *Hrasls*), fatty acid metabolism (e.g. *Fabp7*) and apoptosis (e.g. *Arhgdib*) (67). The differences in expression, which were validated, indicate a wide-ranging effect of *NR2E3* on a variety of biological phenomena. Conceivably, disruption of *NR2E3* could lead to extensive pathological consequences. Therefore, targeting an array of genes may provide different avenues for remedying *NR2E3*-associated pathologies.

1.3.3 The impact of Müller glia on photoreceptor development

In addition to transcriptional regulation necessary for the development and maintenance of photoreceptor cell homeostasis – Müller glial cells also function as an indispensable

modulator in development and differentiation of photoreceptor cells (68). Glial cells in the CNS function as adhesive support and insulation for neurons; providing an environment that protects neurons against mechanical trauma and facilitates neuronal development and plasticity (69-71). As a specified glia in retina, Müller glial cells are the last cell type to differentiate from multipotent progenitors in the retina (72). They are essential for retinal homeostasis as they: 1. Maintain a metabolically stable microenvironment for the neurons by degrading neurotransmitters and releasing neurotrophic factors as well as the antioxidant-glutathione; 2. Participate in forming mechanical barriers for compartmentalizing the retinal microenvironment and maintaining structural stability; 3. Create an anti-proliferative condition for a healthy retina; and 4. Mediate retinal innate immunity and initiate wound healing (73, 74). Most strikingly, it has been documented that Müller glial cells under certain circumstances have a reprogramming potential to produce progenitors for photoreceptor regeneration (75). Reactive gliosis is reported to be initiated in response to lesions in the retina such as dysplasia. Whereas removal of Müller glia results in death of photoreceptor cells (76).

1.4 Cell junctions in maintaining retinal architecture

1.4.1 Classification of cell junctions and their roles in the retina

Morphogenesis of the retina and the execution of its biological functions rely on precise coordination among individual cells, which is largely mediated by cell-cell contact and communication with the microenvironment. The cell-cell contact among individual cells depends upon proper assembly of cell junctions. Cell junctions consist of multiple protein complexes, bridging the cell membrane and also governing the interaction between cells and the extracellular matrix (77). Cell junctions function in a wide range of biological processes, including proliferation, migration, polarization, orchestration of solid tissue development, signal

transduction, and also serving as a diffusion barrier for substances (77-79). Cell junctions are functionally categorized as anchoring (*e.g.* adherens junctions, AJ), occluding (*e.g.* tight junctions, TJ), or communicating junctions (*e.g.* gap junctions) (77). This study particularly focused on AJs and TJs as well as the pathophysiologic impact of their disruption.

AJs are a prerequisite for the assembly of TJs and provide a physical bridge between cells and provide stabilization that is necessary for tissue formation (77, 80, 81). Two major categories of protein complexes participate in forming AJs: cadherin-catenin and nectin-afadin complexes, which provide a physical intercellular association by connecting the cytoskeleton and cytoplasmic actin filaments of two neighboring cells (82). Previous investigations demonstrated that AJs play a profound role in regulating retinal growth and development (in *Drosophila*) – from initiating development from the neuroepithelium, to determining apical-basal polarity of retinal cells as well as controlling the shape of photoreceptor cells (83).

TJs are predominantly located at the most apical domain between epithelial cells, which seals the paracellular space to form a selective barrier for diffusion of fluids and solutes (84). TJs are comprised of two main structural units: 1. the transmembrane component, which includes claudin, occludin and junctional adhesion molecules that stretch across the plasma membrane (PM) to link two adjoining cells via extracellular adhesion domains; and 2. the intracellular scaffolding components, including tight junction protein (TJP) -1, -2 and -3, which are required to tether the transmembrane components, such as occludin, claudins and junctional adhesion molecules, etc. (85-87). These junctional components are extremely critical to maintaining tissue growth and development of the retina. For instance, it has been shown that the TJ components act as intracellular signaling molecules to maintain homeostasis of retinal morphology (78, 88).

Functional cell junctions are necessary to create a favorable microenvironment for differentiation and development of the retina. Strikingly, disruptions of both AJs and TJs have been linked to multiple retinopathies. For instance, aberrant expression of AJ and TJ proteins was found to be associated with autosomal dominant RP in adult mice lacking rhodopsin (89). In addition, changes in expression of AJ and TJ-associated components may undermine retinal barriers, such as blood-retinal barrier, disruption of which facilitates initiation and progression of diabetic retinopathy (90, 91).

1.4.2 ELM in healthy and sick retinas

Conventionally, cell junctions, such as AJs and TJs are regarded as “fences” that separate the apical and basal portions of the cell. Apart from the RPE, the ELM is a major site in the retina where cells junctions are most identifiable. Although the ELM appears as a distinct “membrane” observable by light microscopy or spectral domain optical coherence tomography (SD-OCT), it is actually comprised of continuous zonula adherens (ZA) and zonula occludens (ZO) junctional complexes between photoreceptor ISs and the surrounding apical processes of the Müller glial cells or between Müller glial cells (92). The ELM functions to maintain retinal structural stability and serves as a permeable barrier to control diffusion of substances. It is reported that impairment of ELM integrity causes sub-retinal fluid accumulation, leading to macular edema (92).

Further evidence that changes in ELM morphology is correlated with certain inherited retinal disorders comes from studies of Stargardt disease, one of the most common forms of macular degeneration in juvenile patients. Stargardt disease is characterized by progressive vision loss due to death of photoreceptor cells. Clinical investigation revealed a thickened ELM as a notable SD-OCT feature in young patients (93, 94).

1.4.3 Cell junctions at the ELM and photoreceptor dysplasia

Retinal dysplasia, as a unique pathological entity was first described almost a century ago. It can be initiated by inherited and postnatal insults, such as bacterial infection, X-ray irradiation, metabolic disturbance, etc. (95). Only a handful of investigations have elaborated the pathological properties associated with retinal dysplasia. Some reports indicate cell loss and retinal detachment, leading to potential visual impairment or even blindness (96). Histologically, the dysplastic changes lead to distortion of retinal lamination. It is usually characterized by disrupted cell-cell contact of photoreceptor cells with their neighboring cells, and perturbation of apical-basal polarity, in which disorganization of the retinal laminar architecture, formation of whorl-like structures and gliosis are seen (97). By careful examination, it was noted that fragmentation of the ELM is a prominent feature associated with retinal dysplasia (rosette-like structure) in mice due to aberrant transcriptional regulation (98). Hence, it has been hypothesized that the dysplasia is likely to be the result of aberrant development of photoreceptors (99). Additional studies to better understand how aberrant growth and development of photoreceptors lead to the dysplasia and subsequent photoreceptor cell loss are necessary to generate efficient and effective treatments.

1.5 Mouse models for dysplastic retinopathies

The availability of animal models, especially genetically modified mice, has provided remarkable insights into photoreceptor biology and the dysplastic changes that occur as a result of genetic defects (e.g. disruption of genes that lead to photoreceptor dysplasia) and the mechanisms underpinning the observed pathologies. As aforementioned, the mice bearing a knockout allele of *Nrl* and/or a spontaneous mutation in *Nr2e3* phenotypically recapitulates the disease observed in humans. *Nrl* knockout (*Nrl*^{-/-}) mice generated by deletion of exons 2 and 3

by homologous recombination, phenotypically exhibit abundant dysplastic lesions in the ONL , as well as a significant decline of scotopic vision (56). The retinal degeneration (*rd*) 7 mouse model was identified as a splice site mutation in *Nr2e3* that leads to an in-frame deletion of exons 4 and 5, which is predicted to result in a protein sequence lacking 127 amino acids. Pronounced photoreceptor dysplasia is also observable in mice lacking NR2E3 (100). These two models demonstrate that abnormal development of photoreceptor cells could potentially give rise to dysplastic lesions in retina.

Another murine model in which retinal dysplasia occurs is the strain bearing the *rd8* mutation. It harbors a spontaneous frame shift mutation of *Crumb homologue (Crb) 1* gene (101). *Crb1* is expressed in Müller glia cells in the mouse retina. CRB1 is a critical element in determining cell-polarity and governing AJ formation between Müller glial cells and photoreceptors (102, 103). Molecular studies of human families with vision impairment reveal that *CRB1* variants cause both autosomal recessive RP and LCA (104). According to the clinical observations, *CRB1* mutations lead to disorganized retinas, which is manifested as increased thickness of retinas, distortion of retinal layers, etc. On the other hand, the *Crb1^{rd8/rd8}* mouse, lacking functional CRB1, exhibits classic retinal dysplasia with disruption of cell-cell contact and defective photoreceptor ISs and OSs (105), and recapitulates clinical manifestations to a great extent. Careful characterizations of *Crb1^{rd8/rd8}* mice revealed loss of ELM integrity, displacement of photoreceptors and aberrant retinal morphology as focal adhesive support is lost (101).

Loss or dysfunction of photoreceptors can lead to catastrophic consequences for vision. Therefore, a comprehensive and thorough understanding of photoreceptor biology and of the basis for the pathological changes that underlie retinopathies such as dysplasia, is necessary to

formulate appropriate therapeutic interventions. The mouse models serve as a powerful tool to better understand the pathophysiology of features of the disease, and to test effects of genetic interventions for therapeutic purposes. In this study, we particularly focus on ameliorating dysplastic photoreceptors in *Nr2e3*^{rd7/rd7} and *Nrl*^{-/-} mice by genetic modifications. Identifying potential genetic modifier(s) and the molecular mechanisms through which they function, may provide insights into developing efficacious treatment.

1.6 Identification and characterization of genetic modifiers of photoreceptor dysplasia in mice

Several lines of evidence indicate that multiple factors contribute to the clinical outcomes of *NR2E3* mutations (106). Firstly, while mutations in *NR2E3* were originally shown to cause enhanced S-cone syndrome, other retinal diseases associated with mutations in the gene, such as Goldmann-Favre syndrome and RP, have been reported (64, 107, 108). Secondly, the mode of inheritance (*e.g.*, dominant vs. recessive) and the expressivity of the disease phenotype varies among patients. Reports on human patients suggest that at least one variant of *NR2E3*, p. E121K, leads to different outcomes in Caucasian and Chinese Asian populations (65).

In mouse, modifier screens with different strains of mice have shown that the retinal dysplasia associated with B6.Cg-*Nr2e3*^{rd7/rd7} mice can be totally suppressed to yield morphologically and functionally normal photoreceptors. Interestingly, mapping of the modifier loci in different crosses using three genetically distinct strains showed that they did not overlap, indicating that a number of genetic modifiers exist (109). The first reported genetic modifier of *Nr2e3*^{rd7/rd7} was identified as the *Nr1d1* gene, another transcription factor that influences rod photoreceptor fate (110). Additionally, a point mutation of *Prph2* that leads to a frameshift and a nonsense codon, which is inherited in dominant fashion and somewhat phenotypically resembles

Nr2e3^{rd7/rd7} is found to cause defective OS, retinal degeneration and impairment of photoreceptor function. The transcriptional expression of *Prph2* is directly regulated by NR2E3, which may account for the aberrant formation of OS and degeneration associated with *rd7* retinopathy (111).

1.6.1 ENU mutagenesis screen for modifier allele(s) in mouse models

The chemical mutagenesis screening using N-ethyl-N-nitrosourea (ENU) is a phenotype-driven method, which allows for the identification of disease phenotypes of interest without previous knowledge about the genetic basis of mutation. It efficiently creates mutant mouse resource, offering a complementary way for producing mouse models with clinical relevance (112). ENU is an alkylating agent that transfers its ethyl group to nucleobases, preferentially to thymine (113). Consequently, a DNA nucleotide substitution on DNA takes place after replication, resulting in point mutations. In terms of carrying out the ENU mutagenesis study, proper dosage of ENU and breeding strategy of mice are two key aspects that guarantee successful propagation of induced mutations.

The sensitized ENU-mutagenesis screen for identifying genes that affect the *Nr2e3^{rd7/rd7}* phenotype has proven to be an efficient strategy for identifying genetic modifiers. The selected mice were subject to comprehensive phenotypic characterizations. In this study, we identified seven strains with heritable ocular phenotypes by indirect ophthalmoscopy in a screen of ~850 mutagenized *Nr2e3^{rd7/rd7}* mice. Four of the strains showed fewer *rd7*-like fundus spots and three, a completely different fundus phenotype in comparison to the non-mutagenized parental *Nr2e3^{rd7/rd7}* strain.

1.6.2 Suppression of photoreceptor dysplasia in mice by the *Frmd4b^{Tvrm222}* allele

We chose to focus on the *Tvrm222* modifier strain for the purposes of this dissertation project. The *Tvrm222* mouse line exhibits a significantly reduced pan-retinal spotting phenotype

that was heritable and epistatic on *Nr2e3^{rd7/rd7}*. Quantitative trait locus (QTL) mapping analyses was carried out to identify the chromosomal location of the modifier(s) of the photoreceptor dysplasia phenotype. A second mapping cross with a different parental partner strain was carried out to confirm the mapping location and the segregation of the mutation with the observed reduced retinal spotting phenotype. In parallel, DNA from *Tvrm222* mice was subject to high throughput sequencing (HTS) for mutational analysis.

According to the HTS data, multiple missense variants were located in the minimal region suggested by the mapping analyses. By further genotyping of each variant, we could only validate a missense variant of *Frmd4b* gene on Chromosome 6 that co-segregated with the *Tvrm222* modification.

1.7 Current knowledge about FRMD4B

FRMD4B was first identified as a binding partner of cytohesin 3 (CYTH3/GRP1: general receptor of phosphoinositides 1) more than a decade ago (114). However, the biological functions of FRMD4B remained largely obscure. In particular, no definitive evidence indicated a link to visual function or the regulatory network for photoreceptor development.

1.7.1 Molecular characteristics of FRMD4B and its interaction with GEFs

FRMD4B was identified during a CYTH3 screen, a member of the ADP-ribosylation factor (ARF) guanine nucleotide exchange factor (GEF) family (115), to identify binding factors that modulate its localization and function. Using a radioactive P-labeled CYTH3 probe, a mouse brain cDNA expression library was screened. A cDNA clone encoding a CYTH3-binding protein was isolated, which exists as two different splice variants in brain and lung. The binding protein was first named CYTH3/GRP1 signaling partner 1, which contains a FERM protein interaction domain and two coiled-coil domains that directly interact with CYTH3 (114). The molecule was

later renamed FRMD4B. The majority of FRMD4B was found to co-localize with CYTH3 intracellularly. However, not all CYTH3 is bound to FRMD4B (114). *In vitro* studies show that the CYTH3-FRMD4B complex is normally sequestered in the cytoplasm without stimulation of extracellular cues. With inclusion of insulin in culture media, a large proportion of CYTH3-FRMD4B complex undergoes an acute translocation to the PM (114). As a scaffold protein, membrane recruitment is one the most prominent biological properties for CYTH3-FRMD4B complex identified thus far.

Although it has been more than a decade since these initial discoveries on FRMD4B were concluded, little progress has been made toward understanding its function and biological impact. Recently, however, a Japanese group found FRMD4B, and its homologue FRMD4A, functions as key adaptors in linking the partitioning defective (PAR) - atypical protein kinase C (aPKC) complex and the cytohesins to regulate ARF6 activity that profoundly affects epithelial cell junction remodeling and cellular polarity. Deletion of FRMD4A and/or FRMD4B remarkably disrupts cell-cell contact *in vitro* (116), which strongly implies a role for FRMD4B in cell junction development and maintenance as well as its potential impact to cause pathological changes if disrupted *in vivo*. However, the biological function of FRMD4B, especially in diseased conditions, requires additional studies.

FRMD4B as a scaffold protein as it was predicted, is a key determinant to GEF function, as biological functions of GEFs largely depend on their engagement and disengagement to signaling complexes (117, 118). In terms of the biological features of scaffold proteins, it can be defined as molecules that interact with more than two other signaling components, and mediate specific intracellular localization (e.g. PM, cytoplasm, nucleus and mitochondria) of signal molecules (119, 120). For example, scaffold proteins play an indispensable role in spatio-

temporally control of recruitment and partitioning of GEFs on the cell surface (121). Most of the scaffold proteins provide platforms for assembly of signaling molecules, modulation of intracellular translocation of signaling molecules, coordination of positive and negative feedback signals and inhibition of inactivating signals (122). In the latter circumstance, scaffold proteins provide additional complexity to the signaling pathways by mediating the properties of intracellular signals for subsequent transmission (123). For instance, the physical interaction of connector enhancer of kinase suppressor of Ras1, a scaffold protein that binds cytohesin is critical to activating the PI3K-AKT pathway induced by insulin or insulin growth factor 1 (124).

1.7.2 The impact of CYTH3-FRMD4B on activation of ARF6

GEFs based on their catalytic GTPase substrates, are classified into five major categories (125). CYTH3/GRP1 is a member of ARF-GEF due to the presence of a conserved catalytic Sec7 domain that acts on ARF6 to release GDP in exchange for GTP binding (125). Mechanistically, CYTH3 catalyzes the GTP/GDP exchange of ARFs by conformational modification of the nucleotide-binding site so that the affinity for the nucleotide is altered. This results in release of GDP with subsequent replacement with GTP. During the course of GTP/GDP cycling, GEFs displace the bound nucleotide, and a new nucleotide can subsequently displace the bound GEFs (126). GEFs can be functionally inhibited by interfering with their Sec7 domains by a number of means. For example, brefeldin is sensitive to high molecular-weight GEF-ARF (~ 200 kDa), while RNA aptamer M69 works on small GEF sec7 domains (127, 128).

In addition to the catalytic domain, the pleckstrin homology (PH) domain of CYTH3 is necessary for ARF-GEFs function, as the conformational change of the PH domain is closely related to the auto-inhibitory mechanism for GEF (129). The PH domain is notably responsible for mediating the membrane targeting of GEFs via its interaction with phospholipids, which is

necessary for its activation (130, 131). For GEFs, at least three major methods for their translocation to the cell surface are utilized. In addition to their interactions with phospholipids, the associated ARF substrates as well as the binding partners are utilized for membrane recruitment of GEFs (132). Currently, studies examining how disruption of binding partners, such as FRMD4B, modulates CYTH3 regulation on ARF6 activity are unavailable. Conceivably, a wide spectrum of biological consequences could be generated as CYTH3 function is altered through the influence on its binding partners and subsequent effects on its downstream signals, including ARF6.

1.7.3 The impact of CYTH3-FRMD4B on AKT phosphorylation

As aforementioned, CYTH3 binds phospholipids via its PH domain for membrane recruitment. In fact, CYTH3 was first isolated by screening for protein-coding clones that bound 3'-phosphoinositides with high affinity, and was defined as the downstream target of PIP3, as it is capable of coupling the production of PIP3 at the cell surface to activate ARF6 (133, 134). It is worth noting that PIP3 in parallel serves to phosphorylate AKT, the core component of PI3K-AKT pathway that governs a large number of biological processes (135-137). In light of the spatial proximity of CYTH3 with AKT at the PM, it is possible that the CYTH3-FRMD4B complex is capable of influencing the phosphorylation of AKT, especially under the circumstance in which membrane recruitment of CYTH3-FRMD4B is affected. In fact, a relevant study has shown that CYTH3 plays a critical part in recycling glucose transporter type 4 in insulin signaling by linking ARF6-regulated vesicular trafficking and AKT (138). Generally, cytohesins are regarded as positive activators of insulin signaling. They are important for cell growth and insulin sensitivity (139, 140). Moreover, abundant studies coupled the function of cytohesin GEFs and growth factor signaling pathways (141-143). Collectively, these studies

indicate an extensive involvement of GEFs in intracellular signal transduction. Thus, in this dissertation, the effects of the disruption of FRMD4B on activation of ARF6 and/or phosphorylation of AKT are addressed. Our results show that both ARF6 activation and AKT phosphorylation are affected in the presence of FRMD4B^{938P} variant, which suggests that the effects of FRMD4B on both ARF6 and AKT pathways may be via the CYTH3-FRMD4B complex.

1.8 The regulation of ARF6 and AKT in cell-cell contact and polarity

Proper lamination is a key element during its normal retinal development. Establishing cellular connectivity is a complex process in vertebrates and is spatiotemporally determined by a cluster of genes coding for transcription factors as well as the other molecules (83, 144-146). Considering that the dysplastic lesions in the neuroretina of *Nr2e3*^{rd7/rd7} and *Nrl*^{-/-} mice appears to result from a failure of normal cell junction formation and perturbation of cell polarity, it prompted us to explore whether and in what way an aberrant CYTH3-FRMD4B complex can contribute to and affect the dysplastic process.

1.8.1 The impact of ARF6 on regulating cell adhesion and polarity

Reports revealed that ARF6 contributes significantly to cell junction remodeling and polarization, which is achieved through linkage to the PAR-aPKC complex (116). This complex is evolutionarily conserved and is central to the regulation of cell polarization and focal adhesion (147, 148). A number of previous studies have shown that PAR3 physically binds multiple molecules, including Girdin, LIMK2, Tiam1, etc. to regulate cytoskeleton dynamics and cell polarity (149, 150). Furthermore, disruption of PAR3 in mice leads to abnormal formation of tight junctions, failed apical-basal membrane identities and lumen formation during epithelial morphogenesis (151, 152). aPKC, a serine/threonine kinase, it is primarily responsible for apical

determination of membrane identity and separating polarity regulators among apical, lateral and basal surfaces of the cell (153-155). Finally, PAR6 has been shown to act as a regulatory subunit for aPKC, and more importantly, to function as an adaptor to link aPKC and PAR3 (156, 157). ARF6, on the other hand, primarily modulates rearrangement of cytoskeleton at the cell periphery and membrane remodeling (158). The regulatory effect of ARF6 on cytoskeletal dynamics is considered to occur via activating Rac1 GTPase and/or mediating lipid composition of membrane (159, 160). Additionally, ARF6 exerts a fundamental influence on cell junction remodeling. ARF6-GTP initiates disassembly of AJs between epithelia through internalizing adherens junctional components and re-distributing $\beta 1$ integrin receptors that anchor the cells to the extracellular matrix (161-163). Despite the large array of information of the role of ARF6 on cell adhesion, the studies on the effects of ARF6 activation on ELM integrity are currently lacking.

1.8.2 The regulatory role of AKT in cell adhesion and polarity

Much of the involvement of ARF6 in regulation of cell adhesion and polarization is achieved through modulation of lipid membrane composition, as ARF6 is capable of regulating the synthesis of membrane phospholipid PIP2 (164). Additionally, direct binding of PAR3 to both PIP2 and PIP3 for membrane docking is also a key prerequisite for establishing apical-basal membrane identity (165). It is important to note that CYTH3 and AKT both physically interact with PIP3 (133, 166). The PI3K-AKT pathway also functions in determining cellular behaviors, including migration, adhesion and polarization that are typified by epithelial mesenchymal transition (EMT), a fundamental process for both development and oncogenesis (167). EMT is characterized as a transition from orchestrated adherent epithelial sheet into disorganized mesenchymal composition with disrupted cell-cell contacts (168). A growing number of

evidence shows that basal level of AKT phosphorylation maintains apical-basal polarity with reduced motility of epithelial cells. Constitutive activation of AKT results in reduced expression of E-cadherin and cleavage of intercellular junctions, as well as transformation from apical-basal to front-rear polarity of individual cells (169-171).

It should be noted that the majority of the investigations cited above were carried out in the epithelial cell culture. Knowledge about AKT phosphorylation and cell plasticity in a neuronal context, especially in regards to diseased photoreceptors is still scarce. In this study, we found an alteration in AKT phosphorylation in the presence of FRMD4B^{938P} variant that phenotypically ameliorates photoreceptor dysplasia in *Tvrm222* mice.

CHAPTER 2

METHODS AND MATERIALS

2.1 Mice

Procedures involving mice were approved by Institutional Animal Care and Use Committee (IACUC) and were conducted according to the Association for Research of Vision and Ophthalmology Statement for the Use of Animals in Ophthalmic and Vision Research. The mouse strains utilized in this study included: C57BL/6J (JR# 000664), C57BL/6NJ (005304), DBA/2J (JR# 000671), B6.Cg-*Nr2e3^{rd7}*/J (JR# 004643), B6.Cg-*Nr2e3^{rd7}.Frmd4b^{Tvrm222}*/Pjn (JR# 30623) and B6;129-*Nrl^{tm1Asw}*/J (JR# 021152). All strains were housed and bred in the Research Animal Facility at The Jackson Laboratory. The mice were provided ad libitum a NIH 6% fat diet and acidified water and were housed in a vivarium with a 12-hour light/12-hour dark cycle. The ages of mice used are indicated in the subsequent sections for specific experiments.

2.2 Identification of genetic modifier(s)

2.2.1 ENU mutagenesis and mouse breeding

A sensitized chemical mutagenesis screen was used to identify genetic modifiers of *Nr2e3^{rd7}*. For mutagenesis, adult male *rd7* mice (10-12 weeks of age) were administered ENU intraperitoneally at a dosage of 70 mg/kg between 9-11 am once a week for three weeks. After two months, mutagenized male mice (G₀) were crossed to non-mutagenized female *rd7* mice. If females were impregnated prior to three months post injection, the mutagenesis was considered failed and the mating was terminated. Male G₁ mice born three months or later post administration of ENU were crossed to a non-mutagenized *rd7* female to generate a G₂ population. Four G₂ females were backcrossed to their G₁ sires (Figure 3) to generate G₃ mice, which were screened by indirect ophthalmoscopy at 12 weeks of age. Any phenotypically altered

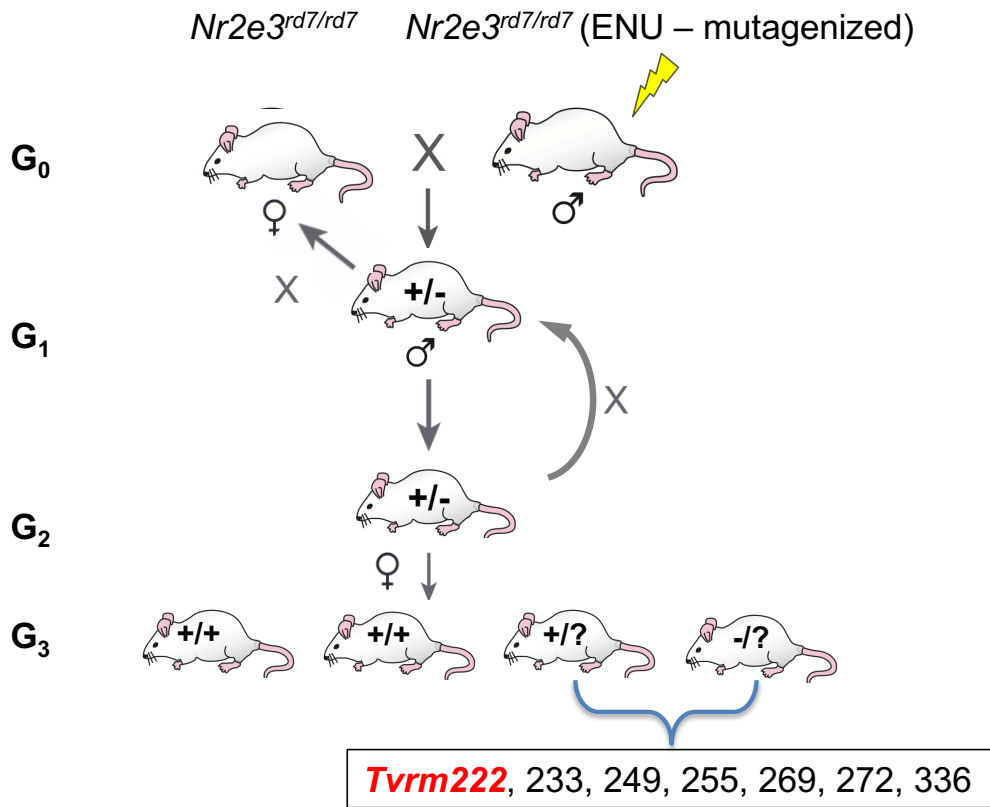


Figure 3. Schematic representation of a breeding scheme for producing *Tvrn222* mice.

Adult ENU-mutagenized $Nr2e3^{rd7}$ homozygous mice (G_0) were mated with untreated female $Nr2e3^{rd7}$ homozygous mice; G_1 males were crossed to homozygous female $Nr2e3^{rd7}$ mice to produce G_2 progenies; G_2 females were mated to their G_1 sire to produce G_3 progenies. The G_3 mice were screened by indirect ophthalmoscopy and the mouse lines with altered fundus presentations were retained and listed in the graph. G_0 - G_3 indicates the generations involved in producing *Tvrn222* line (red). Adapted from Acevedo-Arozena, A. *et al.* Annu Rev Genomics Hum Genet. 2008; 9:49-69

Nr2e3^{rd7/rd7} mice were bred to unmutagenized *Nr2e3^{rd7/rd7}* mice. F₁ progeny were examined by indirect ophthalmoscopy to determine whether the effect was heritable and if the mutation acted in a dominant manner. If the altered phenotype was not observed in the F₁ progeny, they were either intercrossed or backcrossed to an affected sire to determine if the mutation was heritable and acted in a recessive manner. Once the mode of heritability of the modifier was established, mice were backcrossed to N₅ to remove unlinked mutagenized regions that did not segregate with the altered *Nr2e3^{rd7/rd7}* phenotype.

2.2.2 QTL whole genome mapping

For whole genome mapping, mice were generated according to the following breeding scheme: *Tvrm222* mice bearing two copies of the modifier allele were mated with C57BL/6NJ mice to produce F₁ mice; Subsequently, F₁ mice were crossed to *Nr2e3^{rd7/rd7}* mice. Only N₂ progeny homozygous for *rd7* were retained for fundus examination and a whole genome scan (Figure 4). The fundus phenotypes were scored as either 0 for unaffected (*rd7*-like mice) or 1 for affected (reduced or no spotting phenotype). DNA samples from 34 unaffected and 17 affected individuals were subject to whole genome mapping, for which 143 single nucleotide polymorphic (SNP) genetic markers capable of distinguishing B6/J and B6/NJ mice genomic material were used.

For genome-wide one-dimensional scan, 128 imputations used as pseudo-markers were generated at 2 cM spacing for each chromosome. One thousand permutations were performed to determine the thresholds for QTL detection. Four thresholds were calculated from the permutation results. QTLs with logarithm of the odds (LOD) score above the 1% threshold was considered strong QTLs, while LOD scores above 63% indicated a suggestive QTL. For a pair wise two-dimensional scan, 2 cM spacing was used. All possible pairs of QTL locations on each

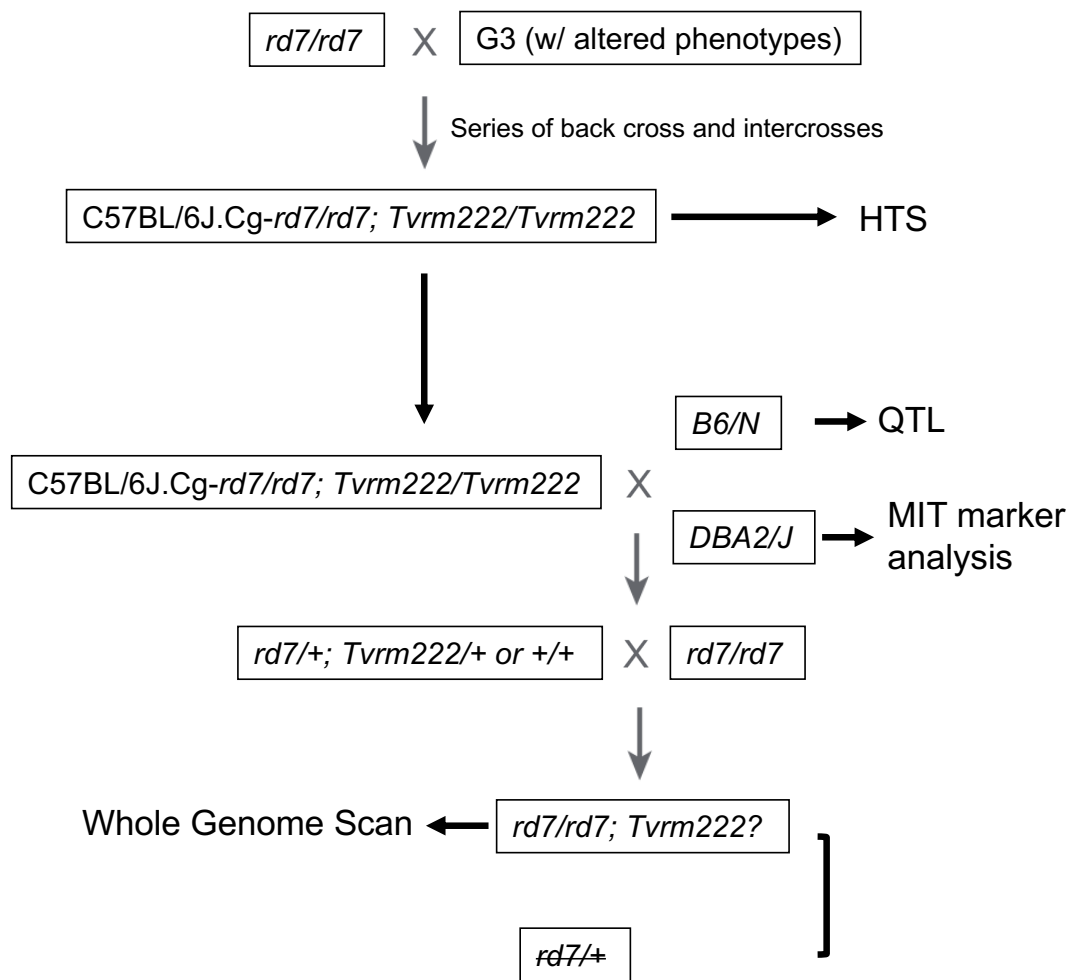


Figure 4. Schematic representation of breeding schemes for mapping and sequencing *Tvrn222*

line. Upper panel: Production of F₁ mice by mating G₃ mice with *rd7* homozygotes for high throughput sequencing (HTS); Lower panel: Producing F₁ mice with either C57BL/6NJ or DBA2/J mice for different mapping crosses utilized. For mapping the F₁ progenies were mated with *rd7* homozygotes to produce mice that were genotypically homozygous *rd7*.

chromosome were tested for association with the alteration in the *rd7* fundus spotting phenotype. The significance thresholds were based on the 5% thresholds following the routine pipeline established by the computational service department at the Jackson Laboratory. QTLs along with possible QTL \times QTL interaction identified from both single QTL and pair wise scans were fit into multiple regression models in the presence of significant covariates, if any. Variations of the phenotype in the models were estimated. P values for terms in the multiple-regression model were calculated. Terms were dropped sequentially until all of the terms in the model were significant at 5% level for both the main QTL and their interaction effects. R/QTL version 1.23-16 was used for the statistical analysis.

2.2.3 Linkage analysis

The mice for linkage analysis were prepared in a similar manner with that for QTL mapping, except that *Tvrm222* mice were mated with DBA/2J mice and the subsequent F₁ mice crossed to *Nr2e3^{rd7/rd7}* mice (Figure 4). A total number of 21 back-cross mice (11 affected and 10 unaffected) were examined phenotypically by indirect ophthalmoscopy and scored as 0 for unaffected and 1 as affected (no spotting phenotype). Seventeen simple sequence length repeat MIT markers were used to scan the five chromosomal regions, including Chromosomes 1, 3, 6, 8 and 18, with the highest LOD scores suggested by QTL mapping. The data were statistically analyzed using the R program following the same fashion with that for QTL mapping.

2.2.4 Exome capture libraries and high throughput sequencing

In order to identify the causative mutation, a whole mouse exome library of a homozygous *Tvrm222* mutant was constructed: using fragmented genomic DNA (1 μ g) to a peak size of 300 bp by sonication for 30 s-power on and 30 s-power off on low power for a total of 10 minutes using a Bioruptor UCD-200TM-EX (Diagenode). The pre-capture paired end library

was constructed using Illumina TruSeq DNA Sample Preparation Kit (Illumina, part number FC-121-100) with no size selection step and 18 cycles of PCR. The pre-capture library was hybridized to the Mouse Exome (Roche NimbleGen, Reference, 9999042611) capture probe set according to the manufacturer's protocol. The sequencing library was quantified by qPCR and sequenced on a single lane of a HiSeq 2000 sequencer (Illumina) by using a 2,100-base (paired end) sequencing protocol. DNA from three *Nr2e3^{rd7}* mutant animals was prepared similarly and served as a control.

2.2.5 PCR

The mouse genotypes were determined by PCR using the following procedures: 1. *Genomic DNA extraction*: tail snips were collected and digested by 50 mM NaOH and boiled for 15 minutes. Tris-EDTA (pH 8.0) was added then to neutralize the digested tail snips after 5-minute cooling at the room temperature. The genomic DNA was ready to use after a 6-minute centrifugation at $4,000 \times g$ at 4°C ; 2. *PCR amplification*: 2 μL of genomic DNA was used in 25 μL reaction volume containing 1 M Tris pH 9, 1 M $(\text{NH}_4)_2\text{SO}_4$, 1 M MgCl_2 , 10 mM dNTP, 30 μM oligos, DMSO and 0.25 U Taq DNA polymerase. The concentrations of each oligonucleotide primer that was used were based on the specific ratios between primer pairs (Table 2.1). PCR thermal cycling programs specific to the genotyping protocol can be found in Table 2.2 – 2.4. The amplified DNA samples were electrophoresed in 3% metaphor gels containing EZ-vision (AMRESCO, N391), and visualized under ultraviolet (UV) light.

The level of *Frmd4b* transcript expression was assessed by using the protocols provided by Dynabeads mRNA Direct Kit (Life Technologies) for isolating mRNA from multiple mouse tissues, and by iScript cDNA Synthesis Kit (BIO-RAD, 1708890) for cDNA synthesis. mRNA isolation procedures depended upon the use of Dynabeads that are covalently coupled to oligo

Table 2.1 Oligo primers for PCR amplification

Oligos	Sequence (5' – 3')	Note
LZO315 (<i>rd7L₁F</i>)	ATTTCTGTGCTGATTTTTATAACAATGAATATATC	Genotyping for <i>Nr2e3</i> ^{rd7/rd7} mice
LZO317 (<i>rd7Nr2e3F</i>)	GATGTCACCAGCAATGACCCC	
LZO316 (<i>rd7Nr2e3R</i>)	TCCACTGTCACTGCCCT	
<i>Frmd4b</i> ^{Tvrm222} Seq_F	CAGCTTACAGGTAGAGTAATGAG	Sequencing (genomic DNA), amplicon: 253 bp
<i>Frmd4b</i> ^{Tvrm222} Seq_R	TCCCTACACCAGCTACTATG	
16374 (<i>Nrl_F</i>)	GAGCTCACTTTGTGGACCAG	Genotyping for <i>Nrl</i> knockout mice
16373 (<i>Nrl_R</i>)	ACGGTGGTGTACCGAGAGAC	
17433 (<i>Nrl_R₁</i>)	GTTCTAATTCATCAGAAGCTGAC	
<i>Trac1</i> Seq_F	CGACAAGGTCCTACAGCAAGGA	Sequencing for <i>Trac1</i> variant
<i>Trac1</i> Seq_R	TAACACTGGGGAGCTGAAGTGG	
<i>Dctn1</i> Seq_F	CCAAATGAGGGGACTGGGAACT	Sequencing for <i>Dctn1</i> variant
<i>Dctn1</i> Seq_R	GTGCTCCTGCTTCTCTGAGGAA	
<i>Grccl0</i> Seq_F	TGCTTCTGATTGCAGGTGTC	Sequencing for <i>Grccl0</i> variant
<i>Grccl0</i> Seq_R	AGCAGCAGCACACATACGAG	
<i>Klra6</i> Seq_F	CCCATGTGTCCCAGAATGCAAC	Sequencing for <i>Klra6</i> variant
<i>Klra6</i> Seq_R	AGATGGCCTCTGTTCTGCAAGT	
<i>mFrmd4b_F</i>	GGGTCAAGCTGTGGTCCAGTAT	RT-PCR (cDNA amplification)
<i>mFrmd4b_R</i>	TGGCCGATTCCTTTGTAGCTGA	
<i>actin_F</i>	CCAGTTCGCCATGGATGACGATAT	RT-PCR (cDNA amplification)
<i>actin_R</i>	GTCAGGATACCTCTCTTGCTCTG	

Table 2.2 *Nr2e3^{rd7}* genotyping

Temp °C	Time	Note
94	2 min	
94	15 s	10 cycles, 0.5°C less for “55°C 15 s” step of each subsequent cycle after the initial one
55	15 s	
72	30 s	
94	15 s	30 cycles
50	15 s	
72	30 s	
72	30 s	
20		Hold

Table 2.3 *Nrl* knockout genotyping

Temp °C	Time	Note
94	2 min	
94	20 s	10 cycles, 0.5°C less for “65°C 15 s” step of each subsequent cycle after the initial one
65	15 s	
68	10 s	
94	15 s	28 cycles
60	15 s	
72	10 s	
72	2 min	
10		Hold

Table 2.4 Amplification of candidate variants

Temp °C	Time	Note
97	3 min	
95	15 s	45 cycles
55	30 s	
72	30 s	
72	3 min	
11		Hold

(dT) residues and recognize poly A residues located at the 3' end of most mRNA. Beads were re-suspended by placing them on a magnet for 30 seconds until the suspension became clear and was washed with fresh lysis/binding buffer prior to use. Tissues were collected in an RNase-free environment. In order to dissect the eyecup, the anterior segment was removed after enucleating the whole eye from CO₂ asphyxiated mice. The tissues were weighed and rapidly transferred to lysis/binding buffer to avoid degradation of the mRNA. The tissues were homogenized on ice. DNA was sheared by repeated passage of the lysate through a 21-gauge needle if the lysate is very viscous. The lysis/binding buffer was removed from 200 µL volume washed beads before 1 mL of lysate was added to the beads. The beads and sample lysate were re-suspended by pipetting, followed by a three-to-five-minute incubation at room temperature. Longer incubation times were utilized if the solution was viscous. The sample tubes were placed next to a magnet for ~two to ten minutes in order to precipitate the beads and to allow for the removal of the supernatant. The bead/mRNA complexes were washed twice at room temperature with one volume of washing buffer provided with the kit. Bead/mRNA complexes were washed twice with an appropriate volume of washing buffer B at room temperature. Finally, the washing buffer was separated from the beads using a magnet and discarded. About 20 µL elution buffer (10 mM Tris-HCl, pH 7.5) was applied to the bead/mRNA complex, followed by a two-minute incubation

at ~ 70°C. The tubes were immediately placed on the magnet after incubation in order to separate the beads from mRNA-containing supernatant, which was transferred to new tubes and placed on ice for use in ensuing experiments.

To determine the mRNA concentration for cDNA synthesis, A_{260} was determined by NanoDrop 2000C spectrophotometry. One μg mRNA was used to mix with 5 \times iScript reverse transcription mix, containing iScript MMLV-RT, RNase inhibitor, dNTPs, oligo (dT), random primers, etc. and nuclease-free water in a 20 μL reaction system, which was incubated in a thermal cycler with programs described in Table 2.5. Absorbance of synthesized cDNA was determined prior to storage at -20°C for future use. All the pairs of primers used for amplifying *Frmd4b* by PCR are shown in Table 2.1. The PCR products were visualized by electrophoresis in 3% agarose gel, containing EZ-Vision In-Gel Solution (AMRESCO, N391)

Table 2.5 cDNA amplification

Temp °C	Time	Note
25	5 min	
42	60 min	
85	5 min	
4		Hold

2.3 Phenotypic characterizations

2.3.1 Indirect ophthalmoscopy

G₃ mice were subject to phenotypic characterization using indirect ophthalmoscopy at six weeks of age, a time point at which the *rd7*-associated pan retinal spotting phenotype is distinctly observable. The mice were administered 1% atropine sulphate topically to dilate pupils. The examination for both eyes by indirect ophthalmoscopy was conducted in a dim environment for

five minutes after administration of the atropine. Mice that showed significantly reduced or no retinal spotting were backcrossed to non-mutagenized *rd7* mice until N₅, post-mutagenesis, to reduce the mutation load of unlinked ENU mutations that did not have a modifying effect.

2.3.2 Fundus imaging

Fundus photo-documentation was carried out at 1.5 months for *Nr2e3^{rd7/rd7}*, *Tvrm222* mice and at one month of age for *Nrl^{-/-}* mice (with and without the modifier). Specifically, mice were administered 1% atropine sulphate topically to dilate pupils. Goniovisc hypromellose ophthalmic solution was applied for surface lubrication and forming a fluid bridge, if necessary. The mice were kept in a dark environment for about five minutes prior to the documentation process. Images were acquired by Micron III and IV retinal imaging microscopes (Phoenix Research Laboratories).

2.3.3 Electroretinography

The function of the outer retina was assessed by electroretinography (ERG). Mice were dark-adapted overnight and anesthetized with ketamine (80mg/kg) and xylazine (16 mg/kg). Corneas were anesthetized using 1% proparacaine HCl and pupils were dilated using 1% mydriacyl, 2.5% phenylephrine HCl and 1% cyclopentolate. Mice were placed on a temperature-regulated heating pad to maintain at 37⁰C temperature throughout the entire recording session. *Nr2e3^{rd7/rd7}* and *Tvrm222* mice were tested at 1.5 months of age with B6/J as the wild type control. *Nrl^{-/-}* mice (with the *Tvrm222* modifier allele) were tested at one month of age with the appropriate age-matched control.

To measure ERG components, responses were recorded from the corneal surface using a stainless-steel electrode that was wetted with 0.7% methycellulose. Needle electrodes placed in the cheek and the tail served as reference and ground leads, respectively. Responses were filtered

(0.3-1500 Hz), differentially amplified, averaged and stored using a UTAS E-3000 signal averaging system (Diagnosys LLC). Responses were first obtained to stimuli presented in the dark. Flash stimuli were presented in an LKC ganzfeld and ranged in luminance from -3.6 to 2.1 log cd.s/m²; inter-stimulus intervals were increased from 4s at the lowest flash luminance to 61s at the highest stimulus levels. Stimuli were presented in order of increasing luminance and at least two successive responses were averaged for each stimulus condition. A steady rod-desensitizing adapting field was then presented within the ganzfeld bowl. After a seven-minute period of light adaptation, cone ERGs were recorded to flashes superimposed upon the adapting field. Flash luminance ranged from -0.8 to 1.9 log cd s/m² and responses to 50 flashes presented at 2.1 Hz were averaged at each intensity level.

The amplitude of the a-wave was measured 10 ms after flash onset from the pre-stimulus baseline. The amplitude of the b-wave was measured from the trough of the a-wave to the peak of the b-wave or alternatively from the pre-stimulus baseline if no a-wave was present. Implicit times were measured from the time of flash onset to the a-wave trough or the b-wave peak. The responses of both eyes were recorded and averaged.

2.3.4 Histology

Eyes from mice of different ages, including two weeks, one month, 1.5 months, two months, six months and one year were obtained for histologic examinations. Mice were asphyxiated by CO₂ followed by cervical dislocation according to an IACUC-approved protocol. The eyes were enucleated and placed in a solution containing methanol, acetic acid and 1× phosphate-buffered saline (PBS) with the volume ratio of 1: 3: 4, respectively, for a minimum of five-hours at 4°C with rocking. Fixed eyes were embedded in paraffin and sectioned transversely across the optic nerve. For hematoxylin and eosin (H&E) staining, sections were de-paraffinized

by immersing slides into 100% xylene, and ethanol solutions of decreasing concentrations (100%, 95%, 70% and 50%). Subsequently, sections were stained for five minutes in 1× hematoxylin and rinsed with tap water for an additional five minutes. The slides were submerged two to three times in acidic alcohol (1% HCl in 70% EtOH) and rinsed for five minutes with tap water. Slides were then submerged in diluted ammonia (1 mL NH₄OH in 1L H₂O) until the slides were noticeably darker. The slides were rinsed with tap water again followed by Eosin staining for one minute and another thorough rinse with tap water. Finally, the slides were rehydrated in EtOH and Xylene solutions in the reversed order described above. The slide sections were examined with a light microscope (Leica)

2.3.5 Measurement of the thickness of ONL

The mouse eye sections were collected at different ages, including six weeks, six months and one year, and were prepared for H&E stained sections as described previously. The ONL thickness was measured ~ 350 μm away from the optic nerve using ImageJ/FIJI software.

2.3.6 Immunohistochemistry

Sections were obtained from whole eyes that were fixed for a minimum of five hours to overnight at 4°C with cold 4% paraformaldehyde (PFA) or methanol: acetic acid (3:1) in 1× PBS. The choice of fixative was dependent on the primary antibodies used (see Table 5). The sections were paraffin-embedded and rehydrated as described above.

After rehydration, the slides were washed with 1× PBS three times for five minutes per wash. The epitopes masked by PFA were retrieved with heating in 10 mM citrate buffer (pH 6.0). The slides were microwaved to boiling in the 10 mM citrate buffer for four minutes then incubated for another four minutes in the same solution. The citrate buffer was replenished constantly to ensure full immersion of the slides. After antigen retrieval, the slides were allowed

to come to room temperature. Subsequently, slides were washed with 1× PBS three times with five minutes each prior to incubation of the slides in 5% blocking solution prepared by diluting normal donkey serum (NDS) with 1× PBS containing 0.1% triton X100 (PBST) for one hour at room temperature.

Primary antibodies were prepared by diluting the desired primary antibodies with blocking solution at different working concentrations. Primary antibodies were applied to sections and placed in a humidified chamber at 4°C overnight. The slides were then washed with 1× PBS three times for five minutes each. During the wash, the secondary antibodies were prepared by dilution in blocking solution with the ratio of 1:200. The secondary antibodies conjugated with fluorophores that emit fluorescence of different spectra were selectively employed based on species of primary antibodies that they recognize. The sections were incubated for one hour at the room temperature with the appropriate secondary antibody in a dark humidified chamber to shield the fluorophore from light exposure. After the incubation, the slides were washed with 1× PBS twice for five minutes each. Meanwhile, a 1× 4', 6-diamidino-2-phenylindole (DAPI) solution was prepared by diluting a DAPI stock solution with 1× PBS using 1:500 ratio. The sections were incubated in a dark chamber with DAPI solution for one minute followed by two 1× PBS washes. The processed slides were mounted with mounting media (Sigma-Aldrich, F4680) and examined with a fluorescence microscope (Leica SP5), following the manufacturer's protocols. The fluorescence channels including UV, 488 and 555 were selected. 20× and 63× objects were used. Z-stack images were generated, if necessary.

2.3.7 Transmission electron microscopy

Transmission electron microscopy (TEM) of *Nr2e3^{rd7/rd7}*, *Tvrm222* and B6/J wild type mice was carried out at one month of age to reveal ultrastructural differences. Mice were

perfused by intra-cardiac injection with PBS followed by fixation with phosphate buffered 2.5% glutaraldehyde/2% PFA in the Sorensen buffer. Eyes were enucleated and incubated with the pre-chilled fixative for 30 minutes. Anterior segments were carefully removed and eyecups were fixed for four additional hours at room temperature followed by an overnight fixation at 4°C on a rocker in the original fixative diluted to 1:10 with 1· PBS. Eyecups were carefully minced into small triangular shapes and post-fixed with 1% osmium tetroxide for two hours. Subsequently, the tissues were rinsed in a series of increasing alcohol concentrations. Dehydrated tissues were embedded in epoxy resin. Tissue sections were cut and stained with uranyl acetate and lead citrate and examined with a transmission JEM-1230 electron microscopy (JEOL). Images were captured using the advanced microscopy techniques (AMT) camera system.

2.4 *In-vitro* transfection of *Frmd4b* and *Cyth3* for cell culture studies

2.4.1 Cell culture

COS-7 and HEK293T cells were revived from our cell line stocks stored in liquid nitrogen. Cells were handled in a sterile environment in a laminar flow hood. The cells were cultured in pre-treated CytoOne T25 tissue culture flasks (USA SCIENTIFIC, CC7682-4325) or 60 mm petri dishes (USA SCIENTIFIC, 8690-0160) with fresh Dulbecco's modified eagle medium (DMEM, high glucose, Thermofisher Scientific, 11965092) supplemented with 10% fetal bovine serum (FBS). The cells were placed in an incubator (Thermofisher Scientific) set at 37°C with 5% CO₂ and were passaged when they reached 70~80% confluence. Two to three passages were performed for thorough revival of the cells prior to use in the experiments. For insulin treatment of cultured cells, 100 nM insulin was prepared using the following procedure: 1. 10 µL 12N HCL was mixed with 12 mL double distilled water (pH 7.6); 2. 6.9 mg anhydrous insulin (Sigma, 91077C) was dissolved in 12 mL 0.01N HCl as the stock solution (100 µM); 3.

The stock solution of insulin was diluted to 1:1000 with PBS and filtered. Aliquots of 100 nM insulin were stored at 4°C.

2.4.2 Plasmid construct

In order to prepare the vectors containing wild type *Frmd4b* or the *Frmd4b* isoform 3 (NCBI Gene ID: 232288), the *Frmd4b* open reading frame was amplified from mouse lung cDNA library using the Expand Long Template PCR system (Roche, 11681834001), using 1.5 µL 10 mM of both *Frmd4b*^{wt}-F and *Frmd4b*^{wt}-R (Table 2.6) in the mixture, containing 5 µL 10× Buffer I, 1.75 µL 10 mM dNTP, 2 µL template DNA (~500 – 1000 ng), 1 µL 5U/ µL DNA polymerase mix and RNase-free water to make up to a 50 µL volume reaction. The thermal cycling program for PCR amplification is described in Table 2.7. The *Frmd4b*^{Tvrm222} open reading frame was synthesized based on the entire vector containing *Frmd4b*^{wt} sequence using Phusion site-directed mutagenesis to replace the thymine nucleotide with cytosine at the designated site. Specifically, 1.25 µL of both *Frmd4b*^{Tvrm222}-F and *Frmd4b*^{Tvrm222}-R (Table 2.6) were used to mix with 1 µL PfuUltra high-fidelity DNA polymerase (Agilent Technologies, 600380), 1 µL dNTP mix, 5 µL 10× reaction buffer, 1.7 µL (50 ng) amplified *Frmd4b*^{wt} insert and double distilled water to make up to a 50 µL reaction system, followed by the PCR thermal cycling program (Table 2.8). Finally, the amplification product was subject to a *DpnI* digestion of parental supercoiled dsDNA by addition of 1 µL of the *DpnI* restriction enzyme (10 U/µL) to the amplification reaction system, followed by a gentle and thorough mixing of the solution and a one-minute spin down prior to one-hour incubation at 37°C. The synthesized *Frmd4b* product, with an expected size of ~ 7 kb, was visualized on a 0.3% agarose gel stained with crystal violet.

The *Cyth3* coding sequence was amplified by mixing 2.5 µL 10 µM of both *Cyth3*-F and *Cyth3*-R (Table 2.6) with 10 µL 5× high-fidelity buffer, 1 µL 10 mM dNTP, 1 µL Phusion DNA

Table 2.6 Oligo primers for amplification of construct inserts

Oligos	Sequence (5' – 3')	Note
<i>Frmd4b</i> ^{wt} -F	AGCCCGGGCGGGATCATGACAGAAGGCAGGC	<i>Frmd4b</i> ^{wt} amplification
<i>Frmd4b</i> ^{wt} -R	CGGTATCGATAAGCTTCAGACTAATGTTCCAGGCTT- G	
<i>Frmd4b</i> ^{938P} -F	CATCTACAATCCCTTGCCCTCTCCGAGCAGACA	<i>Frmd4b</i> ^{938P} site mutagenesis
<i>Frmd4b</i> ^{938P} - R	TGTCTGCTCGGAGAGGGCAAGGGATTGTAGAGT	
<i>Cyth3</i> -F	GATCCCGGAATTCATGGACGAAGGCGGTG	<i>Cyth3</i> coding sequence amplification
<i>Cyth3</i> -R	GATCGATCAAGCTTCTATTTCTTATTGGCAATCCTC- CTTT	
<i>Frmd4b</i> _F ^{iso1}	GCTTCGTGTGGAACCTTGACC	<i>Frmd4b</i> isoform 1 amplification
<i>Frmd4b</i> _R ^{iso1}	GAACCAGCAGCTCCAGTCTT	
<i>Frmd4b</i> _F ^{iso2}	CACACCCCACAGTGCTGAAT	<i>Frmd4b</i> isoform 2 amplification
<i>Frmd4b</i> _R ^{iso2}	GAACCAGCAGCTCCAGTCTT	
<i>Frmd4b</i> _F ^{iso3}	GAGCGTGGGTATCCTGGTAA	<i>Frmd4b</i> isoform 3 amplification
<i>Frmd4b</i> _R ^{iso3}	GAACCAGCAGCTCCAGTCTT	

Table 2.7 Expand long template PCR system for amplifying *Frmd4b*^{wt}

Temp°C	Time	Note
94	2 min	
94	10 s	10 cycles
52	30 s	
68	4 min	
94	10 s	15 cycles
65	30 s	
68	4 min	
68	7 min	
4		hold

Table 2.8 Site mutagenesis for *Frmd4b*^{938P}

Temp°C	Time	Note
95	30 s	
95	30 s	16 cycles
55	1 min	
68	7 min	
4		Hold

polymerase, 1 μ L (50 ng) cDNA template and RNase-free water to make up to a 50 μ L reaction volume. The product was amplified following the specific thermal cycling conditions in Table 2.9. The *Cyth3* fragment (~ 4 kb in size) was visualized by 0.3% agarose gel, containing crystal violet.

Table 2.9 Amplification of *Cyth3* coding sequence

Temp°C	Time	Note
98	30 s	
98	10 s	25 cycles
65	30 s	
72	90 s	
72	7 min	
4		hold

The amplified products of expected size were excised from the gel and further purified using the QIAquick gel extraction kit (QIAGEN, 28706) based on the following procedures: 1. The DNA fragment visualized by crystal violet was excised using a clean sharp scalpel from the agarose gel; 2. The gel slice was weighed in a transparent tube. Three volumes of the Buffer GQ were added to one volume of the gel; 3. The mixture was incubated at ~70°C for about 10 minutes (or

until the gel slice was completely dissolved), during which the tubes were vortexed every two to three minutes to dissolve the gels until the solution took on a yellow color; 4. The QIAquick spin column was placed in a second collection tube provided by the kit; 5. The dissolved samples were applied to the QIAquick column and centrifuged for one minute for DNA binding; 6. The flow-through was discarded after centrifugation and the QIAquick column was placed on the same collection tube; 7. 0.75 mL of Buffer PE was applied to the QIAquick column to wash the bound DNA through the column by centrifugation for one minute; 8. The flow-through was discarded, followed by an additional centrifugation at $13,400 \times g$ for one minute to remove the remnants of washing buffer from the column; 9. 30 μL of elution buffer was added to the column and incubated for one minute prior to a one-minute centrifugation at $13,400 \times g$ for elution of the DNA from the column.

The pCMV-3Tag-2B (Agilent Technologies) vector in which the *Frmd4b* fragments was to be inserted was linearized by mixing 1 μg vector DNA with the restriction endonucleases $1 \times$ BamHI (NEB R3136)/HindIII (NEB R3104) of 1 μL (1 unit) in total, and 5 μL $1 \times$ NEBuffer 3.1 (NEB B7203S) and NEBuffer 2.1 (NEB B7202S) respectively, for the different restriction enzymes, followed by the incubation at 37°C for one hour (Figure 5). The pCMV-3Tag-1A vector (Agilent Technologies, 1 μg DNA) for inserting the *Cyth3* coding sequence was cleaved by mixing 0.5 μL of EcoRI (NEB R3101) in 5 μL NEBuffer EcoRI, and 0.5 μL of HindIII (NEB R3104) in NEBuffer 2.1 (NEB B7202S) for one-hour at 37°C (Figure 6). The amplified products were inserted into the vectors by ligation using an insert (6 μL): vector (2 μL) ratio no greater than 1:5, and addition of 2 μL $5 \times$ master mix and double distilled water to a total volume of 10 μL . The reaction mixture was placed at 37°C for one hour with rotation. The inserted coding

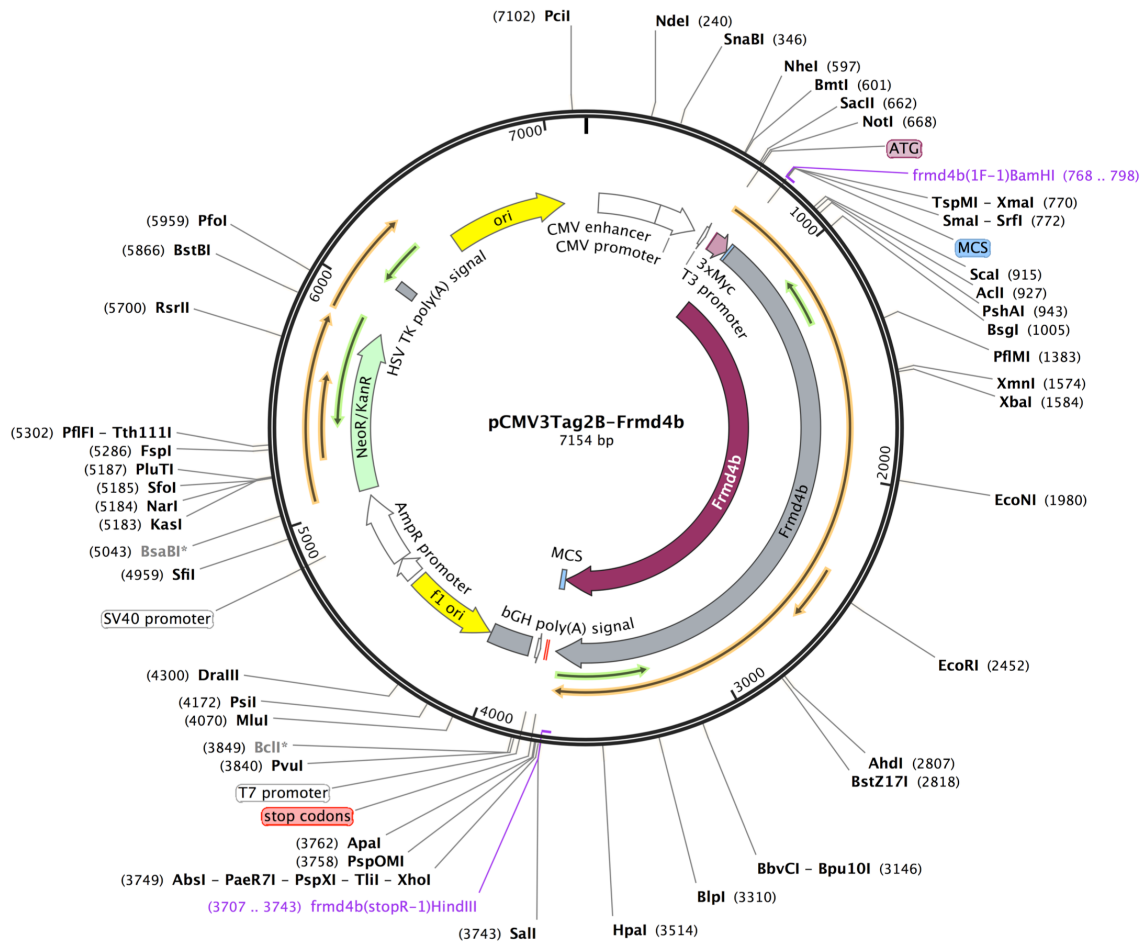


Figure 5. Construction of FRMD4B plasmid vectors for *in-vitro* transfection. The amplicons of *Frmd4b* of both wild type and *TvrM222* variant were inserted in the plasmid vectors. The sites for the insert and the endonucleases are indicated in the diagram.

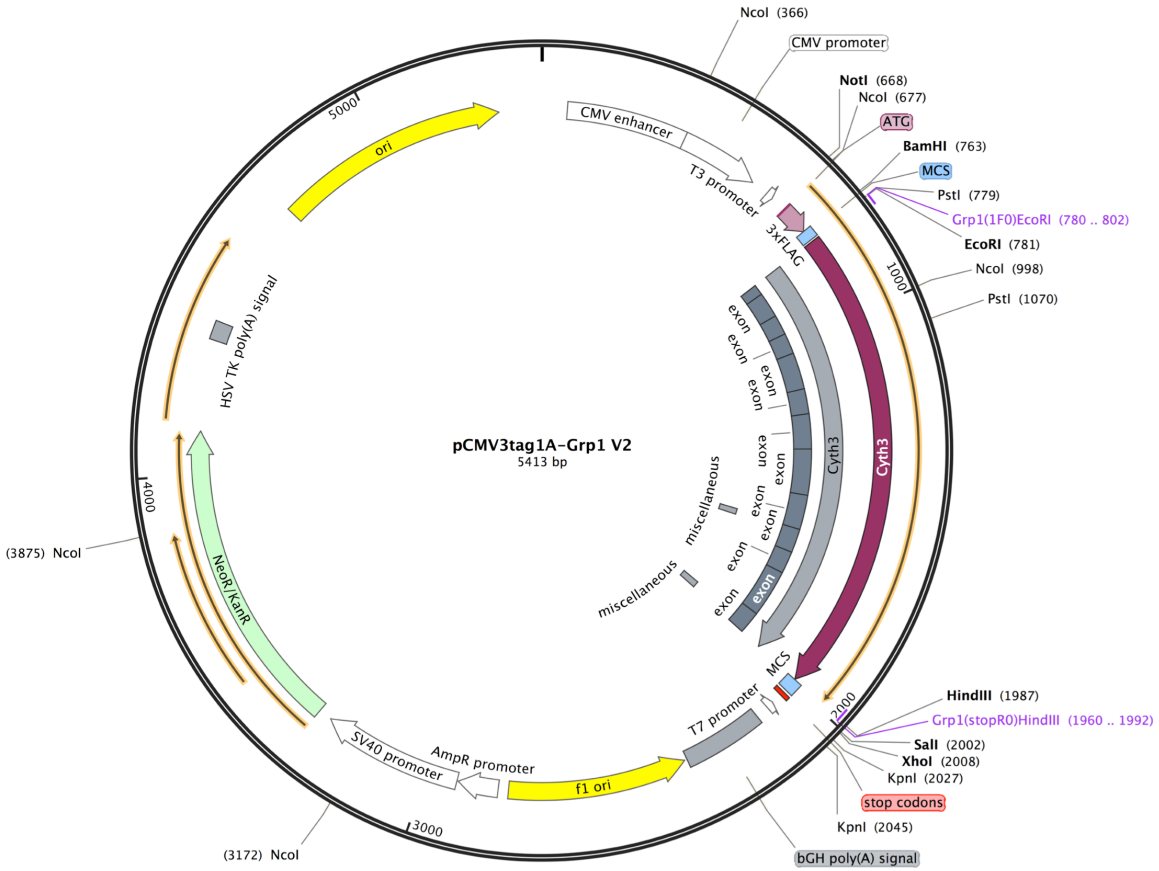


Figure 6. Construction of CYTH3 plasmid vectors for *in-vitro* transfection. The amplicon of *Cyth3* was inserted in the plasmid vectors. Note the site for inserting amplified *Cyth3*.

sequences were subject to verifying their size by electrophoresis in 0.5% agarose gel prior to proceeding to the next step.

Transformation of XL1-Blue supercompetent cells (Agilent Technologies, 200249) with the vector/insert prepared above was performed using the following procedure: 1. 14-mL BD Falcon polypropylene round-bottom tubes were pre-chilled on ice; 2. The XL1-Blue supercompetent cells stored at -80°C were thawed gently by placing on ice before use. When thawed, 150 μL of supercompetent cells were aliquoted to a pre-chilled tube; 3. One μL (~ 50 ng) of *DnpI*-treated DNA was transferred to the aliquot of cells; 4. The transformation reaction was gently swirled and incubated on ice for 30 minutes; 5. Tubes containing the reaction were heat-pulsed in a 42°C water bath for exact 45 seconds; 6. The tube was returned to ice for a two-minute incubation; 7. 0.5 mL autoclaved NZY broth (Thermofisher Scientific: 0.94 mg/L MgCl_2 , 5mg/L NaCl, 0.19 mg/L citric acid anhydrous, 9.8 mg/L peptone 140 and 5 mg/L yeast extract autolyzed low sodium) was added to the transformation solution that was incubated at 37°C for one hour with rotation at ~ 250 rpm; 7. Approximate 100 μL of the transformation mixture was plated on LB agar plates containing 100 $\mu\text{g}/\text{mL}$ ampicillin; 8. The plates were incubated at 37°C overnight; 9. The colonies grown on the LB agar plates were picked with clean toothpicks and placed in tubes containing the culture medium at 37°C with rocking for expansion of the desired colonies. The culture medium was made by mixing 3 μL 1000 \times kanamycin (50 mg/mL) with 3 mL LB solution.

Plasmid DNA was purified using Zyppy plasmid miniprep kit (Zymo Research, D4019) according to the manufacturer's protocol: 1. Six hundred μL of bacterial culture described above was plated in a 1.5 mL microcentrifuge tube; 2. One hundred μL of 7 \times lysis buffer (blue) was added to the tube and mixed by inverting 4-6 times until the opaque solution became clear blue,

no more than 2 minutes, and immediately proceeded to step 3; 3. Three hundred fifty μL of cold neutralization buffer (yellow) was added immediately to the suspended culture and mixed thoroughly until the sample turned yellow to complete the neutralization, at which time a yellowish precipitate could be seen. The samples were inverted for an additional two to three times to ensure complete neutralization; 4. The samples were centrifuged at $13,400 \times g$ for four minutes; 5. ~ Nine hundred μL of supernatant was transferred onto the Zymo-Spin IIN column provided by the kit, without disturbing the cell debris pellet; 6. The column was placed into a collection tube and centrifuged for 15 s; 7. The flow-through was discarded. The column was placed on the same collection tube; 8. Two hundred μL of endo-wash buffer was applied to the column and centrifuged for 30 s; 9. Four hundred μL of Zyppy wash buffer was added to the column and centrifuged for one minute; 10. The column was transferred into a clean 1.5 mL micro-centrifuge tube before adding 30 μL of Zyppy elution buffer directly to the column matrix. The column was allowed to incubate at room temperature for one minute; 11. The plasmid DNA bound to the column was eluted with a 30-second centrifugation. The purified plasmid DNA was subjected to sequencing for validation. The oligo primers used for sequencing *Frmd4b* and *Cyth3* coding sequences are shown in Table 2.10.

The sequence-verified plasmid DNA was grown in larger quantities for subsequent transfections using the QIAGEN plasmid midi kit (QIAGEN, 12145). The specific procedures included: 1. Individual colonies were picked from a freshly streaked selective plate and inoculated in 5 mL LB medium containing 50 $\mu\text{g}/\text{mL}$ kanamycin, which was incubated at 37°C overnight with agitation; 2. The cultured bacterial cell solution was aliquoted. About 100 μL was permanently stored with glycerol at -80°C . The remaining bacterial cells were harvested by centrifugation at $6,000 \times g$ for 15 minutes at 4°C ; 3. The bacterial cells were re-suspended in 4

mL Buffer P1; 3. Four mL Buffer P2 was added and mixed thoroughly by gentle inversion for six times, followed by a five-minute incubation at room temperature (addition of Buffer P2 and

Table 2.10 Oligo primers for sequence verification of the plasmid constructs

Oligos	Sequence (5' – 3')	Note
<i>T7</i>	TAATACGACTCACTATAGGG	
<i>Frmd4bc642F</i>	CCATGGTGGCTTGGTATC	Verification of <i>Frmd4b</i> inserts
<i>Frmd4bc638F</i>	GACTTCCATGGTGGCTTG	
<i>Frmd4bc1358F</i>	CCTGATACAGCAGAAGCT	
<i>Frmd4bc2080F</i>	GCCAGCCCTTACTACACCA	
<i>Frmd4bc2701F</i>	CCACAAATGCTTCTGGGAAC	
<i>Cyth3</i> (511F)	GCCTTTGCATCCCGATAC	Verification of <i>Cyth3</i> insert
<i>Cyth3</i> (995F)	CCAGTCACAAAGGTCAAGT	
<i>Cyth3</i> (675R)	GATGCCTCGGTTTCATGG	
<i>Cyth3</i> (303R)	GACATCCTCTGGGGAGC	

mixing of each sample was completed prior to handling the next sample); 5. Four mL pre-chilled buffer P3 was added to each tube and mixed immediately and thoroughly by vigorously inverting tubes six times, followed by an incubation on ice for 15 minutes; 6. The samples were centrifuged at $18,000 \times g$ at 4°C for 30 minutes. The supernatant containing the plasmid DNA was transferred promptly to a clean tube; 7. The supernatant was centrifuged again at $18,000 \times g$ for 15 minutes at 4°C and decanted. The resulting supernatant was promptly centrifuged again; 8. A QIAGEN-tip 100 was equilibrated by applying 4 mL Buffer QT, allowing the column to empty by gravity flow; 9. The processed supernatant was applied to the prepared QIAGEN-tip by gravity flow; 10. The QIAGEN-tips were washed with 2×10 mL Buffer QC; 11. The bound DNA was eluted from the matrix with 5 mL Buffer QF into a clean 14-mL tube; 12. The DNA was precipitated by adding 3.5 mL room-temperature isopropanol to the eluted DNA, mixed and centrifuged immediately at $15,000 \times g$ for 30 minutes at 4°C . The supernatant was carefully

decanted; 13. The DNA pellet was washed with 2 mL of 70% ethanol stored at room temperature and centrifuged at $15,000 \times g$ for 10 minutes. The supernatant was decanted carefully without disturbing the DNA pellet in a laminar flow hood; 14. The DNA pellet was air dried for about 15 minutes, dissolved in 50 μL of filtered elution buffer; 15. One μL of eluted DNA was diluted in 1:10 with elution buffer to determine the DNA yield, using the NanoDrop 2000.

2.4.3 Cell transfection

HEK-293T cells were plated in 60 mm petri dishes at the density of 1.3×10^6 . For plating COS-7 cells, cover slips were coated with 100 mM polylysine solution diluted with borate buffer for greater than 30 minutes in a laminar flow hood. The slides were thoroughly washed with $1 \times$ PBS before plating the cells. COS-7 cells were plated on pre-treated cover slides at the density of 2×10^5 . Both cell types were cultured overnight, no more than 24 hours prior to transfection. The culture medium was replaced with fresh DMEM prior to transfection. Cells were transfected within 24 hours after being plated when 70 – 80% confluence was reached. Transfection mixture for HEK-293T cells was prepared by mixing 500 μL Opti-MEM (Thermo Fisher Scientific, 31985062), 15 μL of TransIT-2020 (Mirus, MIR 5400) that was pre-warmed at room temperature and gently vortexed, as well as 5 μg of plasmid DNA (2.5 μg *Frmd4b* plus 2.5 μg *Cyth3* for co-transfection). For COS-7 cells, the transfection mixture ratio was adjusted to 100 μL of Opti-MEM, 3 μL TransIT-2020 and 1 μg of plasmid DNA (evenly divided when co-transfection of multiple genes was necessary). The mixture was gently mixed by pipetting and incubated at room temperature for 20 – 30 minutes. The transfection mixture was added drop wise gently to the cells, followed by incubation at 37°C for about 24 hours. The culture media containing transfection mixture was discarded 24 hours later by replacing it with fresh DMEM media. The cells were allowed to recover in the fresh media prior to starvation, at which time the

cells were supplemented with serum-free DMEM and incubated for about 18 hours (overnight) at 37°C. After starvation, the cells were supplemented with 100 nM insulin and incubated for no more than five minutes for measurement of ARF6 activation (GTP/GDP exchange is transient in response to the extracellular cues). For immunofluorescence and other SDS-PAGE analyses, the insulin treatment lasted ~20 minutes. The control group without insulin treatment was supplied with serum-free DMEM.

2.4.4 Immunofluorescence microscopy of transfected cells

Transfected COS-7 cells with or without insulin treatment were fixed with 2% PFA for no more than 15 minutes. After removal of the fixative, COS-7 cells were washed three times with 1× PBS. A 0.1% SDS solution was gently added to the cells on the cover slips and incubated for about five minutes at room temperature to permeabilize the cells. Subsequently, the cells were carefully and thoroughly washed three to five times with 1× PBS. The fixed cells were then incubated with blocking solution containing 5% NDS for one hour. The primary antibodies diluted with blocking solution was added to the cells and incubated overnight at 4°C. The next day, the cells were carefully washed three times with 1× PBS prior to incubation with a secondary antibody at room temperature for one hour. The secondary antibody solution was carefully removed after the incubation. COS-7 cells were washed two times with 1× PBS, followed by counterstaining with 1:500-diluted DAPI for one minute. The cells were washed two more times with 1× PBS prior to mounting cells with mounting media (Thermo Fisher Scientific) and sealing on the slides. The samples were dried at room temperature before examination with a Leica SP5 confocal microscopy.

2.5 SDS-PAGE analyses

2.5.1 Western blot

Whole eyes were enucleated after mice were euthanized by CO₂ asphyxiation and cervical dislocation in accordance with an IACUC-approved protocol. Eyecups were prepared by removing the anterior segment and vitreous of the eye. The dissected eyecups were immediately placed in a modified radioimmunoprecipitation (RIPA) assay buffer (65 mM Tris, pH 7.4; 1% NP40; 0.9% NaCl; 0.25% Na-deoxycholate and 1 mM EDTA), containing 1· protease inhibitor cocktail (Sigma-Aldrich, P8340) and 1· phosphatase inhibitors, which contained 20 mM sodium fluoride, 100 mM sodium pyrophosphate, 100 mM sodium orthovanadate, 100 mM ammonium molybdate and Phenylmethanesulfonyl fluoride (Sigma-Aldrich, P7626). The tissue was thoroughly homogenized using a dounce homogenizer. The lysates were subsequently centrifuged at 13,000 × g at 4°C for 15 minutes. The supernatant was retained without disrupting the pellet at the bottom of the tube.

The supernatant was checked for protein concentration by Direct Detect Infrared Spectrometer (Millipore Sigma, DDHW00010-WW) prior to being loaded on Tris-Glycine eXtended (TGX) precast gels (BIO-RAD, 4569034, 35; 4561094, 95) for electrophoresis. Selection of the polyacrylamide concentrations of the gels depended on the molecular weight of target molecules to be assessed. Dual colored protein standard ladder (BIO-RAD, 1610374) was used for detecting molecular weight of loaded samples. The gel was assembled in a Mini-PROTEAN tetra vertical electrophoresis apparatus with 1× diluted 10× premixed electrophoresis buffer (double distilled water diluent), containing 100 mM Tris, 100 mM Tricine and 0.1% sodium dodecyl sulphate polyacrylamide (SDS), pH 8.3. The samples were electrophoresed at 200V for 30 minutes. When electrophoresis was completed, the gel was carefully pressed onto a

nitrocellulose membrane for protein transfer using the Trans-Blot Turbo Transfer system (BIO-RAD).

The nitrocellulose membrane to which the proteins were transferred was incubated for 40 minutes on a rotator in 4% blocking solution with Nestle milk powder diluted in 1 × Tris-buffered saline (TBS, 50 mM Tris-Cl, 150 mM NaCl, pH 7.6) containing 0.5% Triton X-100 (TBST), at room temperature, followed by an overnight incubation with primary antibodies diluted to a desired concentration in 3 – 5% milk at 4°C on a rocker (see Table 2.11). After an overnight incubation, the membrane was washed for three times with five minutes each using 1 × TBST on a rocker. After the wash, the membrane was incubated with gentle agitation for approximately four hours with secondary antibodies conjugated with horseradish peroxidase that would specifically detect the species in which the primary antibodies were generated. The membrane was then washed three times with TBST for five minutes each. The washed membrane was then subject to a three-minute reaction with Clarity Western ECL Blotting Substrates (BIO-RAD; 1705060) containing western peroxide reagent and western lumino/enhancer reagent for immunodetection. The nitrocellulose membranes were stripped for re-probing by submerging it in 1 × ReBlot Plus Strong Antibody Stripping Solution (Merck Millipore; 2504) according to the manufacturer's protocol.

2.5.2 Co-immunoprecipitation

To precipitate protein extracts from HEK-293T cell, the FLAG immunoprecipitation kit (Sigma-Aldrich, FLAGIPT1) was used. Prior to use, all kit solutions were thawed and mixed to homogeneity. 2 × sample buffer (S8684), containing 125 mM Tris HCL, pH 6.8 with 4% SDS, 20% (v/v) glycerol and 0.004% bromophenol blue was prepared. In order to prepare 5 µg/µL of a 3 × FLAG peptide (F4799) solution, one mg 3 × FLAG peptide was added to 40 µL 10 × wash

buffer (W0390), made up of 0.5 M Tris HCl, pH 7.4 with 1.5 M NaCl. 160 μ L of distilled water was added to the peptide solution when it was completely dissolved. Five mL of 1 \times wash buffer was prepared by adding 0.5 mL of 10 \times wash buffer to 4.5 mL sterile deionized water and mixing thoroughly. About 2 μ L of the FLAG-BAP fusion protein (P7582) stock solution was diluted to a concentration of 50 ng/ μ L with 1 \times wash buffer.

When all the solutions were ready, the transfected HEK-293T cells were harvested when they reached ~70 – 80% confluence with or without being treated with insulin. The culture medium was discarded; the cells were rinsed with 1 \times PBS without dislodging the cells. The PBS was discarded and replaced with 1 \times lysis buffer (L3412), containing 50 mM Tris HCl, pH 7.4 with 150 mM NaCl, 1 mM EDTA and 1% Triton X-100 and 1 \times protease inhibitor (Sigma-Aldrich P8340). The cells in lysis buffer were incubated for about 20 minutes on a rotator and scraped into a 1.5 mL tube. The cell lysate was centrifuged at 12,000 \times g for 10 minutes. Subsequently, the supernatant was carefully collected and transferred to a pre-chilled 1.5 mL tube. The supernatant was aliquoted, with 25 – 50 μ L of the supernatant or the post-nuclear supernatant (PNS) fraction reserved as control, and the remaining supernatant used for the co-immunoprecipitation assay.

The ANTI-FLAG M2-Agarose affinity gel (A2220) was thoroughly and uniformly suspended. The ratio of suspension to packed gel volume was 2:1. Forty μ L of resin was immediately transferred by pipette tips (enlarged ends) into its suspension buffer in a fresh test tube to allow a homogenous dispersal of resin. The resin was centrifuged at 8,000 \times g for 30 s. The supernatant was carefully removed using a pipette tip with a small bore to prevent disturbance of the sediment. The gel was washed five times with 500 μ L of 1 \times wash buffer each to completely remove the glycerol contained in the gel. After carefully decanting the wash

buffer, 400 μ L of cell lysate was added to 600 μ L of lysis buffer and mixed with the resin. The samples were mixed gently on the rocker overnight at 4°C. The next day, the resin containing cell lysate was centrifuged at 8,200 \times g for 30 s. The supernatant collected with narrow-end pipette tips contained the unbound proteins. The resin was washed three additional times with 0.5 mL of 1 \times wash buffer. In order to elute the FLAG-fusion proteins, 100 μ L of 3 \times FLAG elution buffer (150 ng/ μ L) was added to the resin in the tubes. The samples were incubated for 30 minutes at 4°C on a rocker. After the incubation, the resin was centrifuged at 8,200 \times g for 30 s. The supernatant that represented the bound protein content was transferred to fresh tubes, without disturbing the resin pellet at the bottom.

Protein samples were denatured, and SDS-PAGE analysis was performed as described above.

2.5.3 Subcellular fractionation assay

The transfected HEK-293T cells grown in petri dishes with or without insulin treatment were washed with 1 mL pre-chilled 1 \times PBS. The cells were scraped from the petri dish and harvested into a 1.5 ml micro-centrifuge tube with cold PBS. The samples were centrifuged at 8,000 \times g at 4°C for 5 minutes. The supernatant was carefully decanted without disturbing the pellet and replaced with 500 mL HEPES (4-(2-hydroxyethyl)-1-piperazineethanesulfonic acid) buffer, containing 115 mM NaCl; 1.2 mM CaCl₂; 1.2 mM MgCl₂; 2.4 mM K₂HPO₄; 20 mM HEPES and protease inhibitor (Roche; 11836170001) for homogenization. The cells were lysed with a motorized dounce homogenizer. The cell lysate was centrifuged at 13,400 \times g at 4°C for 15 minutes. After centrifugation, the supernatant was carefully removed and placed in another clean 1.5 mL tube. The remaining pellet containing the nuclear content and heavy membranes, was passed through a fine gauge needle, followed by two washes with the HEPES buffer. The

supernatant, which contained the light membranes including plasma membrane, was collected as the PNS fraction, and aliquoted for subsequent use. A portion of the PNS was subject to ultra-centrifugation (Beckman Ultracentrifuge) at $100,000 \times g$ for 30-45 minutes. The supernatant was collected carefully into a new tube and labeled as the cytosolic content (S100). The pellet was washed with HEPES buffer and centrifuged at $100,000 \times g$ for another 15 minutes. The supernatant was discarded and the resultant pellet was re-suspended and collected as the membrane protein content (P100).

Subcellular fractionation of animal tissues followed similar procedures. The tissues were dissected from one-month old animals with desired genotypes. Eyecups harvested from two individual mice of the same genotype were pooled together to ensure sufficient protein yield. Tissues cut into small pieces were homogenized in 1 mL 1M HEPES buffer using a Caframo BDC 2010 reversing digital variable-speed stirrer (N552). The tissue lysate was subject to centrifugation at $13,400 \times g$ at 4°C for separation of the PNS from the heavy nuclear content. The PNS was subject to ultra-centrifugation at $100,000 \times g$ at 4°C to separate the S100 fraction from the P100 fraction. The P100 fraction was washed and re-suspended with HEPES buffer.

Proteins comprising the PNS, S100 and P100 fractions were denatured in $4 \times$ Bolt LDS sample buffer (Thermo Fisher Scientific, B0007) mixed with $10 \times$ Bolt sample reducing reagent (Thermo Fisher Scientific, B0009) at 75°C for 15 minutes, and loaded onto a 4% - 10% TGX precast gradient gel for western blotting analysis as described above.

2.5.4 GTPase-activation assay

ARF6 activation both *in vitro* and *in vivo* was assessed using an ARF6 activation assay kit (Abcam, ab211171). The procedure was carried out using the protocol provided by the manufacturer with minor modifications. For the *in vitro* measurement, HEK-293T cells were

cultured and transfected on 60 mm petri dishes by following the same protocol aforementioned. In order to lyse the cells: 1. 1× Assay Buffer was prepared by diluting 5× Assay Buffer with double distilled water; 2. The cells were harvested when they reached ~70 – 80% confluence and were lysed immediately after treatment with 100 nM insulin for less than 5 minutes; 3. The cells were placed on ice and washed twice in pre-chilled 1× PBS; 4. The cells were re-suspended in 1 mL 1× Assay Buffer, containing 1· protease inhibitor (Sigma-Aldrich SRE0055); 5. The petri dishes remained on ice for 15 minutes; 6. The cells were scraped off the petri dishes, and transferred to 1.5 mL tubes on ice; 7. The samples were centrifuged at $13,400 \times g$ at 4°C to remove cell debris; 8. The supernatant was collected after centrifugation and transferred to a new tube and placed on ice.

For assaying ARF6 activation *in vivo*, eyecups were dissected from 10-day old mice and homogenized as follows: 1. The eyecups were washed with pre-chilled 1× PBS, followed by re-suspension in 1 mL 1× Assay Buffer; 2. The tissue was homogenized with a dounce homogenizer on ice; 3. The lysates were centrifuged at $13,400 \times g$ for 10 minutes at 4°C ; 4. The supernatant or PNS was collected, and transferred to a new tube and placed on ice.

In order to precipitate the protein in the PNS fraction: 1. The supernatant was aliquoted. One hundred μL of the supernatant or PNS was reserved to serve as control. The remaining supernatant was made up to a volume of 1 mL with 1× Assay Buffer; 2. GGA3 protein binding domain (PBD) agarose bead slurry was thoroughly re-suspended by vigorous vortexing; 3. Forty μL of re-suspended GGA3 PBD bead slurry was swiftly added to each sample tube by using an enlarged-end pipette tip; 4. The mixture was incubated at 4°C for one hour on a rocker; 5. The mixture was centrifuged at $13,400 \times g$ for one minute; 6. The supernatant, which contained the unbound portion of ARF6, was carefully aspirated without disturbing the bead layer and saved;

7. The bead pellet was washed three times with 500 μ L of 1 \times Assay Buffer; 8. After removal of the Assay Buffer, the bead pellet was re-suspended in 40 μ L of 2 \times SDS-PAGE sample buffer, and boiled at $>90^{\circ}\text{C}$ for about seven minutes; 9. The samples were centrifuged at $13,400 \times g$ for 30 s to elute the GTP-bound ARF6. Subsequently, the protein samples, including PNS, unbound and bound were loaded onto a Criterion TGX 4-12% precast gel for western blotting analysis following routine procedures.

2.6 Antibodies

The primary antibodies used in the relevant studies are summarized in Table 2.11.

2.7 Imaging processing and statistical analyses

The ImageJ/FIJI software was used for processing all images, for measuring thickness of ONL, as well as for quantifying western blotting results. The statistical significance was calculated by two-way ANOVA with post-hoc Tukey's test and by one-way ANOVA with post-hoc Tukey's test for multiple comparisons (for comparison of three groups of samples) as well as student-*t* test (for comparison of two group of samples). Each experimental group was based on at least three independent samples. Results are reported as mean \pm S.D. $P < 0.05$ was reported as statistically significant.

Table 2. 11 Antibodies

Antibody	Manufacture	Stock No.	Species	Usage
AKT, pan	Cell Signaling	#4961	rabbit	WB*: 1:1000 – 2000
AKT, phospho (Ser473)	Cell Signaling	#9271	rabbit	WB: 1:1000 – 2000
ARF6	Abcam	ab211171	mouse	WB: 1:1000
ATP1A1	Novus Biological	NB300-146SS	mouse	WB: 1:1000
β -catenin	Santa Cruz	sc-1496	goat	WB: 1:1000; IHC**: 1:200 (PFA fixation)
Cone-arrestin	Millipore	AB15282	rabbit	WB: 1:1000; IHC: 1:200 (PFA fixation)
FRMD4B	Dr. Czech's lab	n/a	rabbit	WB: 1:500
GAPDH	Cell Signaling	#2118	rabbit	WB: 1:1000 – 2000
GFAP	Dako	Z0334	rabbit	IHC: 1:200 (PFA [^] fixation)
GS	Abcam	ab73593	rabbit	WB: 1:1000; IHC: 1:200 (PFA fixation)
FLAG-Tag	Sigma-Aldrich	F1804	mouse	WB: 1:2000; IHC: 1:200 (PFA fixation)
MYC-Tag	Cell Signaling	#2276	mouse	WB: 1:2000; IHC: 1:200 (PFA fixation)
Opsin, blue	Chemicon	AB5407	rabbit	WB: 1:1000; IHC: 1:200 (PFA fixation)
P-cadherin	Santa Cruz	sc-7893	rabbit	IHC: 1:200 IHC: 1:200 (PFA fixation)
PH3	Abcam	ab47297	rabbit	IHC: 1:200 (PFA fixation)
PNA	Vector Lab	B-1075	biotin	IHC: 1:200 (PFA fixation)
SOX9	Millipore	AB5535	rabbit	WB: 1:500; IHC: 1:200 (PFA fixation)
ZO-1	Abcam	ab59720	rabbit	WB: 1:1000; IHC: 1:200 (acetic acid: methanol fixation)

WB*: Western Blot; IHC**: Immunohistochemistry; ^: paraformaldehyde

CHAPTER 3

RESULTS

3.1 ENU-induced *Tvrm222* variant as a genetic suppressor of *rd7* dysplasia

To identify genetic modifiers of *Nr2e3^{rd7/rd7}*, we conducted a sensitized mutagenesis screen using the chemical mutagen, ENU, on homozygous B6.Cg-*Nr2e3^{rd7}*/J mutant mice. A number of lines were established, including *Tvrm222*, *Tvrm233*, *Tvrm240* and *Tvrm269* (Table 3.1) with modified ocular phenotypes. In particular, the mice from one of these lines, *Tvrm222*, displayed a significant reduction in number of retinal spots compared to B6.Cg-*Nr2e3^{rd7}*/J homozygotes (Figure 7 A-C, G; note: all of the *Tvrm222* mice referred to in this study were homozygous for both *rd7* and *Tvrm222* unless otherwise indicated). Consistent with the fewer retinal spots observed by fundus imaging, the number of retinal folds observed by histology were remarkably reduced in *Tvrm222* retinas as well (Figure 7F), compared to *rd7* homozygotes in which retinal dysplastic lesions are abundant (Figure 7E). The retinal folds are widespread in *Nr2e3^{rd7/rd7}* mouse retinas at two weeks of age compared to those found in *Tvrm222* retinas (Figure 8 A-C) and also at six weeks and six months of age (Figure 8 D-I), suggesting that the reduction in retinal folds in *Tvrm222* mice occurs during development rather than merely a consequence of photoreceptor cell death as the mutant ages. It is worth noting that the penetrance was not 100% within these populations. It was estimated that approximately 80% of *Tvrm222* mice show a significant reduction in fundus retinal spots and photoreceptor dysplasia, while the remaining 20% mice still displayed some pan-retinal spots (Figure 7G).

In addition to the morphological characterization, we also attempted to examine whether the outer retinal function in *Tvrm222* mice was ameliorated as well. According to the assessment

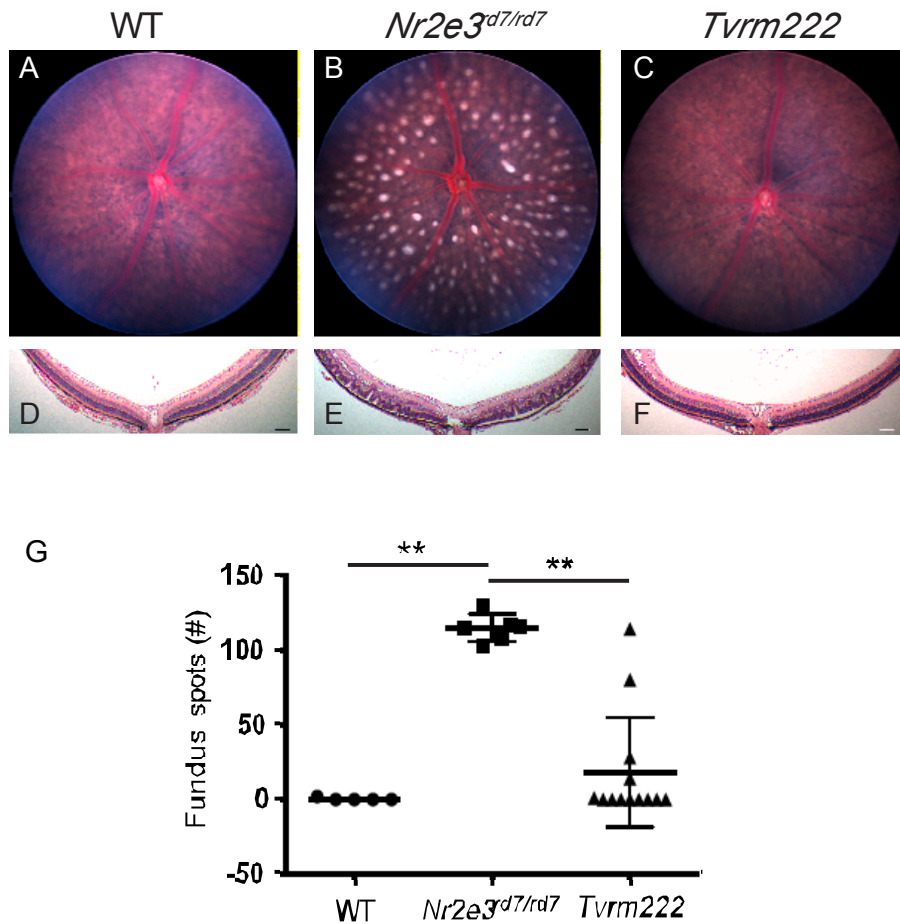


Figure 7. Reduction of *rd7*-associated pan-retinal spots in *Tvrn222* mice. (A-C) Fundus images (quantification of the numbers of dysplastic lesions observed in fundus images of the central retina are shown in G) and (D-F) representative sections of the posterior eye stained with Hematoxylin and Eosin (H&E) from one-month-old wild type (WT), *Nr2e3^{rd7/rd7}*, and *Nr2e3^{rd7/rd7} Frmd4b^{Tvrn222/Tvrn222} (Tvrn222)* mice. Note the spots in the *rd7* fundus (B) and the corresponding retinal folds or lesions shown in histological sections (E). Scale bar = 100 μ m. For quantifications in (G), the results are mean \pm S.D., n = 5 (WT), 6 (*rd7*) or 13 (*Tvrn222*); **: p<0.0001 (one-way ANOVA, post-hoc Tukey's test).

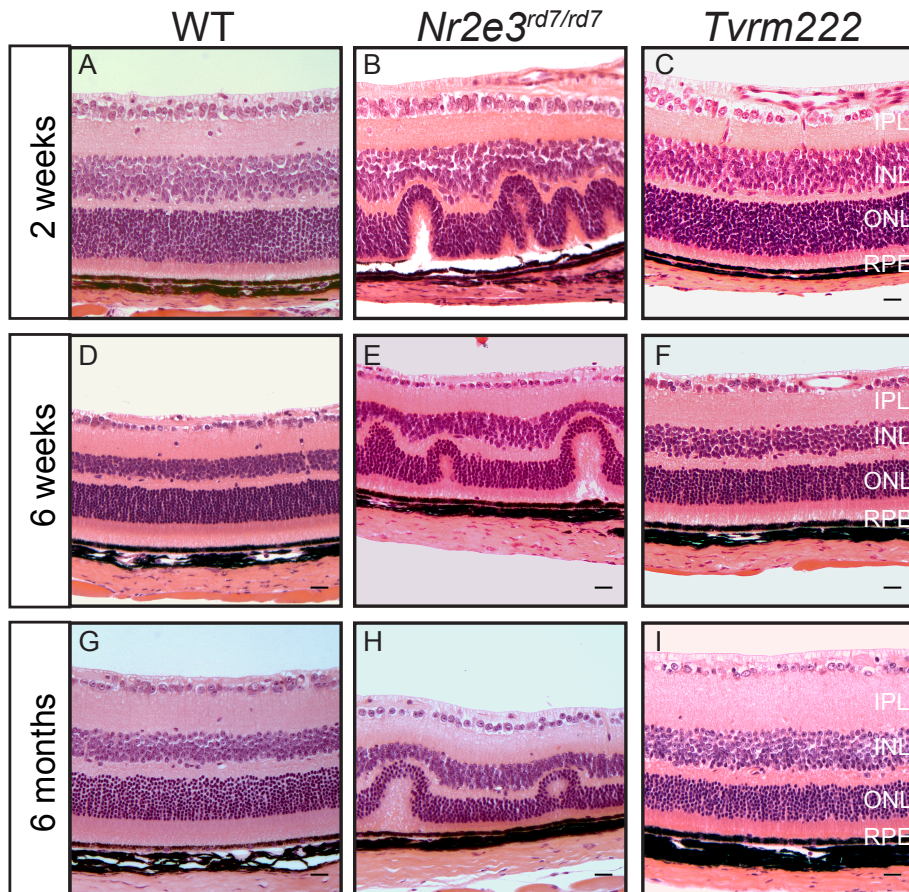


Figure 8. Suppression of *rd7*-associated anatomic anomalies associated in *Tvrn222* mice. Retinal lamination from two-week-old (A-C), six-weeks-old (D-F) and six-month-old (G-I) WT, *Nr2e3^{rd7/rd7}*, and *Tvrn222* mice are shown in H&E stained sagittal sections through the ora serrata and optic nerved head. Note the retinal undulations in the *Nr2e3^{rd7/rd7}* retinas and the relative absence of retinal folds in the *Tvrn222* mice at all ages surveyed. Scale bar = 20 μ m. IPL: inner plexiform layer, INL: inner nuclear layer, ONL: outer nuclear layer, RPE: retinal pigment epithelium

Table 3.1 Lines established from *Nr2e3*^{rd7/rd7} mutagenesis screen

Line ID	Mode	Phenotype [†]	Epistatic	Comment
<i>Tvrm222</i>	Dominant	Significant reduction of <i>rd7</i> spots	Yes	<i>Frmd4b</i> c.2812T>C; p. S938P
<i>Tvrm233/237/238</i> [†]	Dominant	Significant reduction of <i>rd7</i> spots	Yes	HTS*
<i>Tvrm240/249</i> [†]	Dominant	Reduction of <i>rd7</i> spots	Yes	HTS*
<i>tvrm269</i> ^{††}	Recessive	Reduction of <i>rd7</i> spots	Yes	HTS*

[†]Currently at N4. ^{††}Currently at N3. *HTS: high throughput sequencing complete

by ERG, no marked scotopic (0.25 cd.s/m²) or photopic (10 cd.s/m²) ERG improvement was recorded in *Tvrm222* mice in comparison to *Nr2e3*^{rd7/rd7} at ~1.5 months (Figure 9 A-D), despite a decline in *rd7* photoreceptor response compared to the wild type. Since a late-onset retinal degeneration was also documented in both ESCS patients and *Nr2e3*^{rd7/rd7} mice, we additionally measured the thickness of ONL. The results revealed an age-related degeneration found in both *Nr2e3*^{rd7/rd7} and *Tvrm222* mice, which is in contrast to that in the wild type mice at the ages surveyed (Figure 10 A, B). These lines of data imply that the modifying effect of *Frmd4b*^{*Tvrm222*} allele on *rd7*-associated dysplasia was achieved through an alternative pathway in lieu of directly influencing the aberrant cellular composition due to lacking functional NR2E3.

3.2 *Tvrm222* variant is able to normalize retinal structure in *rd7* mouse eyes

3.2.1 *Tvrm222* variant does not affect retinal cell proliferation or Müller gliosis

NR2E3 is a transcription factor that promotes the differentiation of retinal progenitor cells to rods by inhibiting cone-specific genes. It was once proposed that loss of NR2E3 function causes an over-proliferation of blue cones in *rd7* retinas and results in formation of dysplastic folds. Hence, we hypothesized that the modifying effect of the *Frmd4b*^{*Tvrm222*} variant on photoreceptor dysplasia is achieved by affecting cell proliferation. Phosphorylated histone 3 (PH3) was used to label mitotic cells on postnatal day-5 mice, a time at which retinal cells

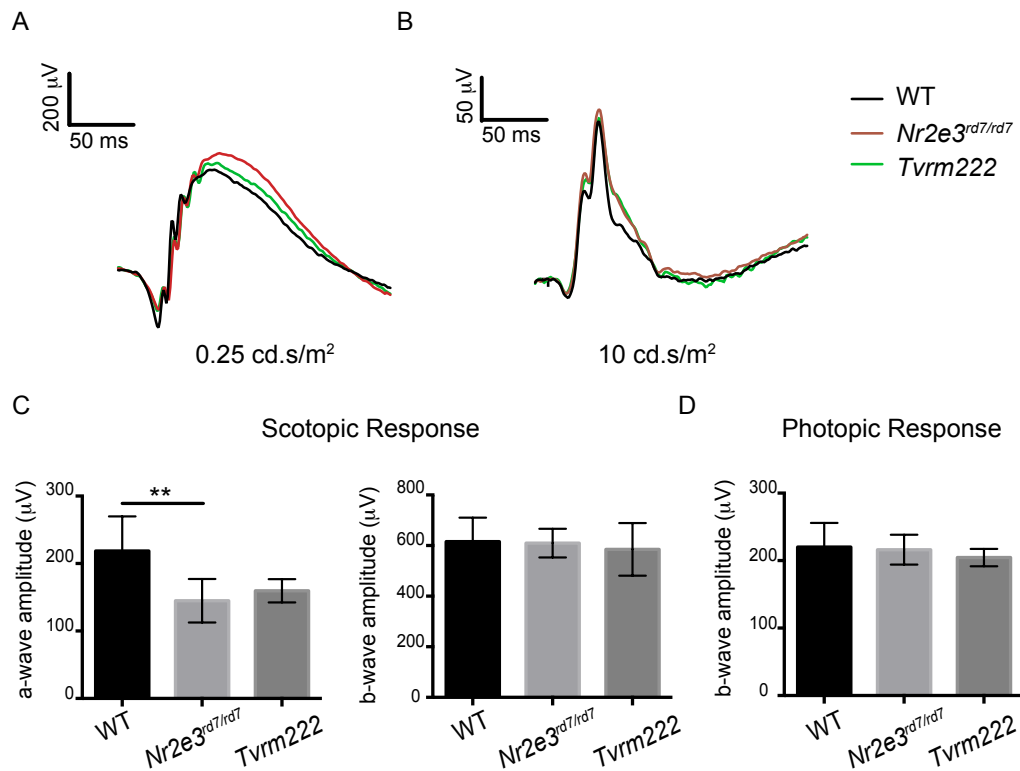


Figure 9. ERG analysis on outer retinal function of both *Nr2e3^{rd7/rd7}* and *Tvrn222* mice.

(A, B) ERG recordings show rod (flash stimuli; 0.25 cd. s/m²) and cone (10 cd. s/m²) responses of six-week-old wild type (black), *Nr2e3^{rd7/rd7}* (red), and *Tvrn222* (green) animals. (C, D) The amplitudes of ERG responses exposed to a range of stimuli were quantified. The results are mean ± S.D. n = 12 (WT), 14 (*Nr2e3^{rd7/rd7}*), and 4 (*Tvrn222*); **: p < 0.01 (one-way ANOVA, post-hoc Tukey's test).

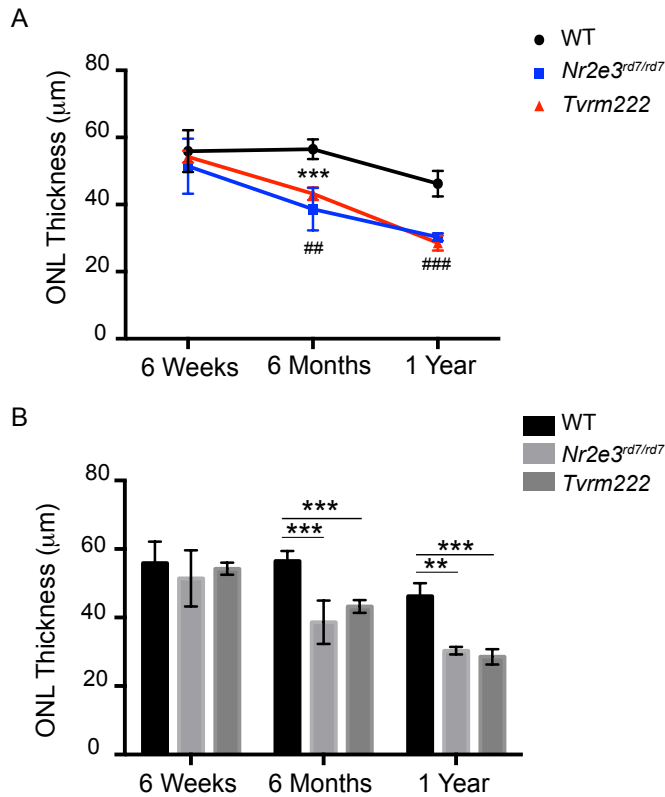


Figure 10. Measurement of the ONL thickness in *Nr2e3^{rd7/rd7}* and *Tvrn222* mice with age.

The thickness of the outer nuclear layer (ONL), ~350 µm from the optic nerve was measured based on H&E stained sections. The results are mean ± S.D. For WT, n = 5 (six weeks), 8 (six months), and 3 (one year); For *Nr2e3^{rd7/rd7}*, n = 4 (six weeks), 12 (six months), and 4 (one year); For *Tvrn222*, n = 7 (six weeks), 5 (six months), and 4 (one year); For determining age-related reduction of ONL thickness (A), *** (*rd7*: six weeks vs. six months): p=0.0007; ## (*Tvrn222*: six weeks vs. six months): p = 0.0064, ### (*Tvrn222*: six months vs. one year): p = 0.0009. For comparing ONL thickness among the mice of different genotypes at certain age (B), **: p<0.01, ***: p<0.001. (two-way ANOVA, post-hoc Tukey's test).

undergo proliferation. Consistent with previous reports, our results showed an increased number of proliferative retinal cells in *Nr2e3*^{rd7/rd7} mice compared to their wild type counterparts (Figure 11 A-D). However, *Tvrm222* retinas bearing the *Frmd4b*^{*Tvrm222*} allele also displayed an increase in PH3-positive cells that was similar to that found in *Nr2e3*^{rd7/rd7} mouse retinas (Figure 11 E, F). A significant increase in the number of proliferative retinal cells was observed in both *Nr2e3*^{rd7/rd7} and *Tvrm222* eyes compared to the wild type (Figure 11 G). The level of blue opsin in wild type, *Nr2e3*^{rd7/rd7} and *Tvrm222* mouse retinas further validated this observation as slight increase in blue opsin-labeled cells were detected in *Nr2e3*^{rd7/rd7} mouse retinas compared to wild type retinas, while the *Frmd4b*^{*Tvrm222*} variant failed to significantly reduce the number of blue opsin positive cells (Figure 11 H-J). Likewise, western blotting analysis of retinal extracts from either *Nr2e3*^{rd7/rd7} or *Tvrm222* showed a similar level of expression of blue opsin levels (Figure 11 K). Taken together, our results reveal that *Tvrm222*-mediated suppression of *rd7* dysplasia does not repress excessive proliferative retinal cells or modify aberrant blue cone photoreceptors.

Furthermore, we decided to morphologically characterize the cone photoreceptors as it was reported to be implicated in initiating formation of dysplastic lesions in mouse retinas (98). The mouse retinas were stained with arrestin 3 (ARR3, a.k.a cone arrestin), a marker for cone cell body and peanut agglutinin (PNA), which specifically stains plasma membrane near ISs and OSs. The results showed abundant mislocalized cone photoreceptors in the ONL in both *Nr2e3*^{rd7/rd7} and *Tvrm222* retinas, in contrast to those in wild type retinas, which are predominantly localized near the apical terminus of the ONL (Figure 11 L-N). Furthermore, increased number of ovoid-shaped cone IS/OS in both *Nr2e3*^{rd7/rd7} and *Tvrm222* retinas was observed, compared to the elongated cone IS/OS in wild type retinas (Figure 11 O-Q). Furthermore, by assaying the expression level of ARR3, we failed to note a significant difference between the *Nr2e3*^{rd7/rd7} and

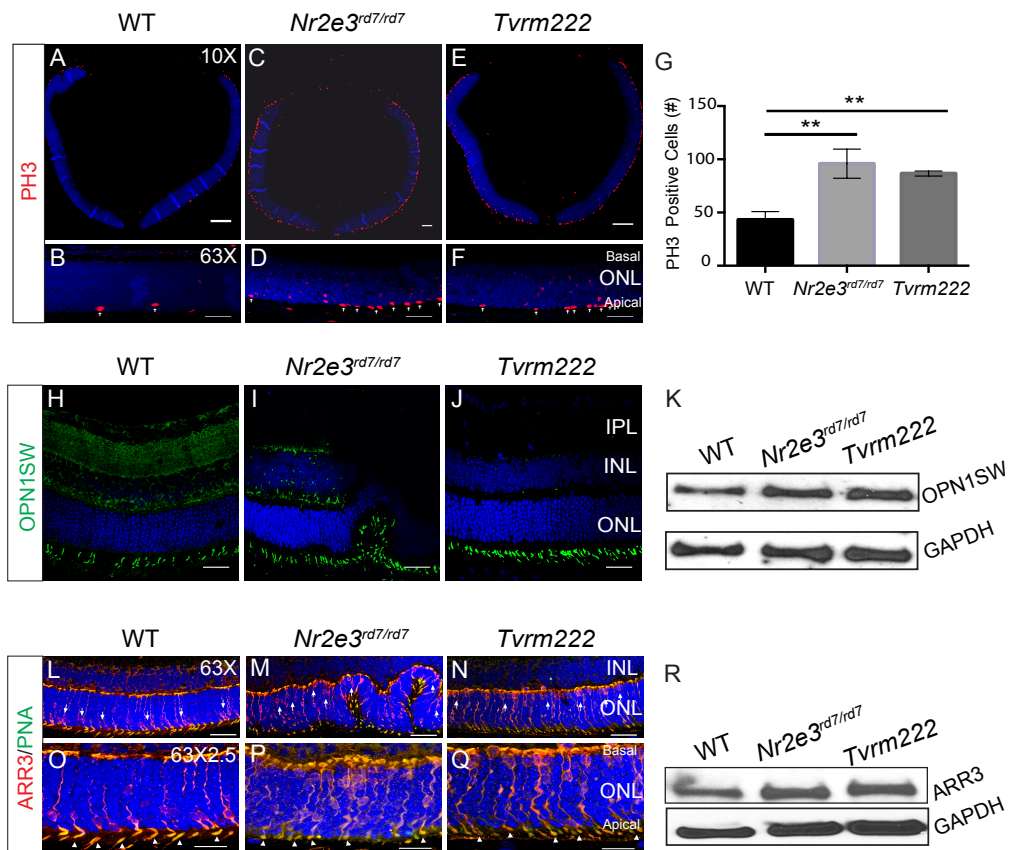


Figure 11. Impact of *Tvrm222* modification on (photoreceptor) cells in *rd7* retinas. WT, *Nr2e3^{rd7/rd7}* and *Tvrm222* mice were assessed for: (A-F) Cell proliferation in five-day-old (P5) retinas by immunofluorescence with phosphorylated histone (PH) 3, a mitotic marker. Arrows indicate proliferative retinal cells. Stained cells were counted in a single section from individual mice (G); The results are mean \pm S.D. $n=3$ for each mouse strain. **: $p<0.01$ (one-way ANOVA with post-hoc Tukey's test for multiple comparisons). Scale bar = $200\mu\text{m}$ (10 \times) or $20\mu\text{m}$ (63 \times); (H-J) Blue-cone opsin (OPN1SW) expression in the retina by immunofluorescence staining and western blot (K) with antibodies of OPN1SW and GAPDH as the loading control. Scale bar = $20\mu\text{m}$. (L-Q) The morphology of cone cell body (arrestin 3, ARR3) and sheath (peanut agglutinin, PNA) by immunofluorescence staining and western blot with antibodies against ARR3 and GAPDH as the loading control (R). Note the displacement of cone cells (arrows) and ovoid-shaped cone cell sheath (arrowheads). Scale bar = $20\mu\text{m}$ (20 \times) or $10\mu\text{m}$ (63 \times 2.5);

Tvrm222 mice (Figure 11 R). Collectively, these results indicate that the *Tvrm222* modifier does not correct the developmental defects of (cone) photoreceptors seen in *Nr2e3^{rd7/rd7}* retinas.

Müller gliosis, another hallmark of dysplastic lesions in retina was also examined. Anti-SRY-Box 9 (SOX9), an adult Müller cell marker, anti-glutamine synthetase (GS), a protein that is exclusively expressed by Müller glia (172) and anti-gial fibrillary acidic protein (GFAP) that labels activated glial cells, were used to detect potential alterations in Müller glial cells. No significant difference was noted in terms of localization of somata of Müller cells in the inner nuclear layer among three different genotypes (Figure 12 A-F), as well as the expression level of SOX9 assayed by western blot (Figure 12 G). Detection of GS-positive cells, shown by immunofluorescence staining (Figure 12 H-J), as well as western blotting assay validated little impact of *Tvrm222* variant on Müller glia cell number (Figure 12 K). Strikingly, GFAP staining was increased in *Nr2e3^{rd7/rd7}* mouse retinas relative to that found in wild type retinas (Figure 12 L, M), indicating activation of Müller glia cells. GFAP signal in *Tvrm222* mouse retinas was significantly repressed in comparison to that observed in *rd7* retinas (Figure 12 N). However, staining was still observable at the sites with residual retinal folds in *Tvrm222* mouse retinas (Figure 12 O). This strongly implies that Müller gliosis in *Tvrm222* mouse retinas is the consequence of the dysplastic lesion in the retina rather than the cause of *Tvrm222*-mediated suppression of *rd7*-associated photoreceptor dysplasia.

Taken together, our data demonstrate that modification of photoreceptor dysplasia by *Tvrm222* variant is not achieved via action on cell proliferation or Müller gliosis, but by alternative mechanisms.

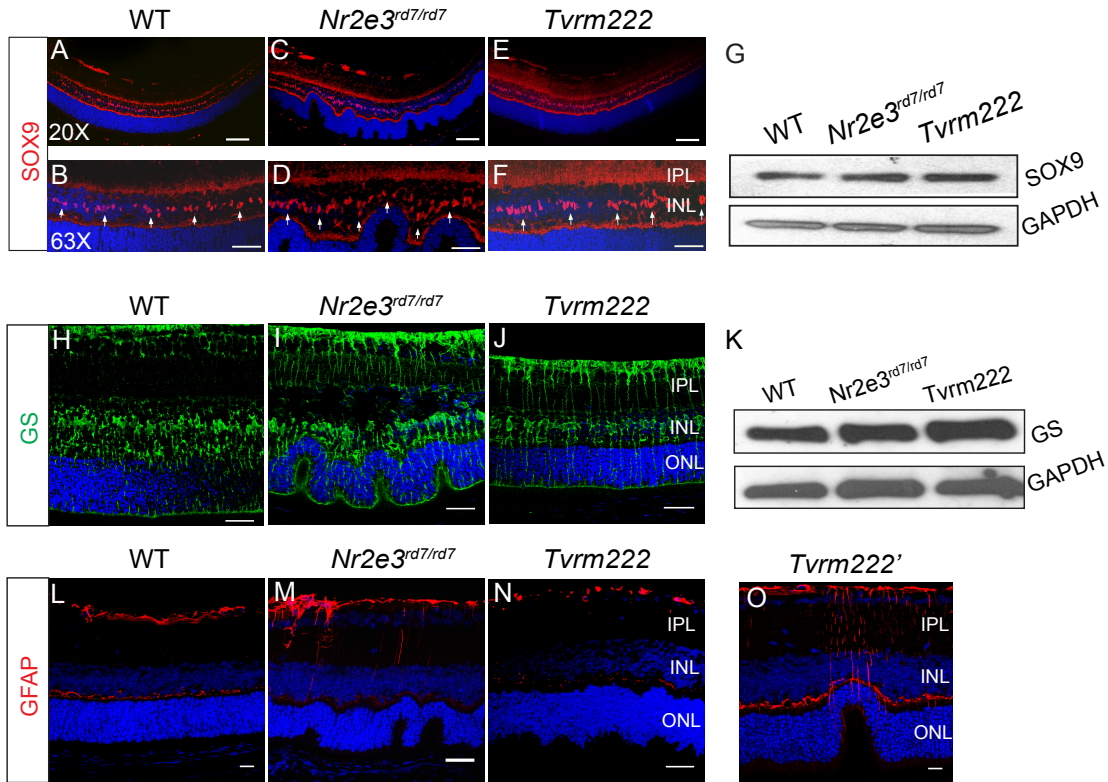


Figure 12. The impact of *Tvrn222* variant on Müller glia. Eye sections from two-week-old mice of WT, *Nr2e3^{rd7/rd7}* and *Tvrn222* were stained by antibodies against: (A-F) SRY Box (SOX) 9 for labeling somata of Müller glia. Note the localization of the Müller cells (arrows). Scale bar = 50µm (20×), 20µm (63×), (G) Representative western blot of SOX9 with GAPDH as the loading control; (H-J) Glutamine synthetase (GS), another Müller cell markers. Scale bar = 20µm. (K) Representative western blot of GS. GAPDH was used as the loading control. (L-O) Glial activation was assessed by staining of retinas with a glial fibrillary acidic protein (GFAP) antibody. Scale bar = 20µm. IPL: inner plexiform layer, INL: inner nuclear layer, ONL: outer nuclear layer.

3.2.2 Rescue of defective ELM by *Tvrm222* variant

Previous studies indicated that fragmentation of ELM is a prominent feature associated with photoreceptor dysplasia in mouse retinas, such as in *Nrl*^{-/-} and *Crb1*^{rd8/rd8} mice. In order to assess whether *Nr2e3*^{rd7/rd7} mice were similarly affected, we examined ELM integrity in *Nr2e3*^{rd7/rd7} and *Tvrm222* retinas by immunofluorescence staining, using antibodies against ZA junction molecules including CTNNB1 (β-catenin) and P-cadherin (CDH3), as well as the ZO junction molecule TJP1 (formerly ZO-1). In contrast to the compact and continuous ELM profile in wild type retinas, the ELM structure was diffused and fragmented in *Nr2e3*^{rd7/rd7} mouse retinas, indicating potential perturbation of cell-cell adhesion (Figure 13 B, E, I). Strikingly, the ELM in *Tvrm222* retinas remained largely intact (Figure 13 C, F, J), comparable to that observed in wild type mouse retinas (Figure 13 A, D, H).

We also examined the structure of the retina by light microscopy and transmission electron microscopy. Eye sections dissected from homozygous B6.Cg-*Nr2e3*^{rd7} at one month exhibited abundant dysplastic whorls. Unlike the distinct ELM structure that formed a visible linear profile in the wild type retina, the junctional plaques were largely missing in the *Nr2e3*^{rd7/rd7} mouse retinas (Figure 14 A, B). Higher magnification further revealed aberrant cellular organization at the level of photoreceptors with disordered IS and OS in the *Nr2e3*^{rd7/rd7} mouse retinas compared to their wild type counterparts, which was particularly striking at the sites of dysplastic whorls (Figure 14 D, E). In contrast, the ELM structure was distinguishable with normalization of IS/OS morphology in *Tvrm222* mouse retinas and an absence of dysplastic folds (Figure 14 C, F). Taken together, our data indicate that the disrupted junctional plaques at the level of ELM as well as anomalous photoreceptor morphology that are associated with *rd7* photoreceptor dysplasia are rescued in the presence of *Tvrm222* variant.

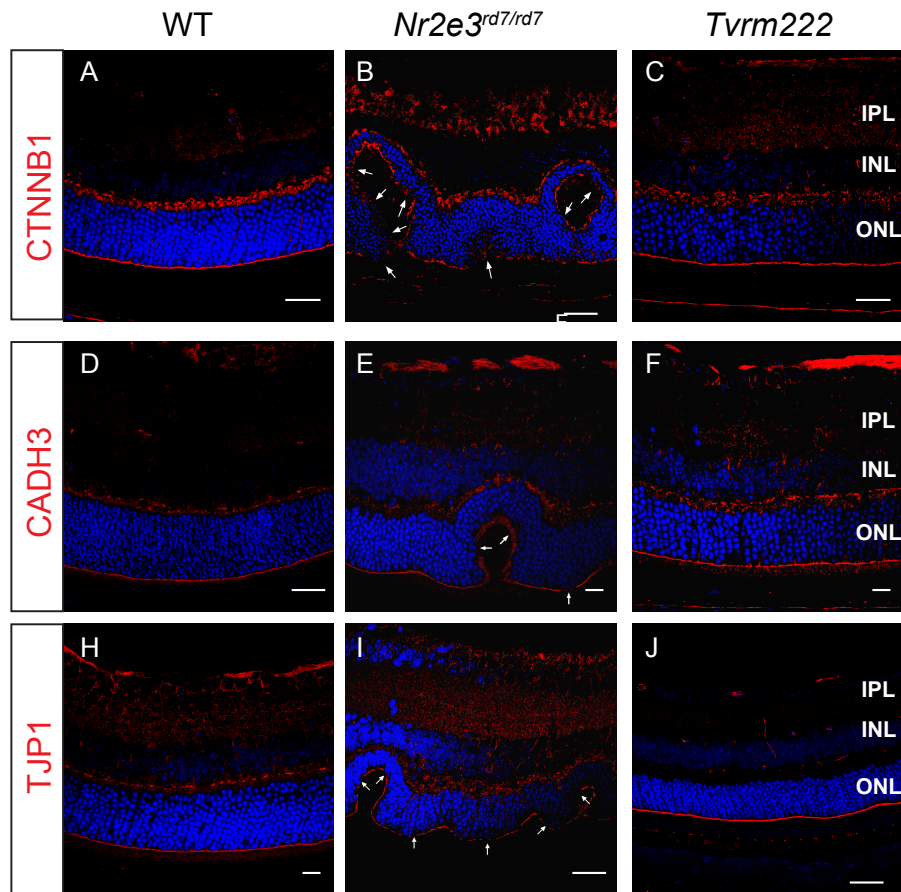


Figure 13. Prevention of ELM fragmentation associated with *rd7* dysplasia in *Tvrn222* retinas. Retina from one-month-old WT, *Nr2e3^{rd7/rd7}* and *Tvrn222* mice were subject to immunofluorescence staining using antibodies against CTNNB1 (b-catenin) (A-C), CDH3 (P-Cadherin) (D-F) and TJP1 (ZO-1) (G-I), respectively. The major breaks of ELM were indicated by arrows. Scale bar = 20 μ m. The fragmentation of the ELM is marked by arrows. IPL: inner plexiform layer; INL: inner nuclear layer; ONL: outer nuclear layer

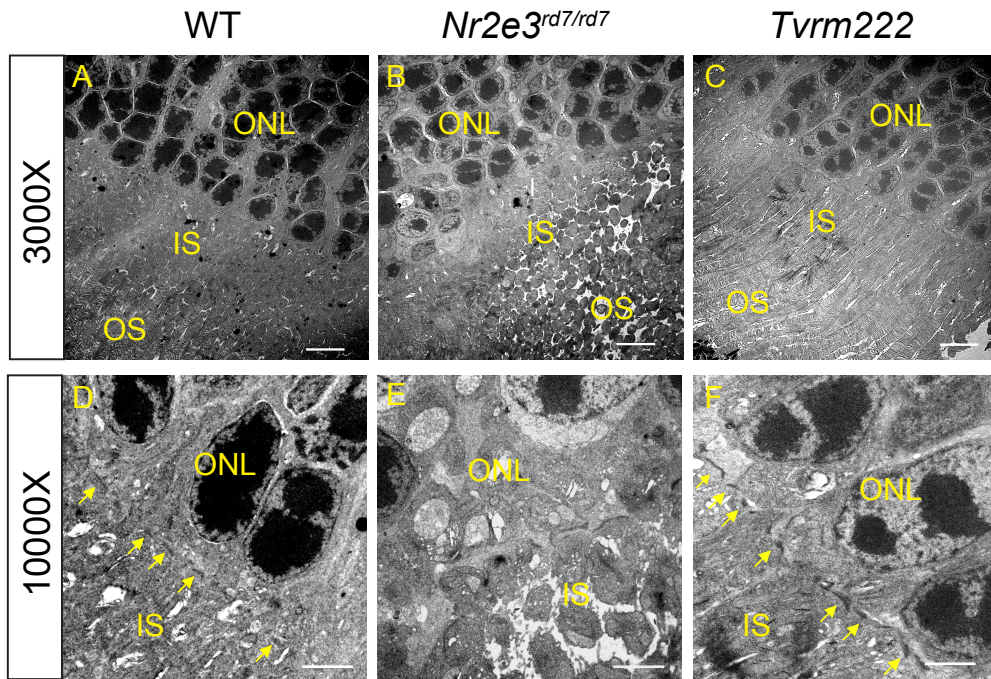


Figure 14. Maintenance of Retinal architecture in *Tvrn222* mice. Ultra-structure of the retina from one-month-old WT (A, D), *Nr2e3^{rd7/rd7}* (B, E) and *Tvrn222* (C, F) mice was examined by TEM. Retinal layers are labelled and ELM is marked by yellow arrows. IS and OS are distinctly shown in both WT and *Tvrn222* retinas. While the junctional plaques are largely missing and IS and OS are disarrayed in *rd7* retina. Scale bar = 5 μ m (3000 \times) or 2 μ m (10000 \times). IPL: inner plexiform layer, INL: inner nuclear layer, ONL: outer nuclear layer, IS: inner segment.

3.3 Identification of *Frmd4b*^{*Tvrm222*} variant as the genetic suppressor of photoreceptor dysplasia

3.3.1 Mapping *Frmd4b* variant as the modifier in *Tvrm222* mouse retina

In order to determine the molecular basis of the genetic rescue of *rd7* dysplasia by *Tvrm222*, we conducted genetic mapping and exome sequence analyses of *Tvrm222* mice. An initial map position was obtained by QTL analysis of a cohort of 51 animals from a backcross of (C57BL/6N × B6.Cg-*rd7/rd7*; *Tvrm222/Tvrm222*) F₁ × B6.Cg-*rd7/rd7*) that was phenotyped by indirect ophthalmoscopy. We first ruled out any significant epistatic loci or a major interference of sexual dimorphism with the *Tvrm222* modifying effect. A significant QTL was found on Chromosome 6 at 34.67 cM (LOD = 2.54, p (F) = 0.00086, Figure 15 A). The location on Chromosome 6 was confirmed in a second cross of (DBA/2J × B6.Cg-*rd7/rd7*; *Tvrm222/Tvrm222*) F₁ × B6.Cg-*rd7/rd7*), in which 21 animals homozygous for *rd7* were phenotyped. Marker *D6Mit29* (37.75 cM, LOD = 4.987) co-segregated with the suppressed phenotype and analysis of recombinants established a minimal region for *Tvrm222* between markers *D6Mit93* and *D6Mit287* spanning ~26 Mb. Whole exome sequencing of B6.Cg *rd7/rd7*; *Tvrm222/Tvrm222* DNA revealed four candidate missense variants, after filtering the sequencing results for novel and significant mutations, including *Dctn1*, *Frmd4b*, *Grcc10*, *Klra6* and *Trac1* within the region suggested by QTL mapping on Chromosome 6. Only a thymine to cytosine transversion in the *Frmd4b* gene co-segregated with *Tvrm222* modification (Figure 15 B). This variant is predicted to lead to a substitution of a serine residue 938 by proline (S938P). The FRMD4B^{S938P} variation is located in a threonine/serine rich domain near the carboxyl terminus of the protein. Cross-species alignment of mouse FRMD4B indicates that the residue corresponding to S938 is normally a proline (P938) in human and rat reference sequences (Figure 15 C).

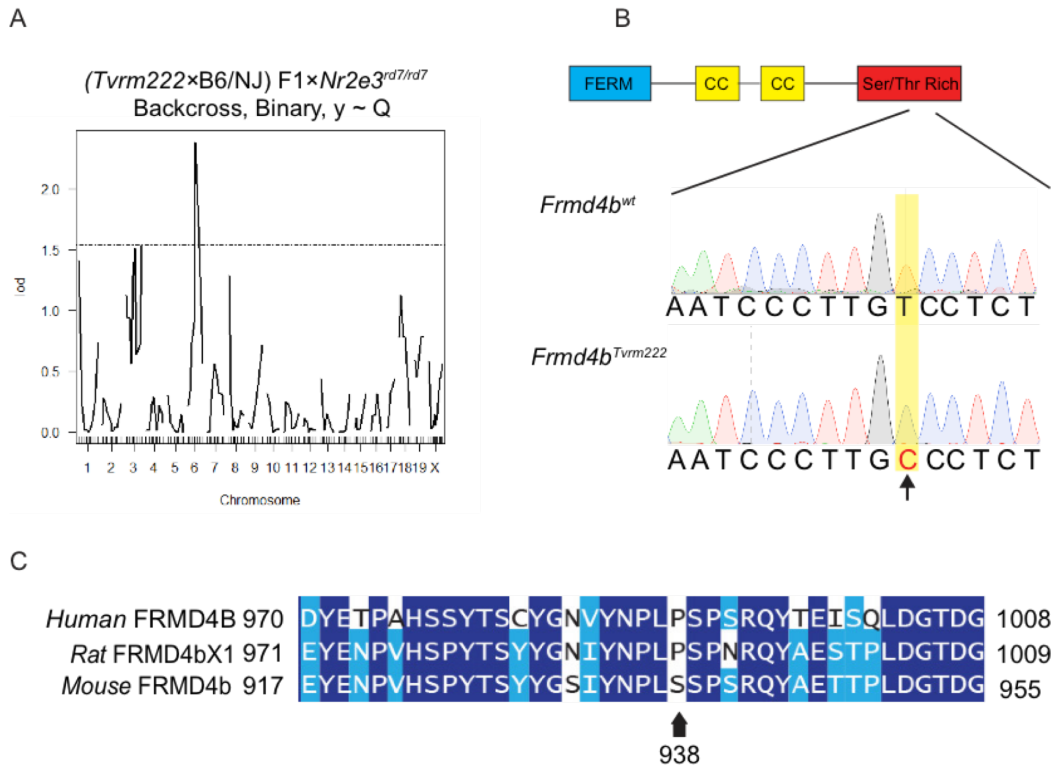


Figure 15. Whole genome mapping to identify the modifier allele in *Tvrm222* mice. (A)

Indicates cross and model used. 1000 permutations were used for each model to obtain a genome-wide LOD significance threshold. The dashed-dotted line indicates genome-wide significance thresholds $p < 0.63$. **(B)** Schematic representation of FRMD4B molecule and the predicted region of the mutation site. Sequencing traces around the *Tvrm222* variation in the *Frmd4b* gene. The arrow indicates the transversion of thymine to cytosine. **(C)** Alignment of human, rat and mouse FRMD4B sequences around the *Tvrm222* variation. Note the proline (marked by an arrow) in human and rat reference sequences is substituted by a serine in mice. The *Tvrm222* variation causes a substitution of the serine with proline. CC: Coiled-coil; FERM: 4.1 protein/Ezrin/Radixin/Moesin

3.3.2 Expression analysis of *Frmd4b*

Since a suitable FRMD4B antibody for western and immunohistochemical analysis was not available, *Frmd4b* expression was detected at the transcriptional level. PCR results showed that *Frmd4b*, amplified from cDNA libraries, is detectable across tissues and organs, including whole eye, retina RPE, brain, lung, and colon (Figure 16 A).

3.3.3 The *Frmd4b*^{*Tvrm222*} variant as the modifier for NRL deficiency

We also segregated the *Tvrm222* allele from the *rd7* mutation by outcrossing it to wild type B6/J mice in order to: 1. Examine the potential impact of the FRMD4B variant on retina in the absence of the *rd7* mutation; 2. Determine if the *Tvrm222* allele was able to reduce photoreceptor dysplasia in *Nrl*^{-/-} mice. The latter was achieved by crossing B6/J-*Frmd4b*^{*Tvrm222/Tvrm222*} mice with B6/J-*Nrl*^{-/-}, followed by an inter-crossing of the F₁ siblings to generate double homozygotes bearing both mutations, B6/J-*Nrl*^{-/-} *Frmd4b*^{*Tvrm222/Tvrm222*} mutants.

Histological examination showed normal retinal morphology in young and adult (two weeks and six months) mice bearing the homozygous *Frmd4b*^{*Tvrm222*} allele without *Nr2e3*^{*rd7/rd7*} (Figure 16 B-G). The photoreceptor dysplasia normally observed by indirect ophthalmoscopy and histology in *Nrl*^{-/-} mice was absent in adult (one month) *Nrl*^{-/-} mice in the presence of *Frmd4b*^{*Tvrm222*} allele (Figure 17 A-D), similar to that observed in *Tvrm222* mice. More importantly, the fragmented ELM associated with the photoreceptor dysplasia due to NRL deficiency was rescued in *Nrl*^{-/-} *Frmd4b*^{*Tvrm222/Tvrm222*} mouse retinas, indicated by both CTNNB1 and TJP1 staining. (Figure 18 A-D).

In conclusion, our mapping and sequencing data provides supportive evidence that the S938P variation of FRMD4B is the suppressor of the dysplastic phenotype in *Tvrm222*. *Frmd4b* is extensively expressed in multiple tissues and organs that we tested. The *Frmd4b*^{*Tvrm222*} allele is

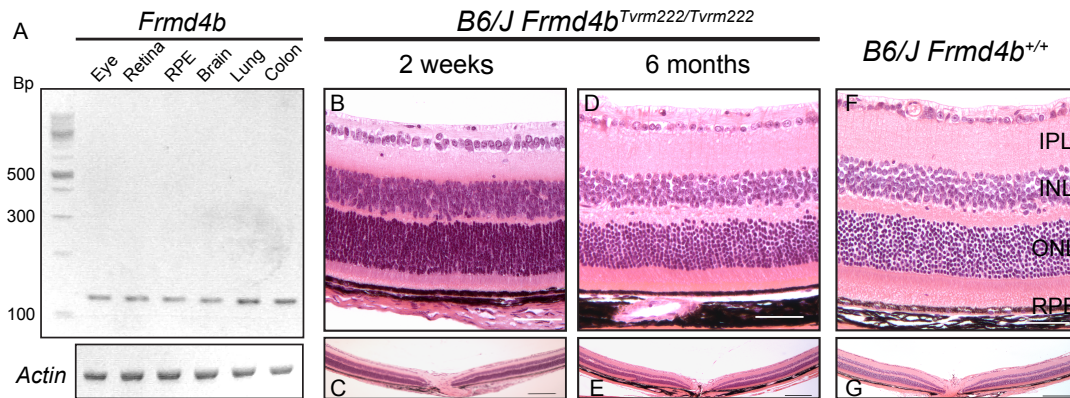


Figure 16. Expression profile of the *Frmd4b* transcript and the impact of the *Frmd4b*^{Tvrn222} allele on mouse retina. (A) RT-PCR of actin (as an internal control) and *Frmd4b* from RNA prepared from whole eye, retina, RPE, lung, brain and colon using primers specifically amplify *Frmd4b* transcript from the cDNA templates. Actin as the internal control. Histological sections show no evident retinal folds at two weeks of age (B, C) and at a later time point (six months, D, E) in eyes from mice carrying the homozygous *Frmd4b*^{Tvrn222} allele only (Scale bar: 20× 50μm; 5× 200μm). IPL: inner plexiform layer, INL: inner nuclear layer, ONL: outer nuclear layer, RPE: retinal pigment epithelium.

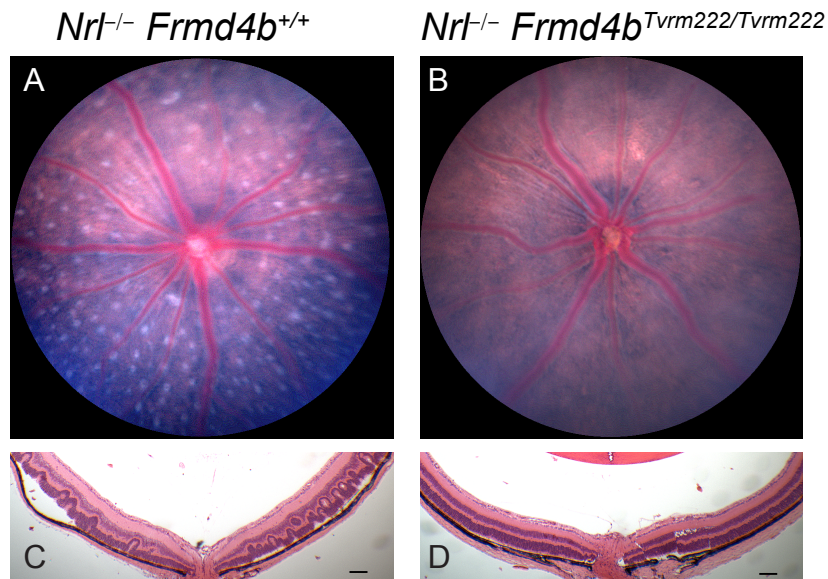


Figure 17. Suppression of retinal dysplasia due to NRL deficiency in the presence of *Frmd4b*^{*Tvrn222/Tvrn222*}. (A, B) The fundus images of one-month-old *Nrl*^{-/-} and *Nrl*^{-/-} *Frmd4b*^{*Tvrn222/Tvrn222*} mice. Note that the *Nrl*^{-/-} retina displays the typical spotting phenotype while the *Nrl*^{-/-} *Frmd4b*^{*Tvrn222/Tvrn222*} retinas show significant reduction in the number of spots. (C, D) H&E stained retina sections from *Nrl*^{-/-} and *Nrl*^{-/-} *Frmd4b*^{*Tvrn222/Tvrn222*} mice indicated the suppression of dysplastic lesions in *Nrl*^{-/-} mice harboring the *Frmd4b*^{*Tvrn222*} allele. Scale bar = 100μm.

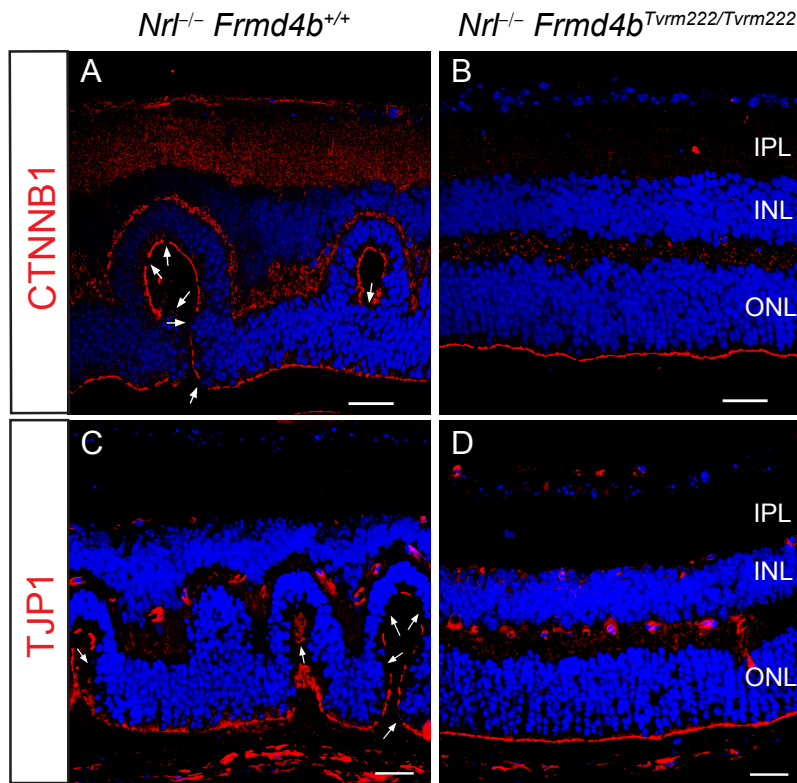


Figure 18. Maintenance of ELM integrity in *Nrt*^{-/-} mice in the presence of the *Frmd4b*^{Tvrn222/Tvrn222} allele. *Nrt*^{-/-} retinal sections from one-month-old animals were immunostained with both anti-CTNNB1 (A, B) and anti-TJP1 (C, D) to assess ELM fragmentation. The breaks in the ELM are indicated by arrows. Such breaks were rarely observed in *Nrt*^{-/-} *Frmd4b*^{Tvrn222/Tvrn222} retinas (B, D). Scale bar = 20 μ m. IPL: inner plexiform layer, INL: inner nuclear layer, ONL: outer nuclear layer.

shown to rescue dysplastic lesions in both *Nr2e3*^{rd7/rd7} and *Nrl*^{-/-} mouse retinas. Therefore, it is vital to determine the molecular and cellular mechanisms that underlie the modification of photoreceptor dysplasia by the FRMD4B variant.

3.4 Reduced cell surface recruitment of FRMD4B in the presence of 938P

The *Frmd4b*^{Tvrm222} variant is predicted to carry an altered amino acid, 938P, in the FRMD4B protein in mouse. Given that cell surface targeting is one of the most prominent features identified thus far for the CYTH3-FRMD4B complex, we compared the intracellular localization of wild type and the FRMD4B^{938P} in cultured cells in order to explore the mechanism by which the *Frmd4b*^{Tvrm222} variant suppresses the dysplastic lesions in retina. To test the effect of the S938P variation on the localization of the CYTH3-FRMD4B complex, COS-7 cells were transiently co-transfected with vectors expressing epitope-tagged CYTH3 and either wild type FRMD4B or the FRMD4B^{938P} variant. The cells were then subjected to serum starvation before insulin supplementation. Without insulin treatment, both the wild type and the FRMD4B^{938P} variant were shown to be diffusely localized in the peri-nuclear region within the cytoplasm (Figure 19 A-D). After insulin supplementation of the culture media, wild type FRMD4B (Figure 20 A, B) was translocated to the cell surface and co-localized with sub-cortical actin fibers, stained by phalloidin, consistent with previous findings. In contrast, a large proportion of the FRMD4B^{938P} variant remained cytosolic even with insulin treatment (Figure 20 C, D). To confirm this result, we also performed subcellular fractionation using protein extracts from HEK-293T cells that were transiently co-transfected with vectors expressing epitope-tagged CYTH3 and either wild type FRMD4B or the FRMD4B^{938P} variant. Similarly, cell surface targeting between the wild type FRMD4B and the FRMD4B^{938P} variant was similar in the absence of insulin (Figure 19 E). However, after supplementing with insulin, more wild type FRMD4B was partitioned to

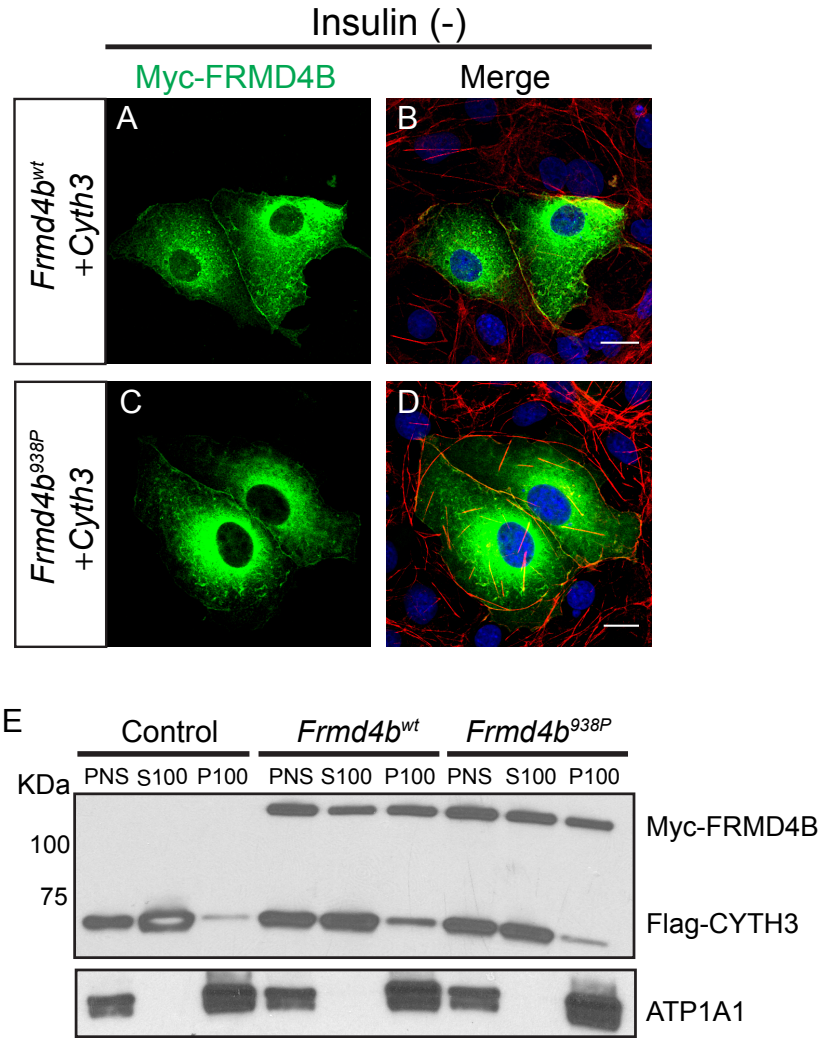


Figure 19. *In-vitro* cytosolic localization of FRMD4B without stimulation of insulin. (A-D) COS7 cells were co-transfected with 3×FLAG-CYTH3 and either 3×myc-FRMD4B^{wt} (A, B) or 3×myc-FRMD4B^{938P} (C, D), and subject to serum starvation (without insulin). 3×myc-FRMD4B was detected by immunofluorescence using an antibody against the myc tag (green). Counterstaining with phalloidin (red) shows sub-plasma membrane actin cytoskeleton and DAPI for nuclei. Scale bar = 20µm. **(E)** Subcellular fractionation profiles of HEK-293T cells transiently transfected with 3×FLAG-CYTH3 and either 3×myc-FRMD4B^{wt} or 3×myc-FRMD4B^{938P}, and without treatment insulin after serum starvation. Na⁺/K⁺-ATPase (ATP1A1) was used as the loading control for membrane fractions. PNS: post-nuclear supernatant; S100: supernatant after 100,000 × g centrifugation; P100: pellet after 100,000 × g centrifugation

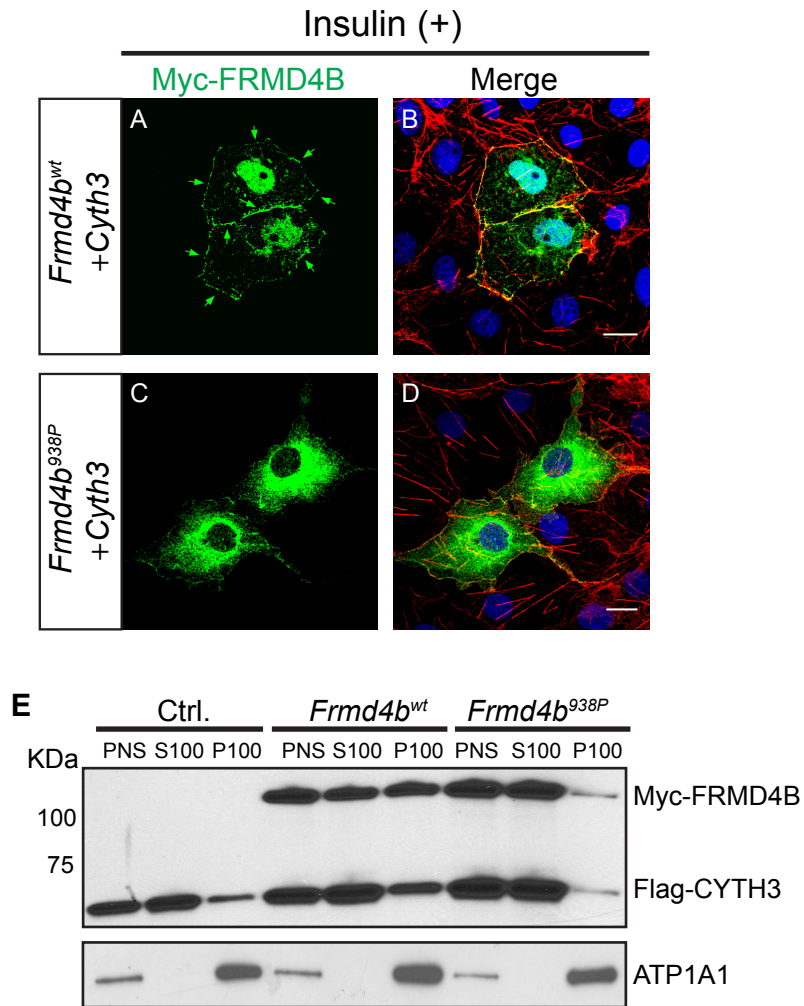


Figure 20. Decreased membrane recruitment of FRMD4B^{938P} with insulin stimulation *in vitro*. (A-D) COS7 cells were co-transfected with 3×FLAG-CYTH3 and either 3×myc-FRMD4B^{wt} (A, B) or 3×myc-FRMD4B^{938P} (C, D), and subject to serum starvation followed by treatment of 100 nM insulin. 3×myc-FRMD4B was detected by immunofluorescence using an antibody against the myc tag (green). Counterstaining with phalloidin (red) shows sub-plasma membrane actin cytoskeleton. Note the cell-surface targeted FRMD4B (arrows). Scale bar = 20µm. (E) Subcellular fractionation profiles of HEK-293T cells transiently transfected with 3×FLAG-CYTH3 and either 3×myc-FRMD4B^{wt} or 3×myc-FRMD4B^{938P}, and treated with insulin after serum starvation. Na⁺/K⁺-ATPase (ATP1A1) was used as the loading control for membrane fractions. PNS: post-nuclear supernatant; S100: supernatant after 100,000 × g centrifugation; P100: pellet after 100,000 × g centrifugation

the membrane fraction compared to FRMD4B^{938P} (Figure 20 E), consistent with the immunofluorescence results.

To further confirm the reduced efficiency of cell surface targeting for the FRMD4B^{938P} variant protein, we assessed FRMD4B membrane localization in mouse tissue. A primary antibody against FRMD4B was provided to us as a generous gift from Dr. Czech. This antibody was able to detect a protein band of the expected size in western blots of lung tissue extracts, but not retinal tissue. We found that the C57BL/6L mouse, harboring the *Frmd4b*^{Tyrm222} allele showed reduced membrane-association of the FRMD4B protein in lung tissue compared with the FRMD4B localization in wild type C57BL/6J mice (Figure 21 A).

Since FRMD4B has been shown to bind CYTH3, we additionally tested whether membrane recruitment of FRMD4B after insulin stimulation is dependent on CYTH3 and is affected by the 938P variant. We found that, in the absence of CYTH3, both the exogenous wild type FRMD4B and the FRMD4B^{938P} variant were present morphologically different from those that were co-existed with CYTH4. Additionally, the transfected FRMD4B was predominantly aggregated in the cytoplasm upon insulin stimulation (Figure 21 B-E), indicating the dependence of membrane recruitment of FRMD4B on CYTH3, which is consistent with previous observations. Next, we sought to determine if the FRMD4B^{938P} variant protein, compared to wild type FRMD4B, had a lower binding affinity for CYTH3, which in turn is responsible for the reduced membrane recruitment of FRMD4B^{938P}. Using a co-immunoprecipitation approach, epitope-tagged CYTH3 and FRMD4B were expressed in HEK-293T cells. An epitope tagged endoplasmic reticulum lumen protein heat shock protein 90 β family member 1 (HSP90B1) was used in place of CYTH3 in one sample, as a negative control to exclude potential non-specific binding of CYTH3 to FRMD4B. We found that the binding affinity between FRMD4B and

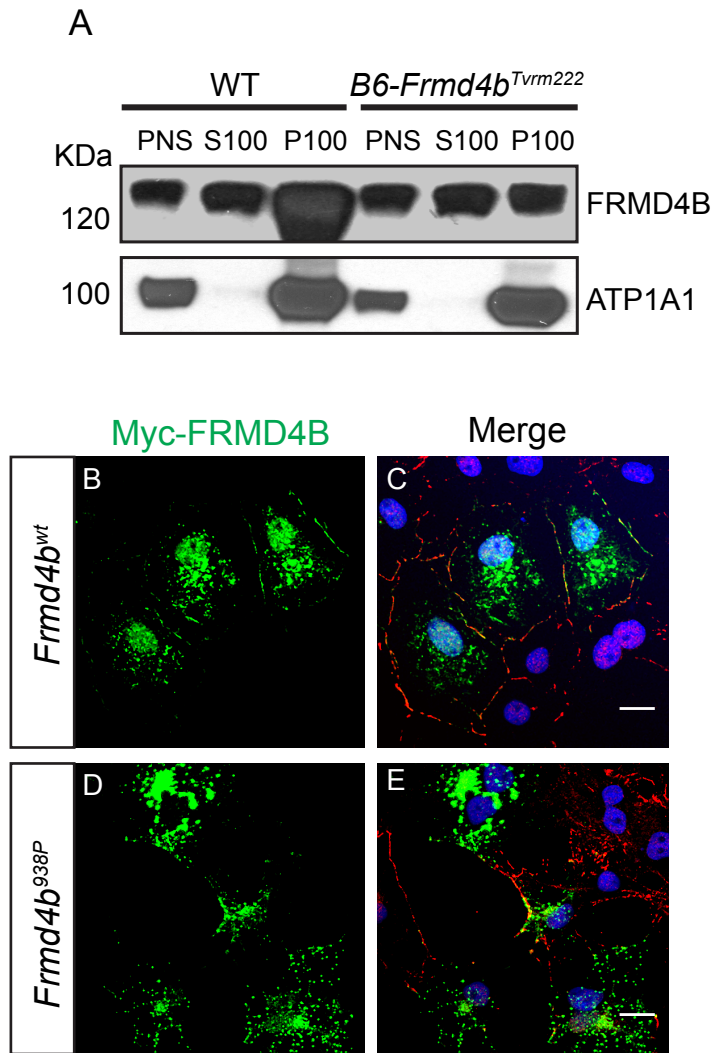


Figure 21. Dependence of FRMD4B on CYTH3 for cell-surface targeting. (A) Membrane fractionation profile of proteins extracted from mouse lung. Endogenous FRMD4B was detected by an FRMD4B antibody (From Dr, Michael Czech). Na^+/K^+ -ATPase (ATP1A1) was used as the loading control for membrane fractions. (B-E) COS7 cells transfected with only 3×myc-FRMD4B^{WT} (B, C) or 3×myc-FRMD4B^{938P} (D, E), but without 3×FLAG-CYTH3 were subject to immunofluorescence staining. Note FRMD4B tends to aggregate in the cytoplasm without co-transfection of CYTH3.

CYTH3 remained unaffected by the FRMD4B^{938P} variant irrespective of insulin stimulation (Figure 22 A, B). It suggests that the FRMD4B^{938P} variant does not affect its' physical interaction with CYTH3. Thus, the reduction in membrane recruitment of FRMD4B^{938P} was not due to an alteration in binding affinity between CYTH3 and FRMD4B. In addition, we also tested whether a physical interaction existed between the CYTH3-FRMD4B complex and CTNNB1 or TJP1, two major intracellular components of cell junctions with binding capacity for proteins involved in intracellular signaling cascades. No evident physical interaction was observed between the CYTH3-FRMD4B complex and either cell junctional component (Figure 22 C). Therefore, this implies that an alternative pathway(s) through which the CYTH3-FRMD4B complex affects cell-cell contact may account for the ELM phenotypes.

3.5 Alterations of ARF6 and AKT pathways in the presence of S938P variation

3.5.1 Elevation of ARF6 activation associated with the FRMD4B^{938P} variant

Since the wild type FRMD4B and the FRMD4B^{938P} variant are differentially recruited to the cell surface, we probed downstream processes that could potentially influence cell junctions and contribute to the maintenance of ELM integrity. It has previously been reported that FRMD4B and its paralogue, FRMD4A, in complex with cytohesins, play a key role in cell junction remodeling by linking ARF6 to the PAR3-PAR6-aPKC complex at the cell surface (116). Based on our finding that the FRMD4B^{938P} variant was less efficiently recruited to the cell surface upon insulin stimulation, we proposed that the FRMD4B^{938P} variant might affect ARF6 activity. To test this hypothesis, we measured the ratio of the ARF6 GTP-binding form to the total amount of ARF6, as an indicator of its activation. Protein extracted from HEK-293T cells transfected with CYTH3 and either wild type FRMD4B or the FRMD4B^{938P} variant were

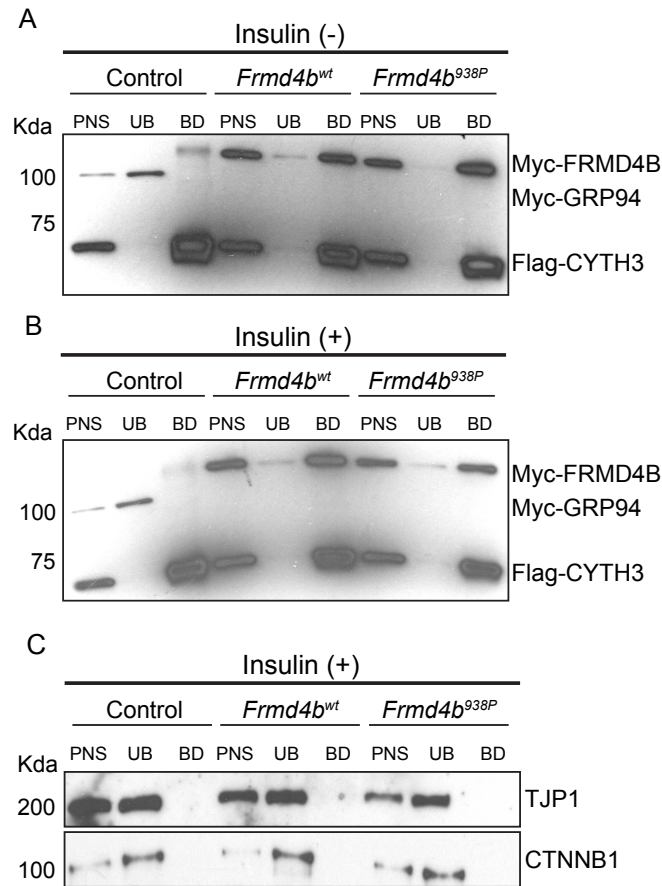


Figure 22. Unaltered binding between CYTH3 and FRMD4B in the presence of 938P variant and no physical interaction with junctional components. (A, B) Co-immunoprecipitation of CYTH3 and FRMD4B from protein extracts prepared from HEK-293T cells. Cells were transfected with 3×FLAG-CYTH3 and myc-tagged HSP90B1 (GRP94) as a negative control (for non-specific MYC interactions), and 3×myc-FRMD4B^{wt} or 3×myc-FRMD4B^{938P}. Cells were either untreated (A) or treated (B) with 100 nM insulin after starvation. Co-immunoprecipitation was performed on post-nuclear supernatant (PNS) using anti-FLAG M2 antibody conjugated agarose beads. UB: unbound; BD: bound. (C) Immunoprecipitates (described above) were also probed for CTNNB1 and TJP1 to test for a potential physical interaction between the CYTH3-FRMD4B complex the cell junction components.

incubated with GGA3 PBD conjugated to agarose beads. The GGA3 PBD specifically recognizes the ARF6 GTP-binding form but not the GDP-binding form. GTP-bound ARF6 and total ARF6 were resolved by western blot analysis. The results showed that the ratio of GTP-bound ARF6 was increased in the presence of the FRMD4B^{938P} variant (Figure 23 A, C). We observed similar results in retinal protein extracts (Figure 23 B). Thus, both *in vitro* and *in vivo* data indicate that the FRMD4B^{938P} variant leads to an increased ARF6 activation compared to wild type FRMD4B.

3.5.2 Decreased AKT phosphorylation associated with *Frmd4b*^{Tvrm222} variant

We also examined whether AKT activity was similarly affected, given the close relationship between CYTH3 and the PI3K-AKT signaling pathway (173), and the effects of insulin stimulation on the localization of the *Frmd4b*^{Tvrm222} variant. Protein was extracted from eyecups dissected from wild type, *Nr2e3*^{rd7/rd7} and *Tvrm222* mice and subject to SDS-PAGE analysis. The results showed that phosphorylated AKT (Ser473) was significantly reduced in *Tvrm222* mouse eyes compared to the other two groups (Figure 24 A, B), suggesting a suppression in AKT activation in the presence of *Frmd4b*^{Tvrm222} variant.

3.5.3 Increased membrane-associated junctional components in *Tvrm222* retinas.

To assess the basis for the rescue of the ELM fragmentation in *Tvrm222* mutants, we determined whether cell junction components were affected compared to either wild type or *Nr2e3*^{rd7/rd7} retinas as observed by immunofluorescence staining and by TEM examination. Subcellular fractionation assays revealed that both CTNNB1 (Figure 25 A, B) and TJP1 (Figure 26 A, B) were significantly increased in the membrane fraction of *Tvrm222* mouse retinas, compared with that in both wild type and *Nr2e3*^{rd7/rd7} retinas. Stabilization of cell-cell contact is consistent with our observations that the ELM integrity is preserved in *Tvrm222* mouse retinas.

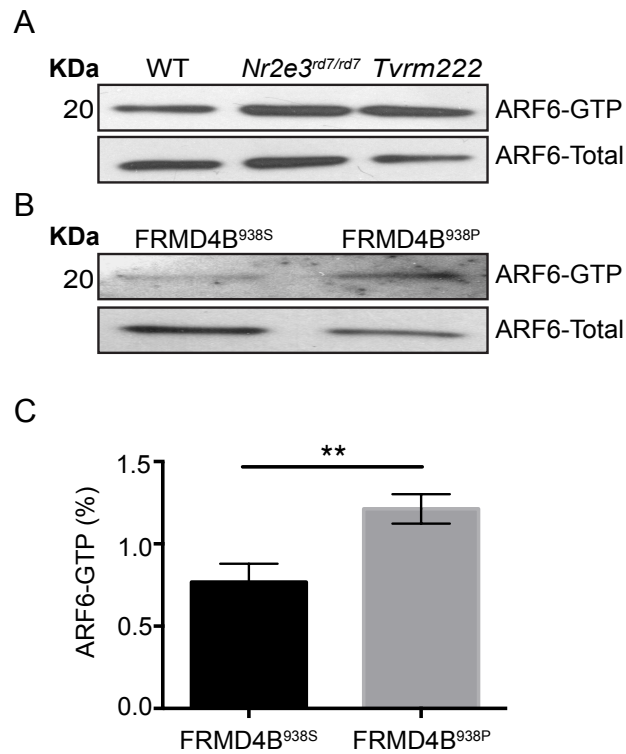


Figure 23. Increased level of GTP-binding form of ARF6 in presence of the FRMD4B^{938P} variant. The levels of GTP-binding ARF6 co-transfected with 3×FLAG-CYTH3 and 3×myc-FRMD4B^{wt} or 3×myc-FRMD4B^{938P} in HEK-293T cells (A) and in retinal tissue (B), were assayed by pull-down using the ARF6-binding domain from GGA3 (crosslinked to agarose beads). The results from transfected cells were quantified and analyzed by one-way ANOVA and post-hoc Tukey's test (C). The results are mean ± S.D., n=3 for each group, ** p<0.01.

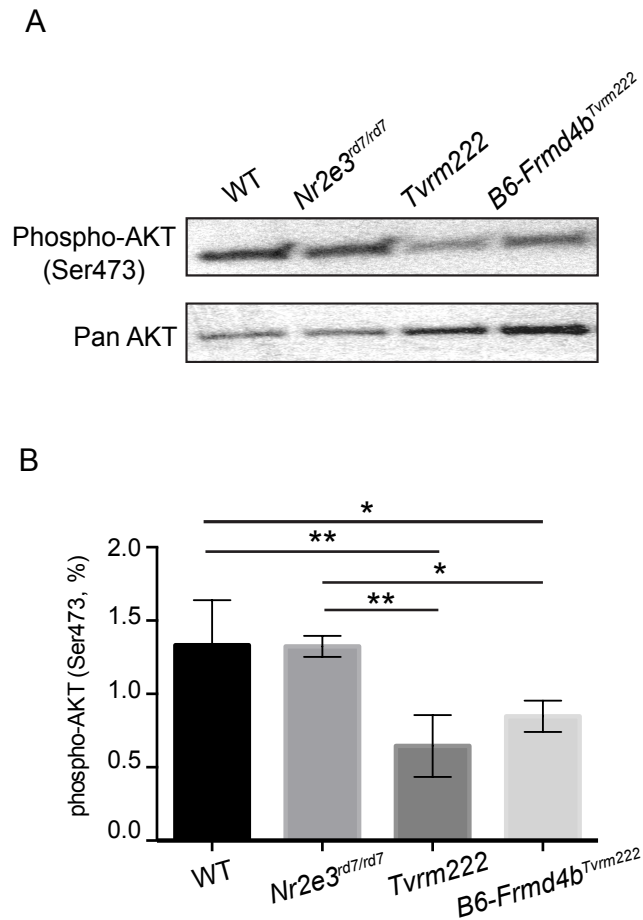


Figure 24. Decreased phosphorylation of AKT in *Tvrn222* mouse eyes. Protein extract from mouse eyecups were analyzed for AKT phosphorylation by western blot analysis. Phosphorylated AKT was probed with an antibody against phosphorylated AKT (Ser473). AKT phosphorylation was significantly downregulated in mice homozygous for *Frmd4b*^{Tvrn222} allele, compared to both WT and *Nr2e3*^{rd7/rd7} mice. Pan-AKT was used as the loading control (A). The western blotting results were quantitated as mean \pm S.D., n = 5 for WT, *Nr2e3*^{rd7/rd7} and *Tvrn222*; n=4 for *Frmd4b*^{Tvrn222}. (B); *: p< 0.01, **: p<0.001 (one-way ANOVA, post-hoc Tukey's test).

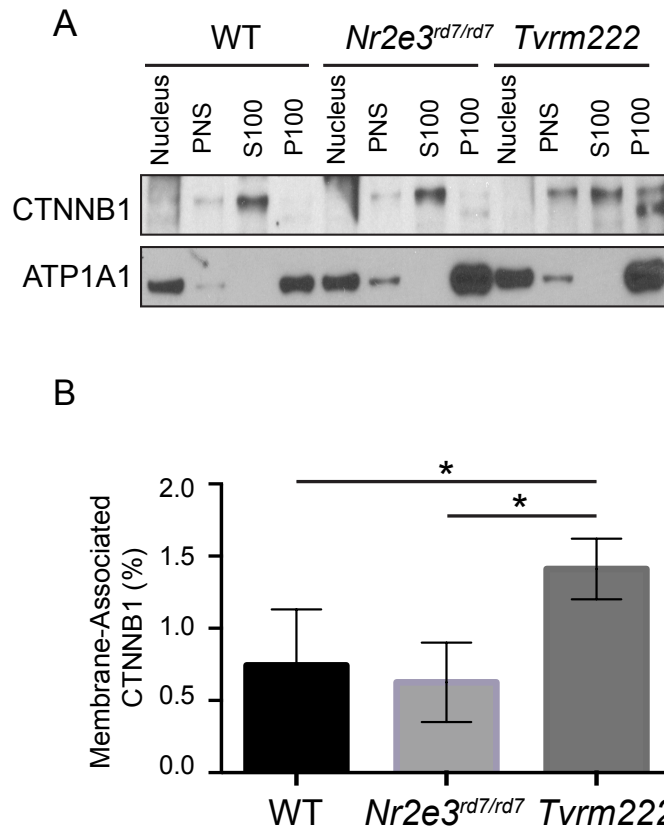


Figure 25. An increase in membrane-associated CTNNB1 in *Tvrm222* mouse retinas.

Crude membrane fractionation of mouse eyecups and subsequent western blot analysis of each fraction using an antibody against CTNNB1 (A). ATP1A1 was used as the loading control for membrane fractions. Note there is a statistically significant increase in membrane-association (P100) of CTNNB1 in *Tvrm222* mouse retinas relative to those in both WT and *Nr2e3^{rd7/rd7}* mice. (B). The levels of membrane-associated CTNNB1 was normalized to corresponding ATP1A1 levels and was quantified by ImageJ. Results from four independent experiments were used in the quantification. Statistical analysis was performed by one-way ANOVA with Tukey's test for multiple comparisons. The results are mean \pm S.D., *: $P < 0.05$, **: $P < 0.01$.

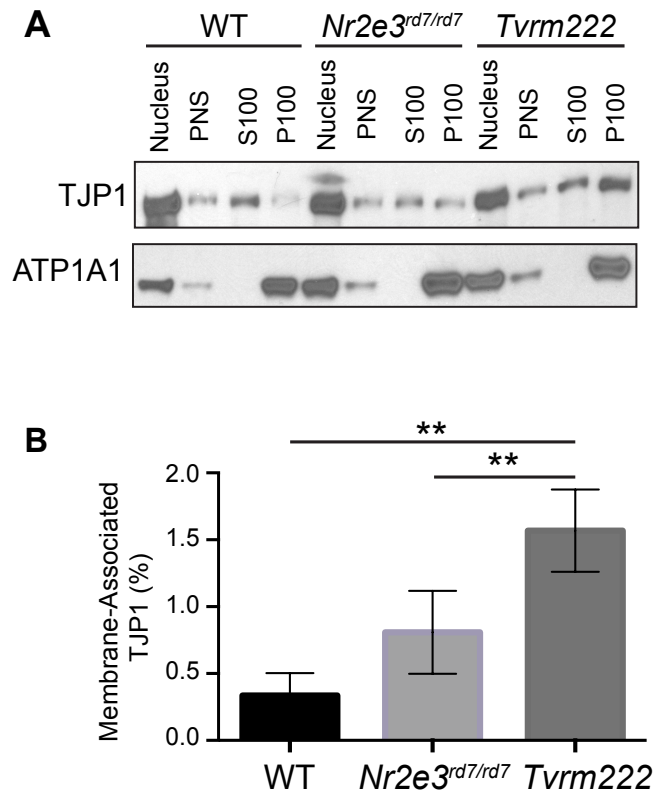


Figure 26. An increase in membrane-associated TJP1 in *Tvrn222* mouse retinas.

Crude membrane fractionation of mouse eyecups and subsequent western blot analysis of each fraction using the antibody against TJP1 (A). ATP1A1 was used as the loading control for membrane fractions. Note there is a statistically significant increase in membrane-association (P100) of TJP1 in *Tvrn222* mouse retinas relative to those in both WT and *Nr2e3^{rd7/rd7}* mice. (B). The levels of membrane-associated TJP1 was normalized to corresponding ATP1A1 levels and was quantified by ImageJ. Results from four independent experiments were used in the quantification. Statistical analysis was performed by one-way ANOVA with post-hoc Tukey's test for multiple comparisons. The results are mean \pm S.D., *: $P < 0.05$, **: $P < 0.01$.

CHAPTER 4

DISCUSSION

4.1 Characterization of *Tvrm222* modification of photoreceptor dysplasia

4.1.1 Recapitulation of morphological defects of ESCS patients in mice

Mutations in *NR2E3* were first reported in patients with ESCS. In clinics, apart from congenital stationary night blindness, impaired visual acuity, and hyperactive S-cone ERGs, distortion of retinal laminar architecture has also been reported (174, 175). The structural retinal abnormality in human ESCS patients displays unique features such as coarse lamination with thickened and bulging appearance. The *en face* view of *NR2E3*-mutant patients' retinas exhibit an annular increase in retinal thickness at the eccentricity of the optic nerve, that normally declines as the distance from the fovea increases (176). The retinal laminar defects in human patients correspond to disease severity. At early stages, some of the retinal layers are slightly thicker than normal. As the disease progresses, the normal laminar pattern of the retina is lost and visual function and acuity are impaired (176). Based on clinical observations, it is likely that the distinctive regional reflectivity by fundus examination is due to retinal undulation, which gives rise to the pan retinal spotting phenotype. In mice, where invasive assessment of the retina can be done, the undulation of the photoreceptor layer is found to correspond to the spotting phenotype. Our observations and clinical reports, taken together, suggest that the defective retinal lamination is a prominent characteristic of *NR2E3*-induced dysplastic changes found in both humans and rodents alike, and also hint an approach for remedying the observed laminopathy, namely suppression of photoreceptor dysplasia.

4.1.2 Functional assessment of *Tvrm222* modification in mice

In addition to the morphologic alterations, the modifying effect of the *Tvrm222* allele on photoreceptor functionality, which is impaired since early childhood in human patients with disruptions in *NR2E3*, was assessed. Surprisingly, a significant functional rescue, as assessed by ERG, did not accompany the anatomic modification of dysplastic lesions in *Tvrm222* retinas. We postulate that the *Tvrm222* modification does not directly resolve the disruption in cone photoreceptors that occurs as a result of the *Nr2e3^{rd7}* mutation. The increase in blue cones and gradual loss of photoreceptors with age was considered the major contributor to impaired retinal function in *Nr2e3^{rd7/rd7}* mutants (100). In this study, we showed that *Frmd4b^{Tvrm222}* correction of retinal lamination was mainly associated with stabilization of cell adhesions at the ELM and thereby, correction of the structural abnormalities. However, *Tvrm222* modifier lacked the ability to revert abnormal cone cell development and to prevent the loss of photoreceptors with age.

It is also worth noting that, unlike human patients with an *NR2E3* mutation, the ERG profiles of *Nr2e3^{rd7/rd7}* mice show little enhancement of the S cone response while rod responses are still comparable to wild-type controls at a young age (177, 178). Additionally, unlike their human counterparts, visual acuity in *Nr2e3^{rd7/rd7}* mice is comparable to B6 controls at 1.5 months of age, according to our preliminary observations. These phenotypic differences in disease manifestation may be due to genetic background influences or alternatively, to allelic variation (e.g. not a null mutation).

Furthermore, it is reasonable to speculate that species differences in photoreceptor development, composition and localization account for the functional differences between humans and mice bearing disruptions in *NR2E3*. Usually, the formation of cone photoreceptors takes place earlier than the genesis of rods, which becomes more evident in the mammals with

longer gestation (31). More importantly, rodents are nocturnal and rely less on cone photoreceptors, while most human activities are performed in light and require the cone photoreceptors that are found in highest density in the macula. The variation of photoreceptor growth and development, as well as of function in the context of *Nr2e3/NR2E3* mutations across species deserves further investigations to allow for better translation and interpretation of data.

4.2 Identification of the *Tvrm222* mutation as the suppressor for photoreceptor dysplasia

4.2.1 Mapping and sequencing the *Tvrm222* genetic modifier(s)

In this study, whole genome mapping was applied in order to reveal the QTLs that accounted for the *Tvrm222* modification. QTL mapping has undergone significant improvements since its advent as a large number of polymorphic markers are available and efficient genotyping technologies and statistical methods have been developed (179, 180). Nevertheless, dissecting the molecular basis of quantitative traits still faces challenges, including the reproducibility and robustness of phenotypes involved, other environmental or genetic factors that might confound genotype-phenotype associations, and availability of cohorts that have sufficient power to detect and localize QTLs (181).

Selection of an appropriate statistical model that links trait values to QTL genotype for mapping is extremely important. The nature of the phenotypic trait as well as the involvement of non-inherited elements largely determine selection of models for QTL mapping (182). In our study, the reduced photoreceptor spotting phenotype in *Tvrm222* mice was examined as a binary trait. However, the suppressive effect of *Tvrm222* is variable, ranging from complete absence of spots to a moderate level of suppression. Therefore, an ordinal trait analysis was also employed, which scored the suppressive effect in ordered categories according to the magnitude of the pan retinal spotting phenotype. The threshold model, in theory, assumes that liability is continuous.

When it reaches the LOD significance threshold, the categorical phenotype is observed (183). Thus, compared to the binary trait that is related to discrete liability, ordinal traits can be related to a continuous liability and the data can be analyzed by methods for continuous traits as long as the number of categories for an ordinal trait is large enough, hence reducing the loss of information during translation from an underlying liability to observable phenotypes (184). It should be noted, however, that although ordinal traits may capture a QTL with a greater sensitivity, an ordinal trait value for an individual is more vulnerable to measurement error than binary traits (179). Plus, QTL mapping analysis for both binary and ordinal traits are usually less powerful than mapping methods for continuous traits. This study, for instance, analyzed the *Tvrm222* phenotypes as both binary and ordinal traits. The binary trait delineated *Tvrm222* modification more distinctly and precisely by using the animals with only complete suppression in comparison to those mice with *rd7*-like dysplasia. Binary calls, however, were likely to miss those with partial modification whereas with characterization using ordinal calls, different degrees of *Tvrm222* modification could be considered. However, such characterization is more subject to phenotyping errors as the boundary to distinguish the *Tvrm222* modification of different extents could be ambiguous. In this study, however, both types of analyses reached the same conclusion. Since the suppressive phenotype in *Tvrm222* mice is primarily caused by induced allelic variant(s) instead of multifactorial inheritance, the categorical model, as a discrete trait for QTL mapping was used in the final analysis.

In order to localize a QTL, occurrence of recombination in the vicinity of the QTL is necessary. Precise QTL mapping is determined in part by the number of animals used in the mapping cohort, a better mapping resolution is expected with larger number of animals (185). In addition, appropriate marker density is necessary to define the areas of recombination. It is

evident that enormous number of mapping individuals would be needed to detect and to localize QTLs to small chromosomal regions (186). This explains why QTL mapping is usually iteratively performed, that is, one first determines an approximate location of 10-20 cM interval by testing a limited number of individual animals, and continuously reducing the potential QTL-associated regions by focusing on individuals with occurrence of recombination between markers that flank the QTLs, and by repeating the mapping procedure in even smaller genomic regions (187). This approach was employed in this study, where an independent cohort of animals was examined by linkage analysis using MIT markers in those regions harboring suggestive and potential QTLs (The candidate modifier was mapped to Chromosome 6, 37.75 cM in *mus musculus* according to the QTL report). We were able to confirm the Chromosome 6 linkage and exclude some of the suggestive loci on other chromosomes.

Admittedly, mapping and sequencing are the statistics-based methods for identifying randomly induced allelic mutations in animals. Direct generation of targeted mutations in candidate gene(s) serves as one of the most compelling approaches to demonstrate the causality between allelic variants and phenotypic alterations. For instance, application of transcription activation-like effector nucleases-mediated gene targeting approach provides a highly efficient way to induce mutations at specific genomic loci *in vivo* (188). Additionally, the advent of genome-editing tool CRISPR-Cas9 with oligonucleotide directed repair remarkably facilitates targeted manipulation of given genes in the animals (189). These genetic modification tools serve to validate the identified modifier variant(s). While considering the costs associated with these methods and the strong biochemical validation observed, these studies were not included.

4.2.2 Genetic suppressor for *rd7* photoreceptor dysplasia

This study focused on a mouse model carrying a modifier allele that was consistent with Mendelian laws of inheritance. The mode of Mendelian inheritance falls into the following major categories: autosomal dominant/recessive inheritance, sex-linked inheritance and mitochondrial inheritance (190). In this study, continuous selection of affected male mice as the founder strain for crossing purposes excludes the possibility of mitochondrial inheritance. Crosses of the *Tvrm222* mice to non-mutagenized *Nr2e3^{rd7/rd7}* mice indicate that *Tvrm222* segregated with a semi-dominant inheritance pattern.

For genetic diseases inherited in a Mendelian fashion, disease expressivity can be affected by multiple factors, including environmental factors, allelic heterogeneity or modifier loci, etc. (191). Although the dysplastic photoreceptor phenotype found in *Nr2e3^{rd7/rd7}* mice is stable among affected individuals, the variability of the suppressive phenotype within individuals of the mapping cross suggests that genetic background modification may contribute to the phenotypic alterations of the *Tvrm222* phenotype.

It should be noted that the phenotypic outcomes in patients with *NR2E3* mutations as well as potential modifying effects are determined collectively by a multitude of factors, including the nature of *NR2E3* mutations, co-existence of multiple allelic modifiers, interactions between the modifiers and *NR2E3*, etc. For example, clinical presentations of patients bearing *NR2E3* disruptions are not homogeneous. The ESCS phenotypes in human patients are more variable in both funduscopy appearance and electrophysiology than those observed in *Nr2e3^{rd7/rd7}* mice (192, 193). Unlike the null mutation of *Nr2e3* in mice, different types of *NR2E3* mutation have been identified in ESCS patients. They are located in different regions of *NR2E3* gene and result in different transcriptional products, which may in turn contribute to the significant phenotypic

variations (64, 192-195). Modifier alleles may also influence variability of phenotypic outcomes among individuals as the identification of *Frmd4b*^{Tyrm222} allele in *Nr2e3*^{rd7/rd7} mice demonstrates. Interestingly, it is well documented that the FRMD4B^{938P} variant is equivalent to the supposedly wild type allele in both human and rat. A search for equivalent human *FRMD4B* variants (P991S) sharing similar features with the murine S938P variation in the Exome Aggregation Consortium (ExAC) database, identified only the following variations: P989T, N988S, Y987C, N985S. They are in the immediate vicinity of P991 and could conceivably alter FRMD4B functions in a similar fashion as S938P does in mouse. However, they exist with extremely low allele frequencies in the human population and are therefore, unlikely to act as general modifiers of ESCS. In addition to the direct homolog of the S938P variation, variants located in different domains of FRMD4B could differentially modify the phenotypes in human patients. Therefore, direct sequencing for *FRMD4B* variants in patients of ECSC or relevant retinopathies could be most informative in demonstrating whether *FRMD4B* and its variants can account for phenotypic variability in human individuals with *NR2E3* or *NRL* mutations.

Aligning the mouse and human FRMD4B sequences suggests at first glance that the human P991 residue is the equivalent of the mouse modifier. However, the region surrounding the mutation site (20 amino acids) is ~65% identical and is serine and proline rich. Therefore, the P991 allele in humans may not be functionally equivalent to mouse P938. In addition, it is often observed that deleterious alleles can be functionally rescued by a second *cis* mutation elsewhere in the protein (196). Therefore, it is possible that the human protein carrying P991 is functionally equivalent to the mouse protein carrying S938. Comparative localization experiments between the human and mouse proteins under insulin stimulation, as carried out in this study, may clarify this issue.

We also surveyed sequences surrounding the mutation site (40 amino acids) in different species and found that 44 sequences that are most closely related to the mouse sequence are from mammals, sharing ~ 60 – 70% sequence identity with laboratory mice. Most of these carry a proline at the site that is mutated in *Tvrm222* (P938). Among rodents, we noticed that rats, hamsters, moles, voles and peromyscus share the proline with other mammals whereas several *mus* species and a mole rat species (*Fukomys*) have serine in this position. In addition, beaver has threonine and a desert rodent (*Jaculus*) has an alanine. Further exceptions to the proline are boars (serine), porpoises (serine), deer (leucine), and bats (leucine). The distribution does not appear to be solely based on phylogeny but may also reflect *de novo* mutations within classes and orders.

The presence of S938 in most mouse strains suggests that it represents the wild type allele for mouse. Therefore, it is also possible that differing evolutionary pressures on the mouse genome lead to the fixation of the S938 allele. For instance, it was shown that mice maintain a basal metabolic rate normalized to body weight that is seven times greater than that of human beings (197). This might necessitate the presence of the S938 allele in mice to maintain higher activity of the insulin pathway (*i.e.* higher AKT phosphorylation) compared to the humans, in which the P991 allele is present. In specific respect to retina, insulin signaling is implicated in the birth of photoreceptors (198, 199). The genesis of photoreceptors, especially rod cells takes place much later in mice than that in human beings (31), which possibly demands higher sensitivity to insulin facilitated by the S938 allele. Therefore, it could be informative to characterize the biological effects of the FRMD4B isoforms in other organs in addition to retina.

In order to do this, a satisfactory antibody against FRMD4B or its *in vivo* labeling becomes indispensable. However, an antibody functioning in immunohistochemical studies was

not available, which confined the detection of *Frmd4b* only at the transcript level for the time being. In the future, development of a reliable antibody is necessary to better examine FRMD4B. According to our observations, the *Frmd4b* gene is ubiquitously expressed in multiple tissues and organs and produces three distinctive isoforms that are differentially expressed across tissues. Based on current knowledge about the distribution of *Frmd4b*, it potentially functions as a critical molecule implicated in fundamental biological processes, much of which remains elusive. Previous studies suggest that recessive mutations usually lead to phenotypic outcomes that are caused by a *loss of function* of a protein, while dominant mutations, albeit not always, lead to a *gain of function* (200). These observations gave us clues about the mechanism through which *Tvrm222* acts to enhance or confer new activities of gene products. Hence, further in-depth elucidations of the working machinery of FRMD4B and its 938P variant that mediates suppression of the dysplastic lesions in mice may provide insights into potential approaches to ameliorate retinal dysplasia.

4.3 The impact of S938P variation on biological properties of FRMD4B

4.3.1 Physical interactions of FRMD4B with its binding partners

Membrane recruitment of FRMD4B is largely dependent on the physical interaction between FRMD4B and CYTH3. In this study, we noted that the substitution of the serine residue 938 with proline in FRMD4B results in an alteration of cell-surface targeting of CYTH3-FRMD4B, which potentially underlies the modification of dysplastic lesions in mouse retinas. FRMD4B has been shown to act as an adaptor for the binding of CYTH3 with the PAR3-PAR6-aPKC complex. Among a series of amino acid sequence segments examined previously, the region of FRMD4B that was indispensable and sufficient for its localization with primordial cell junction components were amino acids 542-972 (116). Strikingly, the missense mutation in

Tyrm222 mice is located within this amino-acid region (542-972) of FRMD4B that directly binds PAR3. Therefore, it is reasonable to hypothesize that S938P variation alters the binding capacity of FRMD4B to PAR3. Future studies should particularly focus upon the binding affinity between FRMD4B and PAR3, as well as the biological consequences of the interaction at the molecular level.

4.3.2 *In-vitro* systems for elucidating biological properties of FRMD4B

In order to reveal the biological properties of FRMD4B as well as its 938P variant, *in-vitro* observations are indispensable. Different cell lines were chosen for different aspects of this study. COS (CV-1 in origin with SV40 genes) 7 cells are derived from kidney of the African green monkey that resemble fibroblast cells. Typically, COS-7 cells display adherent growth. COS-7 cells were utilized to better visualize the intracellular localization of the FRMD4B molecule. Generally, COS-7 cells are readily transfectable with plasmid DNA (201). More importantly, COS-7 cells enabled us to distinctly view intracellular localization of FMRD4B in respect to distinct features of cell morphology. 293T cells on the other hand, an important variant of HEK 293 cells, which stands for Human Embryonic Kidney 293 cells, are derived from human embryonic kidney cells and contain the SV40 large T-antigen that allows for episomal replication of transfected plasmid containing the SV40 origin of replication (202). The expression of the T-antigen facilitates amplification of transfected plasmids and extends temporal expression of transfected products (202). This cell line is extensively used in transgenic studies due to high transfection efficiency, which confers high protein yield of desired gene products. Additionally, in order to investigate the adhesive properties of cells transfected with CYTH3-FRMD4B *in vitro*, we attempted to use MDCK (Madin-Darby canine kidney) cells, a cell line derived from the kidney tissue of an adult female cocker spaniel, which exhibits

epithelial morphology and behaviors. MDCK cells are widely used as a model for studying apico-basolateral polarity and cell junctions that comprise essential characteristics of epithelia (203). Ideally, MDCK cells would have enabled us to test the effect of CYTH3-FRMD4B^{938P} on cell junction dynamics *in vitro*. However, the transfection efficiency of MDCK cells by lipid-based transfection, electroporation, etc. was extremely low and poor epithelial morphology was observed after transfection. Also, whether cell junctions of MDCK cells are similar to adhesive properties between cells of the retina is unknown as cell junctions of different cell types might differ and not be regulated by the CYTH3-FRMD4B complex in the same fashion in the epithelial context.

Reduced efficiency of membrane recruitment of the FRMD4B^{938P} variant revealed by both immunocytochemistry and subcellular fractionation assays is a key discovery of this study. While the immunocytochemistry indicates clearly that FRMD4B^{938P} does not translocate to the membrane from the cytoplasm efficiently, such definitive results for the subcellular fractionation assay was somewhat ambiguous. Technique wise, the fractionated proteins assayed by SDS-PAGE in determining translocation of given molecules from one fraction to another within a given individual was not clear cut. Potential reasons for this include: 1) protein content associated with different fractions of the same individual is less comparable as a proper control for the comparison is lacking in this study; 2) cell-surface targeting efficiency of FRMD4B is not known, which might be helpful in determining the amount of protein relocated to cell surface from the cytosol. Therefore, the protein load for blotting is empirical and not precise enough for quantification purpose between cytosolic content and membrane content. In addition, it must be noted that all the *in-vitro* data were generated based on the transient transfection of cells. Conclusions of the study were based on the assumption that the transfection rate remained the

same, and cells were evenly transfected across groups. In order to quantify the results more accurately, generating stable cell lines is definitely a desirable approach. However, both pCMV-3Tag-1A-*Cyth3* and pCMV-3Tag-2B-*Frmd4b* bear kanamycin and ampicillin resistant coding sequences. Colony picking by antibiotic selection fails to differentiate the two inserts and will not be viable for generating stable cell lines. Alternative approaches should be considered, including fluorescence-activated cell sorting, etc.

Finally, it is worth noting that the FRMD4B isoform 3 (NP_660130.2), which encompasses the shared carboxyl terminal amino acid sequences of the longer isoforms expressed in brain and lung, was used in our *in-vitro* studies. We specifically selected FRMD4B isoform 3 as it shares the most domains including a FERM domain, two coiled-coil domains and a serine/threonine rich domain with the other isoforms. The difference among the isoforms takes place at the amino terminus but it is predicted that the amino terminus, for example, in the lung variant is presumably not translated (114). Admittedly, additional future studies to understand the functional consequences of the different isoforms of FRMD4B (Table 2.6) would be beneficial as the isoforms are likely to function differentially across multiple tissues and organs.

4.4 Signaling pathways that mediate functions of the CYTH3-FRMD4B complex

Our study also established, for the first time to our knowledge, a linkage between altered CYTH3-FRMD4B membrane recruitment and modification of cell junction phenotypes, as well as an effect on both ARF6 and AKT in the presence of the *Frmd4b*^{Tvrm222} allele. Previous investigations as well as our own results, indicate that regulation of cell junctions by CYTH3-FRMD4B is complex as multiple pathways appear to be implicated.

We determined through both *in vitro* and *in vivo* studies that the GTP/GDP cycling of ARF6 was significantly skewed to the GTP binding form in response to reduced membrane

recruitment of CYTH3-FRMD4B complex. According to previous reports, activation of ARF6 regulates both AJ assembly and disassembly, depending upon its binding to signaling complexes (115). The differences in results may be due to the cell types involved. Interestingly, the majority of previous investigations were focused on homotypic cell junctions in epithelium, but not between neuronal cells. Our study examines the ELM, which consists of heterotypic cell junctions between photoreceptors and Müller glia. Our results imply that increased cell junction-associated proteins at the ELM are linked to elevated ARF6 activation. This suggests that the regulation of heterotypic cell junctions such as that observed for the ELM may be different than other homotypic cell junctions in other tissues. Examination of both neuronal and heterotypic cell junctions deserves further investigation.

It is generally accepted that CYTH3 catalyzes GTP binding to ARF6 at the cell surface (204, 205). FRMD4B-mediated membrane recruitment of CYTH3 serves as a critical mechanism for activation of ARF6 (116). Meanwhile, it becomes complicated that activation of ARF6 can reciprocally serve as a prerequisite for membrane recruitment of CYTH3 – constitutively activated ARF6 is capable of recruiting CYTH3 to the cell surface according to some previous investigations (206). Whether other cell-surface targeting mechanisms can impact ARF6 GTP/GDP exchange is unknown. However, a critical determinant to ARF6 activation may be the cell-type involved. For instance, co-localization of FRMD4B-CYTH3-PAR3 varies among different cell types (116), which could presumably affect activation of ARF6. Additionally, auto-regulatory mechanisms of GEFs could also play a role in the regulation of ARF6 (207). However, a limitation of the *in-vitro* system with transient transfections is that it does not allow for assessment of potential feedback and/or compensatory mechanisms. Unlike the previous studies, which directly introduced constitutively (in)active ARF6 (208, 209), the ARF6 activation in this

study is more likely to be a secondary response towards the alteration in FRMD4B membrane recruitment, which implies an alternative regulatory system between ARF6 and the GEF.

Another key finding revealed by this study is the downregulation of AKT phosphorylation in the presence *Frmd4b*^{Tyrm222} variant in mouse retinas. This study was primarily focused on dysplastic lesions in retina. Its histologic and cellular characteristics, such as delamination, loss of cell junctions and polarity, etc. are reminiscent of other pathological processes, including EMT, neoplastic transformation, etc. In fact, it is well established that AKT pathway regulates a variety of pathophysiological processes, including developmental defects, metabolic disorders, tumorigenesis, etc. This prompted us to examine the impact of the FRMD4B on the AKT pathway. Conceivably, regulation of PI3K-AKT by FRMD4B may be significant for its translational applications in clinics due to broad and profound implications of PI3K-AKT pathway in a variety of pathological processes.

The regulatory relationship among CYTH3-FRMD4B, ARF6 and AKT is intricate and has yet to be fully elucidated. According to the previous studies, ARF6 activates phosphatidylinositol 4-phosphate 5 kinase (PIP5K) to generate PIP₂, which can be further converted to PIP₃ for phosphorylation of AKT (210). In addition, ARF6 might also be spatially adjacent to AKT at the cell surface due to the interaction of ARF6 with the PAR complex, which is closely linked to phosphoinositides signaling events (211). Hence, it is possible that ARF6 and AKT may be closely linked and FRMD4B, as a scaffold protein, serves as a novel platform, upon which ARF6 and AKT can interact to coordinate their biological functions (Figure 27). Further studies are necessary to determine whether the effects of the CYTH3-FRMD4B complex on ARF6 and AKT are achieved in a hierarchical manner or as independent parallel effects.

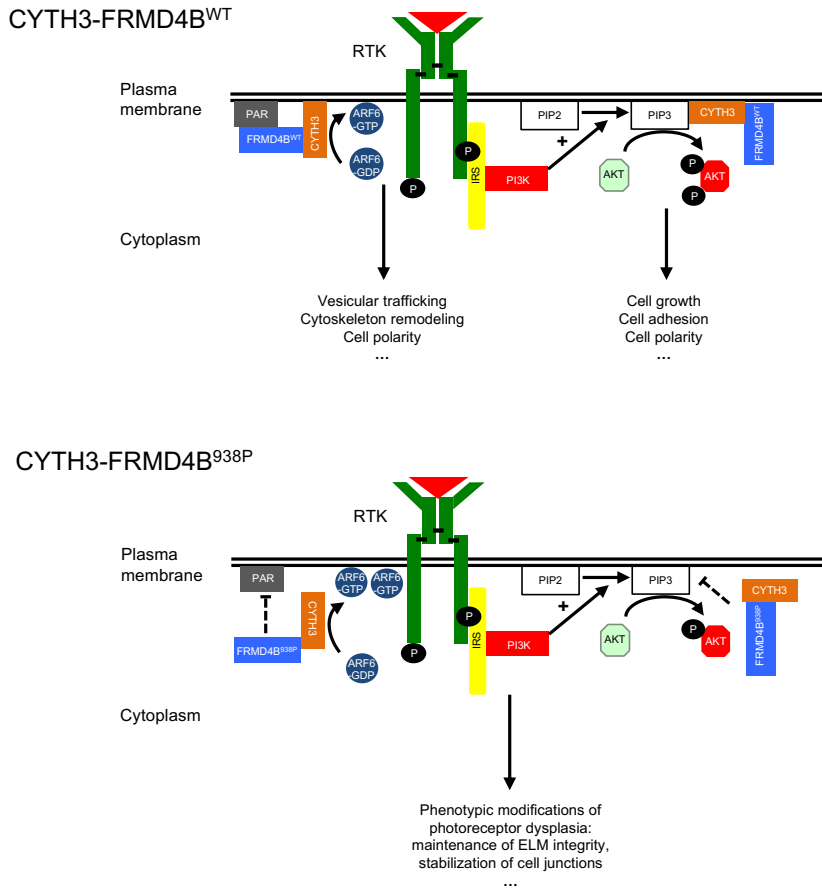


Figure 27. Working model of interactions of CYTH3-FRMD4B complex with AKT and ARF6 pathways for modifying retinal dysplasia based on the information from the cited literatures and our finding in this study. Upper panel: Potential association CYTH3-FRMD4B^{WT} with ARF6 and/or AKT pathways at the cell surface for generating a variety of biological consequences. Lower panel: A reduced cell-surface targeting of CYTH3-FRMD4B^{938P} and its influence on rescuing photoreceptor dysplasia. AKT: protein kinase B, ARF6: ADP-ribosylation factor 6, CYTH3: cytohesin 3, PAR: Par3-Par6-aPKC, IRS: insulin receptor substrate, RTK: receptor tyrosine kinase, P: phosphate group, PI3K: phosphatidylinositol-4,5-bisphosphate 3-kinase, PIP2: phosphatidylinositol 4,5-bisphosphate, PIP3: phosphatidylinositol (3,4,5)-trisphosphate,

CHAPTER 5

CONCLUDING REMARKS AND FUTURE DIRECTIONS

The importance of proper development of retinal precursor cells and the establishment of cell-cell contact between photoreceptors and their neighboring Müller glial cells to maintain retinal integrity and structural stability of the retina was substantiated in this study. Disruption of junctional components may drive pathological changes or respond to disease phenotypes and further deteriorate the pathological consequences. Currently, the ELM provides a classic example where anomalies in cell junctions in the retina can be associated with or cause retinal disorders. According to our observations, fragmented ELM is closely related to photoreceptor dysplasia in *rd7* mice. More importantly, we identified a novel genetic modifier, *Frmd4b*^{*Tvrm222*}, that effects cell junctions at the level of the ELM and suppresses photoreceptor dysplasia caused by deficiencies of either *Nr2e3* or *Nrl*. FRMD4B is a scaffold protein that is known to physically interact with the PAR complex, CYTH3 and ARF6 to modulate cell junction remodeling, cytoskeletal dynamics and epithelial polarization (116). At the molecular level, we noted that compared to the wild type, FRMD4B^{938P} is less efficiently recruited to the cell surface. Additionally, both activation of ARF6 and reduced phosphorylation of AKT was observed, which are potentially associated with increased expression of cell junction molecules at the cell surface in *Tvrm222* retinas. Cell-cell contact appears to be stabilized and fragmentation of ELM is prevented. This is associated with a reduction in dysplastic lesions in both *rd7* and *Nrl*^{-/-} mouse retinas.

Despite the fact that FRMD4B was first isolated more than a decade ago, little knowledge has been obtained since then with respect to its biological properties and the consequences of its involvement in potential pathophysiological conditions. Some of the pilot genome-wide analyses

disclosed likely involvement of multiple FRMD4B variants in diseased conditions, including neuronal degeneration, lachrymal/salivary gland lesions, chronic obstructive pulmonary disease, late onset Alzheimer's disease, cardiomyopathy and celiac disease (212-215). Comprehensive studies to validate its role in given diseases and the mechanisms underlying the observed pathologies are yet to be done.

This study demonstrates a key role of FRMD4B and its missense variant in maintaining cell junctions in the context of dysplastic lesion and indicates a potential influence of FRMD4B on ARF6 and AKT signaling pathways. In the future, it is important that we address in what manner FRMD4B modulates the biological functions of ARF6 and AKT. These effects could be tested by *in-vitro* co-transfection of constitutively activated ARF6 and AKT, and by manipulation of FRMD4B expression to characterize intracellular localization of ARF6 and AKT as well as their potential reliance on FRMD4B for coordination and propagation of intracellular signals. Analyses of *Tvrm222-Akt^{-/-}* and *Tvrm222-Arf6^{-/-}* double mutants will reveal contributions of these pathways to rescuing dysplastic phenotypes *in vivo*. This will provide us with more detailed knowledge about the regulatory mechanisms that control cell junction dynamics in the retina and allow us to discover interacting targets that collectively influence tissue homeostasis and function of the retina.

Finally, from the perspective of therapeutics, exploration of FRMD4B could be useful to provide a target in the application of *in situ* engraftment of photoreceptor transplants to treat retinal degenerative disorders since ELM integrity is closely related to therapeutic outcomes of transplantation in retina (216). In a broader sense, regulating FRMD4B may also be extrapolated in other pathophysiological processes due to its potential involvement in both ARF6 and AKT pathways, which are central to tissue repair, regeneration, neoplasm, etc. By probing into the

working machinery of FRMD4B, we anticipate an extensive implication of this molecule in a wide spectrum of biological processes, as well as its therapeutic prospect in clinics.

REFERENCES

1. Bourne RRA, *et al.* (2017) Magnitude, temporal trends, and projections of the global prevalence of blindness and distance and near vision impairment: a systematic review and meta-analysis. *Lancet Glob Health* 5(9):e888-e897.
2. Masland RH (2001) The fundamental plan of the retina. *Nat Neurosci* 4(9):877-886.
3. Asai H, Chiba T, Kimura S, & Takagi M (1975) A light-induced conformational change in rod photoreceptor disc membrane. *Exp Eye Res* 21(3):259-267.
4. DeGrip WJ, *et al.* (1988) Photoexcitation of rhodopsin: conformation changes in the chromophore, protein and associated lipids as determined by FTIR difference spectroscopy. *Photochem Photobiol* 48(4):497-504.
5. Fu Y (1995) Phototransduction in Rods and Cones. *Webvision: The Organization of the Retina and Visual System*, eds Kolb H, Fernandez E, & Nelson RSalt Lake City (UT)).
6. Kefalov VJ (2012) Rod and cone visual pigments and phototransduction through pharmacological, genetic, and physiological approaches. *J Biol Chem* 287(3):1635-1641.
7. Chaitin MH, Schneider BG, Hall MO, & Papermaster DS (1984) Actin in the photoreceptor connecting cilium: immunocytochemical localization to the site of outer segment disk formation. *J Cell Biol* 99(1 Pt 1):239-247.
8. Wolf G (2004) The visual cycle of the cone photoreceptors of the retina. *Nutr Rev* 62(7 Pt 1):283-286.
9. Mustafi D, Engel AH, & Palczewski K (2009) Structure of cone photoreceptors. *Prog Retin Eye Res* 28(4):289-302.
10. Kawamura S & Tachibanaki S (2008) Rod and cone photoreceptors: molecular basis of the difference in their physiology. *Comp Biochem Physiol A Mol Integr Physiol* 150(4):369-377.
11. Ortin-Martinez A, *et al.* (2014) Number and distribution of mouse retinal cone photoreceptors: differences between an albino (Swiss) and a pigmented (C57/BL6) strain. *PLoS One* 9(7):e102392.

12. Ebrey T & Koutalos Y (2001) Vertebrate photoreceptors. *Prog Retin Eye Res* 20(1):49-94.
13. Jacobs GH, Williams GA, & Fenwick JA (2004) Influence of cone pigment coexpression on spectral sensitivity and color vision in the mouse. *Vision Res* 44(14):1615-1622.
14. Stockman A, MacLeod DI, & Johnson NE (1993) Spectral sensitivities of the human cones. *J Opt Soc Am A Opt Image Sci Vis* 10(12):2491-2521.
15. Jonas JB, Schneider U, & Naumann GO (1992) Count and density of human retinal photoreceptors. *Graefes Arch Clin Exp Ophthalmol* 230(6):505-510.
16. Ahnelt PK (1998) The photoreceptor mosaic. *Eye (Lond)* 12 (Pt 3b):531-540.
17. Jeon CJ, Strettoi E, & Masland RH (1998) The major cell populations of the mouse retina. *J Neurosci* 18(21):8936-8946.
18. Carter-Dawson LD & LaVail MM (1979) Rods and cones in the mouse retina. I. Structural analysis using light and electron microscopy. *J Comp Neurol* 188(2):245-262.
19. Curcio CA, Sloan KR, Kalina RE, & Hendrickson AE (1990) Human photoreceptor topography. *J Comp Neurol* 292(4):497-523.
20. Farber DB, Flannery JG, Lolley RN, & Bok D (1985) Distribution patterns of photoreceptors, protein, and cyclic nucleotides in the human retina. *Invest Ophthalmol Vis Sci* 26(11):1558-1568.
21. Zhang T, *et al.* (2015) Variability in Human Cone Topography Assessed by Adaptive Optics Scanning Laser Ophthalmoscopy. *Am J Ophthalmol* 160(2):290-300 e291.
22. Curcio CA, Sloan KR, Jr., Packer O, Hendrickson AE, & Kalina RE (1987) Distribution of cones in human and monkey retina: individual variability and radial asymmetry. *Science* 236(4801):579-582.
23. Anonymous (1937) Topography of the layer of rods and cones in the human retina. *Journal of the American Medical Association* 108(3):232-232.

24. Palczewski K (2006) G protein-coupled receptor rhodopsin. *Annu Rev Biochem* 75:743-767.
25. Filipek S, Stenkamp RE, Teller DC, & Palczewski K (2003) G protein-coupled receptor rhodopsin: a prospectus. *Annu Rev Physiol* 65:851-879.
26. Chabre M & Deterre P (1989) Molecular mechanism of visual transduction. *Eur J Biochem* 179(2):255-266.
27. Fu Y & Yau KW (2007) Phototransduction in mouse rods and cones. *Pflugers Arch* 454(5):805-819.
28. Yau KW (1994) Phototransduction mechanism in retinal rods and cones. The Friedenwald Lecture. *Invest Ophthalmol Vis Sci* 35(1):9-32.
29. Yau KW & Baylor DA (1989) Cyclic GMP-activated conductance of retinal photoreceptor cells. *Annu Rev Neurosci* 12:289-327.
30. Gotz M & Huttner WB (2005) The cell biology of neurogenesis. *Nat Rev Mol Cell Biol* 6(10):777-788.
31. Brzezinski JA & Reh TA (2015) Photoreceptor cell fate specification in vertebrates. *Development* 142(19):3263-3273.
32. Carter-Dawson LD & LaVail MM (1979) Rods and cones in the mouse retina. II. Autoradiographic analysis of cell generation using tritiated thymidine. *J Comp Neurol* 188(2):263-272.
33. Young RW (1985) Cell differentiation in the retina of the mouse. *Anat Rec* 212(2):199-205.
34. Cepko CL, Austin CP, Yang X, Alexiades M, & Ezzeddine D (1996) Cell fate determination in the vertebrate retina. *Proc Natl Acad Sci U S A* 93(2):589-595.
35. van Ginkel PR & Hauswirth WW (1994) Parallel regulation of fetal gene expression in different photoreceptor cell types. *J Biol Chem* 269(7):4986-4992.

36. Bassett EA & Wallace VA (2012) Cell fate determination in the vertebrate retina. *Trends Neurosci* 35(9):565-573.
37. Harris WA (1997) Cellular diversification in the vertebrate retina. *Curr Opin Genet Dev* 7(5):651-658.
38. Edlund T & Jessell TM (1999) Progression from extrinsic to intrinsic signaling in cell fate specification: a view from the nervous system. *Cell* 96(2):211-224.
39. Livesey FJ & Cepko CL (2001) Vertebrate neural cell-fate determination: lessons from the retina. *Nat Rev Neurosci* 2(2):109-118.
40. Lillien L & Cepko C (1992) Control of proliferation in the retina: temporal changes in responsiveness to FGF and TGF alpha. *Development* 115(1):253-266.
41. Fischer AJ (2005) Neural regeneration in the chick retina. *Prog Retin Eye Res* 24(2):161-182.
42. Lamba DA, Karl MO, Ware CB, & Reh TA (2006) Efficient generation of retinal progenitor cells from human embryonic stem cells. *Proc Natl Acad Sci U S A* 103(34):12769-12774.
43. Wang Y, *et al.* (2018) Insulin-like growth factor-1 regulation of retinal progenitor cell proliferation and differentiation. *Cell Cycle*:1-35.
44. Mellough CB, *et al.* (2015) IGF-1 Signaling Plays an Important Role in the Formation of Three-Dimensional Laminated Neural Retina and Other Ocular Structures From Human Embryonic Stem Cells. *Stem Cells* 33(8):2416-2430.
45. Lillien L (1995) Changes in retinal cell fate induced by overexpression of EGF receptor. *Nature* 377(6545):158-162.
46. Mo A, *et al.* (2016) Epigenomic landscapes of retinal rods and cones. *Elife* 5:e11613.
47. Hughes AE, Enright JM, Myers CA, Shen SQ, & Corbo JC (2017) Cell Type-Specific Epigenomic Analysis Reveals a Uniquely Closed Chromatin Architecture in Mouse Rod Photoreceptors. *Sci Rep* 7:43184.

48. Rao RC, Hennig AK, Malik MT, Chen DF, & Chen S (2011) Epigenetic regulation of retinal development and disease. *J Ocul Biol Dis Infor* 4(3):121-136.
49. Swaroop A, Kim D, & Forrest D (2010) Transcriptional regulation of photoreceptor development and homeostasis in the mammalian retina. *Nat Rev Neurosci* 11(8):563-576.
50. Nishida A, *et al.* (2003) Otx2 homeobox gene controls retinal photoreceptor cell fate and pineal gland development. *Nat Neurosci* 6(12):1255-1263.
51. Koike C, *et al.* (2007) Functional roles of Otx2 transcription factor in postnatal mouse retinal development. *Mol Cell Biol* 27(23):8318-8329.
52. Furukawa T, Morrow EM, & Cepko CL (1997) Crx, a novel otx-like homeobox gene, shows photoreceptor-specific expression and regulates photoreceptor differentiation. *Cell* 91(4):531-541.
53. Mitton KP, *et al.* (2000) The leucine zipper of NRL interacts with the CRX homeodomain. A possible mechanism of transcriptional synergy in rhodopsin regulation. *J Biol Chem* 275(38):29794-29799.
54. Jia L, *et al.* (2009) Retinoid-related orphan nuclear receptor RORbeta is an early-acting factor in rod photoreceptor development. *Proc Natl Acad Sci U S A* 106(41):17534-17539.
55. Rehemtulla A, *et al.* (1996) The basic motif-leucine zipper transcription factor Nrl can positively regulate rhodopsin gene expression. *Proc Natl Acad Sci U S A* 93(1):191-195.
56. Mears AJ, *et al.* (2001) Nrl is required for rod photoreceptor development. *Nat Genet* 29(4):447-452.
57. Chen J, Rattner A, & Nathans J (2005) The rod photoreceptor-specific nuclear receptor Nr2e3 represses transcription of multiple cone-specific genes. *J Neurosci* 25(1):118-129.
58. Hennig AK, Peng GH, & Chen S (2008) Regulation of photoreceptor gene expression by Crx-associated transcription factor network. *Brain Res* 1192:114-133.
59. Sohocki MM, *et al.* (1998) A range of clinical phenotypes associated with mutations in CRX, a photoreceptor transcription-factor gene. *Am J Hum Genet* 63(5):1307-1315.

60. Swaroop A, *et al.* (1999) Leber congenital amaurosis caused by a homozygous mutation (R90W) in the homeodomain of the retinal transcription factor CRX: direct evidence for the involvement of CRX in the development of photoreceptor function. *Hum Mol Genet* 8(2):299-305.
61. Nichols LL, 2nd, *et al.* (2010) Two novel CRX mutant proteins causing autosomal dominant Leber congenital amaurosis interact differently with NRL. *Hum Mutat* 31(6):E1472-1483.
62. Bessant DA, *et al.* (1999) A mutation in NRL is associated with autosomal dominant retinitis pigmentosa. *Nat Genet* 21(4):355-356.
63. Haider NB, *et al.* (2000) Mutation of a nuclear receptor gene, NR2E3, causes enhanced S cone syndrome, a disorder of retinal cell fate. *Nat Genet* 24(2):127-131.
64. Schorderet DF & Escher P (2009) NR2E3 mutations in enhanced S-cone sensitivity syndrome (ESCS), Goldmann-Favre syndrome (GFS), clumped pigmentary retinal degeneration (CPRD), and retinitis pigmentosa (RP). *Hum Mutat* 30(11):1475-1485.
65. Yang Y, *et al.* (2010) Association of NR2E3 but not NRL mutations with retinitis pigmentosa in the Chinese population. *Invest Ophthalmol Vis Sci* 51(4):2229-2235.
66. Haider NB, *et al.* (2009) Nr2e3-directed transcriptional regulation of genes involved in photoreceptor development and cell-type specific phototransduction. *Exp Eye Res* 89(3):365-372.
67. Webber AL, *et al.* (2008) Dual role of Nr2e3 in photoreceptor development and maintenance. *Exp Eye Res* 87(1):35-48.
68. Rich KA, Figueroa SL, Zhan Y, & Blanks JC (1995) Effects of Muller cell disruption on mouse photoreceptor cell development. *Exp Eye Res* 61(2):235-248.
69. Streit WJ, Graeber MB, & Kreutzberg GW (1988) Functional plasticity of microglia: a review. *Glia* 1(5):301-307.
70. Araque A & Navarrete M (2010) Glial cells in neuronal network function. *Philos Trans R Soc Lond B Biol Sci* 365(1551):2375-2381.

71. Rasband MN (2016) Glial Contributions to Neural Function and Disease. *Mol Cell Proteomics* 15(2):355-361.
72. Turner DL & Cepko CL (1987) A common progenitor for neurons and glia persists in rat retina late in development. *Nature* 328(6126):131-136.
73. Bringmann A, et al. (2006) Muller cells in the healthy and diseased retina. *Prog Retin Eye Res* 25(4):397-424.
74. Reichenbach A & Bringmann A (2013) New functions of Muller cells. *Glia* 61(5):651-678.
75. Goldman D (2014) Muller glial cell reprogramming and retina regeneration. *Nat Rev Neurosci* 15(7):431-442.
76. Dyer MA & Cepko CL (2000) Control of Muller glial cell proliferation and activation following retinal injury. *Nat Neurosci* 3(9):873-880.
77. Alberts B JA, Lewis J, et al. (2002) Cell Junctions. . *Molecular Biology of the Cell. 4th edition.* , (Garland Science, New York).
78. Zihni C, Mills C, Matter K, & Balda MS (2016) Tight junctions: from simple barriers to multifunctional molecular gates. *Nat Rev Mol Cell Biol* 17(9):564-580.
79. Ivanov AI & Naydenov NG (2013) Chapter Two - Dynamics and Regulation of Epithelial Adherens Junctions: Recent Discoveries and Controversies. *International Review of Cell and Molecular Biology*, ed Jeon KW (Academic Press), Vol 303, pp 27-99.
80. Cavey M & Lecuit T (2009) Molecular bases of cell-cell junctions stability and dynamics. *Cold Spring Harb Perspect Biol* 1(5):a002998.
81. Anonymous (2017) Chapter 31 - Intercellular Junctions A2 - Pollard, Thomas D. *Cell Biology (Third Edition)*, eds Earnshaw WC, Lippincott-Schwartz J, & Johnson GT (Elsevier), pp 543-553.
82. Hartsock A & Nelson WJ (2008) Adherens and tight junctions: structure, function and connections to the actin cytoskeleton. *Biochim Biophys Acta* 1778(3):660-669.

83. Tepass U & Harris KP (2007) Adherens junctions in Drosophila retinal morphogenesis. *Trends Cell Biol* 17(1):26-35.
84. Niessen CM (2007) Tight junctions/adherens junctions: basic structure and function. *J Invest Dermatol* 127(11):2525-2532.
85. Cereijido M, Shoshani L, & Contreras RG (2000) Molecular physiology and pathophysiology of tight junctions. I. Biogenesis of tight junctions and epithelial polarity. *Am J Physiol Gastrointest Liver Physiol* 279(3):G477-482.
86. Balda MS & Matter K (2000) Transmembrane proteins of tight junctions. *Semin Cell Dev Biol* 11(4):281-289.
87. Chiba H, Osanai M, Murata M, Kojima T, & Sawada N (2008) Transmembrane proteins of tight junctions. *Biochim Biophys Acta* 1778(3):588-600.
88. Matter K & Balda MS (2003) Signalling to and from tight junctions. *Nat Rev Mol Cell Biol* 4(3):225-236.
89. Campbell M, *et al.* (2006) Aberrant retinal tight junction and adherens junction protein expression in an animal model of autosomal dominant Retinitis pigmentosa: the Rho(-/-) mouse. *Exp Eye Res* 83(3):484-492.
90. Davidson MK, *et al.* (2000) Reduced expression of the adherens junction protein cadherin-5 in a diabetic retina. *Am J Ophthalmol* 129(2):267-269.
91. Forster C (2008) Tight junctions and the modulation of barrier function in disease. *Histochem Cell Biol* 130(1):55-70.
92. Omri S, *et al.* (2010) The outer limiting membrane (OLM) revisited: clinical implications. *Clin Ophthalmol* 4:183-195.
93. Burke TR, *et al.* (2013) Abnormality in the external limiting membrane in early Stargardt disease. *Ophthalmic Genet* 34(1-2):75-77.
94. Lee W, *et al.* (2014) The external limiting membrane in early-onset Stargardt disease. *Invest Ophthalmol Vis Sci* 55(10):6139-6149.

95. Albert DM, Lahav M, Colby ED, Shaddock JA, & Sang DN (1977) Retinal neoplasia and dysplasia. I. Induction by feline leukemia virus. *Invest Ophthalmol Vis Sci* 16(4):325-337.
96. Wilkie DA (2011) Chapter 10 - Diseases of the Ocular Posterior Segment A2 - Gilger, Brian C. *Equine Ophthalmology (Second Edition)*, (W.B. Saunders, Saint Louis), pp 367-396.
97. Silverstein AM, Osburn BI, & Prendergast RA (1971) The pathogenesis of retinal dysplasia. *Am J Ophthalmol* 72(1):13-21.
98. Stuck MW, Conley SM, & Naash MI (2012) Defects in the outer limiting membrane are associated with rosette development in the *Nrl*^{-/-} retina. *PLoS One* 7(3):e32484.
99. Whiteley HE (1991) Dysplastic canine retinal morphogenesis. *Invest Ophthalmol Vis Sci* 32(5):1492-1498.
100. Haider NB, Naggert JK, & Nishina PM (2001) Excess cone cell proliferation due to lack of a functional NR2E3 causes retinal dysplasia and degeneration in rd7/rd7 mice. *Hum Mol Genet* 10(16):1619-1626.
101. Mehalow AK, *et al.* (2003) CRB1 is essential for external limiting membrane integrity and photoreceptor morphogenesis in the mammalian retina. *Hum Mol Genet* 12(17):2179-2189.
102. Tepass U, Theres C, & Knust E (1990) crumbs encodes an EGF-like protein expressed on apical membranes of Drosophila epithelial cells and required for organization of epithelia. *Cell* 61(5):787-799.
103. Izaddoost S, Nam SC, Bhat MA, Bellen HJ, & Choi KW (2002) Drosophila Crumbs is a positional cue in photoreceptor adherens junctions and rhabdomeres. *Nature* 416(6877):178-183.
104. Richard M, *et al.* (2006) Towards understanding CRUMBS function in retinal dystrophies. *Hum Mol Genet* 15 Spec No 2:R235-243.
105. Aleman TS, *et al.* (2011) Human CRB1-associated retinal degeneration: comparison with the rd8 *Crb1*-mutant mouse model. *Invest Ophthalmol Vis Sci* 52(9):6898-6910.

106. von Alpen D, *et al.* (2015) Differential dimerization of variants linked to enhanced S-cone sensitivity syndrome (ESCS) located in the NR2E3 ligand-binding domain. *Hum Mutat* 36(6):599-610.
107. Sharon D, Sandberg MA, Caruso RC, Berson EL, & Dryja TP (2003) Shared mutations in NR2E3 in enhanced S-cone syndrome, Goldmann-Favre syndrome, and many cases of clumped pigmentary retinal degeneration. *Arch Ophthalmol* 121(9):1316-1323.
108. Blanco-Kelly F, *et al.* (2016) Dominant Retinitis Pigmentosa, p.Gly56Arg Mutation in NR2E3: Phenotype in a Large Cohort of 24 Cases. *PLoS One* 11(2):e0149473.
109. Haider NB, *et al.* (2008) Mapping of genetic modifiers of Nr2e3 rd7/rd7 that suppress retinal degeneration and restore blue cone cells to normal quantity. *Mamm Genome* 19(3):145-154.
110. Cruz NM, *et al.* (2014) Modifier genes as therapeutics: the nuclear hormone receptor Rev Erb alpha (Nr1d1) rescues Nr2e3 associated retinal disease. *PLoS One* 9(1):e87942.
111. Nystuen AM, Sachs AJ, Yuan Y, Heuermann L, & Haider NB (2008) A novel mutation in Prph2, a gene regulated by Nr2e3, causes retinal degeneration and outer-segment defects similar to Nr2e3 (rd7/rd7) retinas. *Mamm Genome* 19(9):623-633.
112. Balling R (2001) ENU mutagenesis: analyzing gene function in mice. *Annu Rev Genomics Hum Genet* 2:463-492.
113. Acevedo-Arozena A, *et al.* (2008) ENU mutagenesis, a way forward to understand gene function. *Annu Rev Genomics Hum Genet* 9:49-69.
114. Klarlund JK, *et al.* (2001) Signaling complexes of the FERM domain-containing protein GRSP1 bound to ARF exchange factor GRP1. *J Biol Chem* 276(43):40065-40070.
115. Donaldson JG & Jackson CL (2011) ARF family G proteins and their regulators: roles in membrane transport, development and disease. *Nat Rev Mol Cell Biol* 12(6):362-375.
116. Ikenouchi J & Umeda M (2010) FRMD4A regulates epithelial polarity by connecting Arf6 activation with the PAR complex. *Proc Natl Acad Sci U S A* 107(2):748-753.

117. Mansour M, Lee SY, & Pohajdak B (2002) The N-terminal coiled coil domain of the cytohesin/ARNO family of guanine nucleotide exchange factors interacts with the scaffolding protein CASP. *J Biol Chem* 277(35):32302-32309.
118. MacNeil AJ & Pohajdak B (2009) Getting a GRASP on CASP: properties and role of the cytohesin-associated scaffolding protein in immunity. *Immunol Cell Biol* 87(1):72-80.
119. Pan CQ, Sudol M, Sheetz M, & Low BC (2012) Modularity and functional plasticity of scaffold proteins as p(1)acemakers in cell signaling. *Cell Signal* 24(11):2143-2165.
120. Shaw AS & Filbert EL (2009) Scaffold proteins and immune-cell signalling. *Nat Rev Immunol* 9(1):47-56.
121. Herrmann A, Tillmann BA, Schurmann J, Bolker M, & Tudzynski P (2014) Small-GTPase-associated signaling by the guanine nucleotide exchange factors CpDock180 and CpCdc24, the GTPase effector CpSte20, and the scaffold protein CpBem1 in *Claviceps purpurea*. *Eukaryot Cell* 13(4):470-482.
122. Good MC, Zalatan JG, & Lim WA (2011) Scaffold proteins: hubs for controlling the flow of cellular information. *Science* 332(6030):680-686.
123. Zeke A, Lukacs M, Lim WA, & Remenyi A (2009) Scaffolds: interaction platforms for cellular signalling circuits. *Trends Cell Biol* 19(8):364-374.
124. Lim J, Zhou M, Veenstra TD, & Morrison DK (2010) The CNK1 scaffold binds cytohesins and promotes insulin pathway signaling. *Genes Dev* 24(14):1496-1506.
125. Casanova JE (2007) Regulation of Arf activation: the Sec7 family of guanine nucleotide exchange factors. *Traffic* 8(11):1476-1485.
126. Bos JL, Rehmann H, & Wittinghofer A (2007) GEFs and GAPs: critical elements in the control of small G proteins. *Cell* 129(5):865-877.
127. Mayer G, *et al.* (2001) Controlling small guanine-nucleotide-exchange factor function through cytoplasmic RNA intramers. *Proc Natl Acad Sci U S A* 98(9):4961-4965.
128. Zeeh JC, *et al.* (2006) Dual specificity of the interfacial inhibitor brefeldin a for arf proteins and sec7 domains. *J Biol Chem* 281(17):11805-11814.

129. He X, Kuo YC, Rosche TJ, & Zhang X (2013) Structural basis for autoinhibition of the guanine nucleotide exchange factor FARP2. *Structure* 21(3):355-364.
130. Baumeister MA, Rossman KL, Sondek J, & Lemmon MA (2006) The Dbs PH domain contributes independently to membrane targeting and regulation of guanine nucleotide-exchange activity. *Biochem J* 400(3):563-572.
131. Lemmon MA (2003) Phosphoinositide recognition domains. *Traffic* 4(4):201-213.
132. Malaby AW, van den Berg B, & Lambright DG (2013) Structural basis for membrane recruitment and allosteric activation of cytohesin family Arf GTPase exchange factors. *Proc Natl Acad Sci U S A* 110(35):14213-14218.
133. Czech MP (2000) PIP2 and PIP3: complex roles at the cell surface. *Cell* 100(6):603-606.
134. Klarlund JK, *et al.* (1998) Regulation of GRP1-catalyzed ADP ribosylation factor guanine nucleotide exchange by phosphatidylinositol 3,4,5-trisphosphate. *J Biol Chem* 273(4):1859-1862.
135. Hemmings BA & Restuccia DF (2012) PI3K-PKB/Akt pathway. *Cold Spring Harb Perspect Biol* 4(9):a011189.
136. Vivanco I & Sawyers CL (2002) The phosphatidylinositol 3-Kinase AKT pathway in human cancer. *Nat Rev Cancer* 2(7):489-501.
137. Manning BD & Toker A (2017) AKT/PKB Signaling: Navigating the Network. *Cell* 169(3):381-405.
138. Li J, *et al.* (2012) Grp1 plays a key role in linking insulin signaling to glut4 recycling. *Dev Cell* 22(6):1286-1298.
139. Hafner M, *et al.* (2006) Inhibition of cytohesins by SecinH3 leads to hepatic insulin resistance. *Nature* 444(7121):941-944.
140. Fuss B, Becker T, Zinke I, & Hoch M (2006) The cytohesin Steppke is essential for insulin signalling in Drosophila. *Nature* 444(7121):945-948.

141. Venkateswarlu K, Gunn-Moore F, Tavare JM, & Cullen PJ (1999) EGF-and NGF-stimulated translocation of cytohesin-1 to the plasma membrane of PC12 cells requires PI 3-kinase activation and a functional cytohesin-1 PH domain. *J Cell Sci* 112 (Pt 12):1957-1965.
142. Pan T, *et al.* (2013) Function and mode of action of cytohesins in the epidermal growth factor pathway in colorectal cancer cells. *Oncol Lett* 5(2):521-526.
143. Reviriego-Mendoza MM & Santy LC (2015) The cytohesin guanosine exchange factors (GEFs) are required to promote HGF-mediated renal recovery after acute kidney injury (AKI) in mice. *Physiol Rep* 3(6).
144. Grillo-Hill BK & Wolff T (2009) Dynamic cell shapes and contacts in the developing *Drosophila* retina are regulated by the Ig cell adhesion protein hibris. *Dev Dyn* 238(9):2223-2234.
145. Pichaud F (2014) Transcriptional regulation of tissue organization and cell morphogenesis: the fly retina as a case study. *Dev Biol* 385(2):168-178.
146. Zuber ME, Gestri G, Viczian AS, Barsacchi G, & Harris WA (2003) Specification of the vertebrate eye by a network of eye field transcription factors. *Development* 130(21):5155-5167.
147. Suzuki A & Ohno S (2006) The PAR-aPKC system: lessons in polarity. *J Cell Sci* 119(Pt 6):979-987.
148. Suzuki A, *et al.* (2001) Atypical protein kinase C is involved in the evolutionarily conserved par protein complex and plays a critical role in establishing epithelia-specific junctional structures. *J Cell Biol* 152(6):1183-1196.
149. Sasaki K, Kakuwa T, Akimoto K, Koga H, & Ohno S (2015) Regulation of epithelial cell polarity by PAR-3 depends on Girdin transcription and Girdin-Galphai3 signaling. *J Cell Sci* 128(13):2244-2258.
150. Chen X & Macara IG (2006) Par-3 mediates the inhibition of LIM kinase 2 to regulate cofilin phosphorylation and tight junction assembly. *J Cell Biol* 172(5):671-678.
151. Chen X & Macara IG (2005) Par-3 controls tight junction assembly through the Rac exchange factor Tiam1. *Nat Cell Biol* 7(3):262-269.

152. Bryant DM, *et al.* (2010) A molecular network for de novo generation of the apical surface and lumen. *Nat Cell Biol* 12(11):1035-1045.
153. Horikoshi Y, *et al.* (2009) Interaction between PAR-3 and the aPKC-PAR-6 complex is indispensable for apical domain development of epithelial cells. *J Cell Sci* 122(Pt 10):1595-1606.
154. Morais-de-Sa E, Mirouse V, & St Johnston D (2010) aPKC phosphorylation of Bazooka defines the apical/lateral border in Drosophila epithelial cells. *Cell* 141(3):509-523.
155. Rodriguez-Boulan E & Macara IG (2014) Organization and execution of the epithelial polarity programme. *Nat Rev Mol Cell Biol* 15(4):225-242.
156. Yamanaka T, *et al.* (2001) PAR-6 regulates aPKC activity in a novel way and mediates cell-cell contact-induced formation of the epithelial junctional complex. *Genes Cells* 6(8):721-731.
157. Chen J & Zhang M (2013) The Par3/Par6/aPKC complex and epithelial cell polarity. *Exp Cell Res* 319(10):1357-1364.
158. D'Souza-Schorey C, Boshans RL, McDonough M, Stahl PD, & Van Aelst L (1997) A role for POR1, a Rac1-interacting protein, in ARF6-mediated cytoskeletal rearrangements. *EMBO J* 16(17):5445-5454.
159. Boshans RL, Szanto S, van Aelst L, & D'Souza-Schorey C (2000) ADP-ribosylation factor 6 regulates actin cytoskeleton remodeling in coordination with Rac1 and RhoA. *Mol Cell Biol* 20(10):3685-3694.
160. Palacios F & D'Souza-Schorey C (2003) Modulation of Rac1 and ARF6 activation during epithelial cell scattering. *J Biol Chem* 278(19):17395-17400.
161. Palacios F, Schweitzer JK, Boshans RL, & D'Souza-Schorey C (2002) ARF6-GTP recruits Nm23-H1 to facilitate dynamin-mediated endocytosis during adherens junctions disassembly. *Nat Cell Biol* 4(12):929-936.
162. Palacios F, Price L, Schweitzer J, Collard JG, & D'Souza-Schorey C (2001) An essential role for ARF6-regulated membrane traffic in adherens junction turnover and epithelial cell migration. *EMBO J* 20(17):4973-4986.

163. Dunphy JL, *et al.* (2006) The Arf6 GEF GEP100/BRAG2 regulates cell adhesion by controlling endocytosis of beta1 integrins. *Curr Biol* 16(3):315-320.
164. Aikawa Y & Martin TF (2003) ARF6 regulates a plasma membrane pool of phosphatidylinositol(4,5)bisphosphate required for regulated exocytosis. *J Cell Biol* 162(4):647-659.
165. Shewan A, Eastburn DJ, & Mostov K (2011) Phosphoinositides in cell architecture. *Cold Spring Harb Perspect Biol* 3(8):a004796.
166. Ebner M, Lucic I, Leonard TA, & Yudushkin I (2017) PI(3,4,5)P3 Engagement Restricts Akt Activity to Cellular Membranes. *Mol Cell* 65(3):416-431 e416.
167. Bakin AV, Tomlinson AK, Bhowmick NA, Moses HL, & Arteaga CL (2000) Phosphatidylinositol 3-kinase function is required for transforming growth factor beta-mediated epithelial to mesenchymal transition and cell migration. *J Biol Chem* 275(47):36803-36810.
168. Shook D & Keller R (2003) Mechanisms, mechanics and function of epithelial-mesenchymal transitions in early development. *Mech Dev* 120(11):1351-1383.
169. Larue L & Bellacosa A (2005) Epithelial-mesenchymal transition in development and cancer: role of phosphatidylinositol 3' kinase/AKT pathways. *Oncogene* 24(50):7443-7454.
170. Grille SJ, *et al.* (2003) The protein kinase Akt induces epithelial mesenchymal transition and promotes enhanced motility and invasiveness of squamous cell carcinoma lines. *Cancer Res* 63(9):2172-2178.
171. Xue G & Hemmings BA (2013) PKB/Akt-dependent regulation of cell motility. *J Natl Cancer Inst* 105(6):393-404.
172. Germer A, Jahnke C, Mack A, Enzmann V, & Reichenbach A (1997) Modification of glutamine synthetase expression by mammalian Muller (glial) cells in retinal organ cultures. *Neuroreport* 8(14):3067-3072.
173. Cantley LC (2002) The phosphoinositide 3-kinase pathway. *Science* 296(5573):1655-1657.

174. Greenstein VC, *et al.* (1996) The enhanced S cone syndrome: an analysis of receptor and post-receptor changes. *Vision Res* 36(22):3711-3722.
175. Hood DC, Cideciyan AV, Roman AJ, & Jacobson SG (1995) Enhanced S cone syndrome: evidence for an abnormally large number of S cones. *Vision Res* 35(10):1473-1481.
176. Jacobson SG, *et al.* (2004) Nuclear receptor NR2E3 gene mutations distort human retinal laminar architecture and cause an unusual degeneration. *Hum Mol Genet* 13(17):1893-1902.
177. Kinori M, *et al.* (2011) Enhanced S-cone function with preserved rod function: a new clinical phenotype. *Mol Vis* 17:2241-2247.
178. Akhmedov NB, *et al.* (2000) A deletion in a photoreceptor-specific nuclear receptor mRNA causes retinal degeneration in the rd7 mouse. *Proc Natl Acad Sci U S A* 97(10):5551-5556.
179. Li J, Wang S, & Zeng ZB (2006) Multiple-interval mapping for ordinal traits. *Genetics* 173(3):1649-1663.
180. Collard BCY, Jahufer MZZ, Brouwer JB, & Pang ECK (2005) An introduction to markers, quantitative trait loci (QTL) mapping and marker-assisted selection for crop improvement: The basic concepts. *Euphytica* 142(1):169-196.
181. Hunter KW & Crawford NP (2008) The future of mouse QTL mapping to diagnose disease in mice in the age of whole-genome association studies. *Annu Rev Genet* 42:131-141.
182. Manichaikul A, Moon JY, Sen S, Yandell BS, & Broman KW (2009) A model selection approach for the identification of quantitative trait loci in experimental crosses, allowing epistasis. *Genetics* 181(3):1077-1086.
183. Van Ooijen JW (1999) LOD significance thresholds for QTL analysis in experimental populations of diploid species. *Heredity (Edinb)* 83 (Pt 5):613-624.
184. Xu S & Atchley WR (1996) Mapping quantitative trait loci for complex binary diseases using line crosses. *Genetics* 143(3):1417-1424.

185. Abiola O, *et al.* (2003) The nature and identification of quantitative trait loci: a community's view. *Nat Rev Genet* 4(11):911-916.
186. Mackay TF (2001) The genetic architecture of quantitative traits. *Annu Rev Genet* 35:303-339.
187. Mackay TF (2009) Q&A: Genetic analysis of quantitative traits. *J Biol* 8(3):23.
188. Bedell VM, *et al.* (2012) In vivo genome editing using a high-efficiency TALEN system. *Nature* 491(7422):114-118.
189. Ran FA, *et al.* (2013) Double nicking by RNA-guided CRISPR Cas9 for enhanced genome editing specificity. *Cell* 154(6):1380-1389.
190. Health GADoCDo (2010 Feb. 17) Appendix B, Classic Mendelian Genetics (Patterns of Inheritance) *Understanding Genetics: A District of Columbia Guide for Patients and Health Professionals.*, Washington (DC)).
191. Griffiths AJF, Miller, J.H., Suzuki, D.T., et al (2000) Penetrance and expressivity. *An introduction to Genetic Analysis. 7th edition*, ed Freeman WH).
192. Pachydaki SI, *et al.* (2009) Phenotypic features of patients with NR2E3 mutations. *Arch Ophthalmol* 127(1):71-75.
193. Audo I, *et al.* (2008) Phenotypic variation in enhanced S-cone syndrome. *Invest Ophthalmol Vis Sci* 49(5):2082-2093.
194. Manayath GJ, *et al.* (2014) A novel mutation in the NR2E3 gene associated with Goldmann-Favre syndrome and vasoproliferative tumor of the retina. *Mol Vis* 20:724-731.
195. Kanda A & Swaroop A (2009) A comprehensive analysis of sequence variants and putative disease-causing mutations in photoreceptor-specific nuclear receptor NR2E3. *Mol Vis* 15:2174-2184.
196. Jordan DM, *et al.* (2015) Identification of cis-suppression of human disease mutations by comparative genomics. *Nature* 524(7564):225-229.

197. Demetrius L (2005) Of mice and men. When it comes to studying ageing and the means to slow it down, mice are not just small humans. *EMBO Rep* 6 Spec No:S39-44.
198. Rajala A, Tanito M, Le YZ, Kahn CR, & Rajala RV (2008) Loss of neuroprotective survival signal in mice lacking insulin receptor gene in rod photoreceptor cells. *J Biol Chem* 283(28):19781-19792.
199. Rajala A, Dighe R, Agbaga MP, Anderson RE, & Rajala RV (2013) Insulin receptor signaling in cones. *J Biol Chem* 288(27):19503-19515.
200. Lodish H, Berk, A., Zipursky, S.L., et al.. (2000) *Molecular Cell Biology*. 4th edition. (W. H. Freeman, New York).
201. Felgner PL, et al. (1987) Lipofection: a highly efficient, lipid-mediated DNA-transfection procedure. *Proc Natl Acad Sci U S A* 84(21):7413-7417.
202. Lin YC, et al. (2014) Genome dynamics of the human embryonic kidney 293 lineage in response to cell biology manipulations. *Nat Commun* 5:4767.
203. Behrens J, Mareel MM, Van Roy FM, & Birchmeier W (1989) Dissecting tumor cell invasion: epithelial cells acquire invasive properties after the loss of uvomorulin-mediated cell-cell adhesion. *J Cell Biol* 108(6):2435-2447.
204. Gaschet J & Hsu VW (1999) Distribution of ARF6 between membrane and cytosol is regulated by its GTPase cycle. *J Biol Chem* 274(28):20040-20045.
205. Langille SE, et al. (1999) ADP-ribosylation factor 6 as a target of guanine nucleotide exchange factor GRP1. *J Biol Chem* 274(38):27099-27104.
206. Cohen LA, et al. (2007) Active Arf6 recruits ARNO/cytohesin GEFs to the PM by binding their PH domains. *Mol Biol Cell* 18(6):2244-2253.
207. DiNitto JP, et al. (2007) Structural basis and mechanism of autoregulation in 3-phosphoinositide-dependent Grp1 family Arf GTPase exchange factors. *Mol Cell* 28(4):569-583.
208. Santy LC (2002) Characterization of a fast cycling ADP-ribosylation factor 6 mutant. *J Biol Chem* 277(43):40185-40188.

209. Venkataraman A, Nevriy DJ, Filtz TM, & Leid M (2012) Grp1-associated scaffold protein (GRASP) is a regulator of the ADP ribosylation factor 6 (Arf6)-dependent membrane trafficking pathway. *Cell Biol Int* 36(12):1115-1128.
210. Brown FD, Rozelle AL, Yin HL, Balla T, & Donaldson JG (2001) Phosphatidylinositol 4,5-bisphosphate and Arf6-regulated membrane traffic. *J Cell Biol* 154(5):1007-1017.
211. Wu H, *et al.* (2007) PDZ domains of Par-3 as potential phosphoinositide signaling integrators. *Mol Cell* 28(5):886-898.
212. Cappola TP, *et al.* (2010) Common variants in HSPB7 and FRMD4B associated with advanced heart failure. *Circ Cardiovasc Genet* 3(2):147-154.
213. Matkovich SJ, Van Booven DJ, Cappola TP, & Dorn GW, 2nd (2010) Association of an intronic, but not any exonic, FRMD4B sequence variant and heart failure. *Clin Transl Sci* 3(4):134-139.
214. Garner C, *et al.* (2014) Genome-wide association study of celiac disease in North America confirms FRMD4B as new celiac locus. *PLoS One* 9(7):e101428.
215. Santiago JA, Bottero V, & Potashkin JA (2017) Dissecting the Molecular Mechanisms of Neurodegenerative Diseases through Network Biology. *Front Aging Neurosci* 9:166.
216. Kong Y, Naggert JK, & Nishina PM (2018) The Impact of Adherens and Tight Junctions on Physiological Function and Pathological Changes in the Retina. *Adv Exp Med Biol* 1074:545-551.

BIOGRAPHY OF THE AUTHOR

Yang Kong was born in Jinan, China on February 24, 1984. He was graduated from Shandong Experimental High School in 2003. He was matriculated in Weifang Medical University and graduated in 2008 with the Bachelor's degree in Clinical Medicine (M.D. equivalent). He enrolled in Shandong University, School of Medicine in the autumn of 2008, and obtained Master's degree in Surgery. After graduation, Yang entered the program of Graduate School of Biomedical Science and Engineering at the University of Maine and joined Dr. Patsy Nishina's group at the Jackson Laboratory since 2013 for studying inherited retinal disorders and their genetic basis by using mouse models. Yang is a candidate for the Doctor of Philosophy degree in Biomedical Science from the University of Maine in August 2018.